Engineering Colloidal Microstructures for Functional Properties: Crystals and Gels

by

Peng-Kai Kao

A dissertation submitted in partial fulfillment
of the requirements for the degree of
Doctor of Philosophy
(Chemical Engineering)
in the University of Michigan
2021

Doctoral Committee:

Professor Michael J. Solomon, Chair
Professor Sharon C. Glotzer
Professor Ronald G. Larson
Associate Professor Xiaoming Mao

Peng-Kai Kao

pkkao@umich.edu

ORCID iD: 0000-0002-3123-2926

Dedication

To my mother 陳金蘭 (Chin-Lan Chen) and my father 高添慶 (Tien-Ching Kao) who always love and support me.

Acknowledgements

I would like to thank my advisor, Professor Mike Solomon. Mike cares about all his students and respect us as independent researchers. Mike is a pioneering leader in the field of soft matter. Mike is an educator that always emphasizes the importance of diversity, equity, and inclusion. More importantly, Mike is our mentor that provides an environment with encouragement and support. I am very happy and thankful that I can have Mike as my Ph.D. advisor. I also want to thank my committee, Professor Sharon Glotzer, Professor Ronald Larson, and Professor Xiaoming Mao.

The meaning of goodbye for me is to remember the good things happened in a relationship and bring the positive influence with me to the next journey. I want to thank Lukasz Maksymiuk. Without you, I don't think I would be able to complete my Ph.D. study. Thank you for your support, care and accompany through the high and low points of my time in graduate school. I would like to thank Mahesh Ganesan for being my mentor, not only teaching me the knowledge about colloidal gels and rheology, but also providing me so much guidance in my graduate student life. In my colloidal crystal projects, I am very grateful to collaborate with Bryan VanSaders, who significantly increase the depth of the study and allow the nice comparison between experiments and computer simulation.

I want to thank Keara Saud and Colin Greatwood. Thank you for always having me at your most amazing house, spending time together, listening to music and chatting about everything happened in graduate school. I feel so lucky to have the unique friendship with Sabina Wilkanowicz. Thank you for sending me your most positive and energetic messages from

Poland. I am also very grateful to have Yulei Zhang and Yixuan Chen as my best friends in Ann Arbor. Thank you for all the countless talks together with tears and laughter. I am also thankful to have my awesome friends from the Michigan family, Joanne Beckwith, Xiaowen Zhao, Wayne Gray, Paul Yu, George Tsai, and Yufei Wei. I am so lucky to meet Joseph Mroz at the end of my PhD journey. Thank you for being supportive and showing great care to me.

Lastly, I want to thank my family in Taiwan, my father, my mother, my sister and my nephews, Ryan, and Ragnar. Every winter, I am so excited to go back home and visit you. I miss all the wonderful trips together. This pandemic makes it harder for all of us, but we shall see each other pretty soon!

Table of Contents

List of Tables

List of Figures

Abstract

In this dissertation, we report the microstructural engineering of colloidal crystals and gels to alter their macroscopic functional properties, including, specifically, the optical properties of crystals and the rheological properties of gels. Confocal laser scanning microscopy (CLSM) is used to characterize microstructures at the single particle level. Small-angle light scattering (SALS) and rheology are used separately to quantify the macroscopic light diffraction responses and mechanical properties.

External fields can accelerate colloidal self-assembly, yet the accelerated kinetics can negatively impact the quality of ordered crystal structures. We show that cyclically applied external electric fields can improve the crystallinity of colloidal crystals by annealing local disorder. We find that the optimal off-duration for maximum annealing is approximately one-half of the melting half lifetime of the assembled crystal. The annealing efficacy depends on the creation of mobile defects while avoiding additional immobile defects during field off-duration. Molecular dynamics simulations show that the optimal off-duration for maximum annealing, normalized by crystal melting time, is insensitive to particle interaction details. This research provides a simple and efficient strategy to rapidly create perfect crystals as well as the mechanistic insights into how defects annealing is the key to the phenomena.

From CLSM, we find that ellipsoids with aspect ratio 2.0 melt into disordered structures 5.7 times faster compared to spheres. On the other hand, ellipsoids with the same aspect ratio self-assemble into ordered crystals at a similar rate to spheres. By molecular dynamics simulations, we find that it is the Brownian rotation of the ellipsoids contributes to faster melting

kinetics relative to spheres. Insights from the project can be applied to reconfigurable self-assembly manipulation.

Physical gelation of colloids produces elastic structures that are used to stabilize formulation. However, rheological control is greatly limited by the universality of the arrested spinodal decomposition mechanism of colloidal gelation. Volume fraction and interparticle bonding are the limited tools to control gel modulus. We demonstrate, through manipulation of particle shape, that we can expand the design space of available elastic states. Gels formulated from discoids exhibit expanded elasticity states that are shifted in volume fraction from the universality of sphere gels by a factor of as much as 15 in volume fraction and 20 in elastic modulus. We apply the predictive model of particle gelation and explain this efficient generation of elasticity into a series of factors dependent on fractal dimension, backbone topology, and non-central forces, with each independently measured and quantified. Our study reveals a new strategy for designing sustainable gels materials with tailored rheological and mechanical properties, particularly elasticity at ultra-low volume fractions.

Chapter 1 Introduction

1.1 Crystallization of Colloids

Colloidal systems studied in this dissertation are nanometer to micrometer scale solid particles that are suspended in a fluid phase. Due to their larger sizes, the position and motion of these particles can be captured and quantified by confocal microscopy and light scattering. Colloidal particles therefore have been viewed as analogues of atoms with tailorable size, shape and interactions[1]. Colloidal particles can vary in size from about 5 nm to about 5 μm. In this range, Brownian motion and interparticle forces are both important to their collective structure, dynamics, and function. These particles are observable by optical microscopy at the upper end of that scale, and it is this range that will be of particular interest to the present work.

Colloidal particles can assemble into ordered or disordered structures as a consequence of different driving forces. Particles in suspensions are driven by thermal fluctuation, also known as the Brownian motion[2]. In addition, the assembled structure can be altered through dynamic manipulation of thermodynamic variables and colloidal properties of the system, such as particle size, shape, and interaction potential. The motion of colloidal particles can also be induced by external fields, such as electric field, optical field, magnetic field, and temperature gradient[1]. Manipulating the magnitude or direction of these externally applied fields allow phoretically-control configurations of colloids assembly[3].

Pusey and Megen first reported spherical colloids undergo a fluid to crystal phase transition as their volume fraction increases[4]. There exists short-range repulsion between the

poly-12-hydroxysteric acid (PHSA) stabilized polymethylmethacrylate (PMMA) particles and long-range spatial order once they crystalize. Since then, many research studies have been conducted to explore using external fields to assist the crystallization of colloids. For example, Kim et al.[5] showed a photo-induced and reconfigurable crystallization process for colloidal spheres. Macfarlane et al.[6] showed DNA-functionalized colloidal nanoparticles can be assembled into crystalline materials. Swan et al.[7] demonstrated that paramagnetic colloids can be self-assembled into body-centered tetragonal crystals. Lumsdon et al.[8] reported using coplanar alternating current (AC) fields to form two-dimensional colloidal crystals by microspheres. In this dissertation, we present experiments and simulations to study the annealing as well as kinetics of crystallization and melting of colloidal crystal monolayers by the application of coplanar AC electric fields.

1.1.1 Coplanar Electric Field-assisted Assembly

The application of a coplanar AC electric field with frequency ω across a colloidal suspension leads to particles polarization. The dielectrophoretic (DEP) force and the dipole-dipole (chaining) interaction are two of the mechanisms that induce the crystallization of colloidal spheres. Colloidal particles interact with nonuniform electric fields and migrate to their net potential energy minimum. This electrokinetic migration is balanced by hydrodynamic drag and is referred to as DEP[9]. In our system reported in Chapter 2 and Chapter 3, particles first settled onto the substrate of the coplanar device and formed a disordered monolayer before any assembly was initiated. The DEP force due to vertical field gradient within the coplanar system is thus not at play. We acknowledge some DEP contributions driving densification in the plane parallel to the bottom substrate, as demonstrated by the fact that particle densities are highest at the midplane of the device.

To study the particle–particle dipolar interaction for concentrated two-dimensional spherical colloids, we can use a generalized expression as shown below[9]:

$$u(r_{ij}, \theta_{ij}, x_i, z_i) = -kT\lambda_E f_\phi P_2(cos\theta_{ij}) \left(\frac{2a}{r_{ij}}\right)^3 E^*(x_i, z_i)^2 \quad \textit{1-1}$$

where $u(r_{ij}, \theta_{ij})$ is the dipole-dipole interaction between particles, r_{ij} is the distance between particle i and j, θ_{ij} is the angle between particle i and j, λ_E is the relative dipolar and Brownian energy, f_ϕ is the area-fraction-dependent modification term, $P_2(cos\theta_{ij})$ is the second Legendre polynomial, a is particle radius, $E^*(x_i, z_i) = \frac{E(x,z)}{E_0}$ is the local normalized electric field, E_0 is the electric field strength. Specifically, λ_E can be expressed as:

$$\lambda_E = \pi\varepsilon_s a^3 (f_{cm} E_0)^2 / kT \quad \textit{1-2}$$

where ε_s is the solvent permittivity and f_{cm} is the Clausius—Mosotti factor given as:

$$f_{cm} = Re[(\widetilde{\varepsilon_p} - \widetilde{\varepsilon_s})/(\widetilde{\varepsilon_p} + 2\widetilde{\varepsilon_s})] \quad \textit{1-3}$$

where $\widetilde{\varepsilon_p}$ and $\widetilde{\varepsilon_s}$ are the complex particle and solvent permittivity.

From the above relationship, we know the dipolar energy scale with a^3E^2. The electric field strength, E, required for crystallization increase with frequency and decrease with particle size. Mittal et al.[10] also summarized the order-disorder transition of polystyrene particles in AC electric field generated in a coplanar electrode geometry scales with a^3E^2 given by the ratio between dipolar energy and thermal energy. In Chapter 3, we report the impact of electric field applied voltage and frequency on quality of the assembled colloidal crystals.

The operating parameters of the applied external fields have great impact on the quality of the colloids assembled structures. It is very common that external-field-assisted colloidal crystal assemblies are polycrystalline in nature with defects embedded, such as vacancies and interstitials, as well as grain boundaries that separate adjoining crystals of different orientations[11]. The presence of these defects microstructures drastically alters material properties.

For example, Liu et al.[12] showed the connection between colloidal crystal assembly quality and the intensity of reflective structural color peak intensity: the reduction in peak intensity scales with increased defect density.

1.1.2 Colloidal Crystals and Structural Color

Structural color is produced by constructive interference of visible light bands based on Bragg's scattering within periodically ordered nanostructures[13]. Its brilliant iridescence can be found in the nature, such as Morpho butterfly wings, feather of blue-tailed bee-eater[14] and opals[15]. For ordered structures composed of micrometer-scale building blocks, the structural reflection is in the infrared range of wavelengths. For example, the active color change of chameleon has been related to a combination of pigments and structural color. Specifically for structural color reflection, there is one upper layer of iridophores consists of guanine nanocrystal that can reflect different wavelengths of light by actively adjusting the spacing between the nanocrystals. There exists another deeper ordered cells that reflect the near-infrared range light which provides passive thermal protection[16].

Colloidal crystals can produce optical responses that depend on the wavelength, angle, and polarization of incident light and thus have been developed to mimic structural color in nature[17]. By slowly evaporating solvent, colloidal particles can self-assemble into crystals and generate iridescent color[12]. Shah et al.[18] reported using direct current (DC) electric field to assemble close-packed colloidal crystals. By changing the size of the particles, red, green, and blue structural color is observed for building blocks with diameters of 0.50, 0.40, and 0.29 μm, respectively. Magnetic nanoparticles based on magnetite (Fe_3O_4) can respond to a magnetic field and form photonic crystal arrays conveniently with tunable optical properties[17]. Hu et al.[19] demonstrated magnetically induced self-assembly of superparamagnetic colloids for colorimetric

humidity sensor. These artificial structural color devices based on colloidal crystals have been developed for applications in advanced display, smart windows, and camouflage devices[17].

1.1.3 Shape Effects on Colloidal Crystals

Colloidal particles with anisotropy in shapes and compositions have been engineered for particular targeted assembly structures[20]. One of the key anisotropy dimensions of shape is particle's aspect ratio, which is defined by the ratio between the major axis and the minor axis. In this dissertation, we explore two types of spheroidal colloids: ellipsoids, which are prolate (elongated) spheroids with aspect ratio larger than one, and discoids, which are oblate (flattened) spheroids with aspect ratio smaller than one. Specifically, in the study of colloidal crystals (Chapter 3), we focus on how ellipsoidal shape can affect the kinetics of crystallization and melting.

Ellipsoidal colloids used in this study are prepared by thermo-mechanical stretching[21]. It is demonstrated by molecular dynamics simulation that the maximum packing fraction of ellipsoids is greater than that of spheres[22]. Shah et al.[23] show experimentally that ellipsoids can form orientational and layered positional ordered packing structures under direct current (DC) electric fields due to electrophoretic deposition and field-assisted assembly. Ganesan et al.[24] use DC electric fields in conjunction with ultraviolet light to self-assemble highly dense structures of colloidal ellipsoids with three-dimensional order and volume fraction as large as 67%. Ding et al.[25] report a convective self-assembly of ellipsoidal γ-Fe_2O_3–SiO_2 core–shell particles in an external magnetic field and the assembly showed strong structural color based on the size of the ellipsoids. Kohri et al.[26] demonstrate structural coloration made of evaporation-driven ellipsoidal melanin particles assembly. These examples show ellipsoidal shape of the building blocks provides potential applications for functional materials.

1.2 Colloidal Gels

1.2.1 Rheology of colloidal gels

In Chapter 4 of this dissertation, we will study the effect of particle shape on the microstructures and macroscopic mechanical properties of the assembled colloidal gels. Colloidal gels studied here are diffusion-limited cluster aggregation (DLCA) where the arrested spinodal mechanism arisen from strong and short-range pair potentials between colloids. The attraction potential between these particles are so strong that the bonds are irreversible and the gels are non-equilibrium[27]. The assembled DLCA gels have branched, tenuous, and space-spanning fractal structures with a low fractal dimension ≈ 1.8[2].

Colloidal gels have two characteristic rheological properties. First, at low frequency, the elastic modulus (storage modulus), G', is greater than the viscous modulus (loss modulus), $G"$, reflecting the solid-like elasticity which can be used to provide a stabilizing network for formulation purposes. The elastic modulus is linear thus nearly independent of frequency and is strongly dependent on particle volume fraction as well as interaction potential[2]. Second, the assembled structures will undergo fluidization transition at the yield stress, σ_{yield}, which is defined as G' and $G"$ cross. Typically, there are three stages for a colloidal gels been sheared[28]: Stage I is the solid regime, where $G' > G"$. Stage II is the solid-liquid transition where G' decreases sharply and $G"$ reaches its maximum. Stage III is the liquid region where $G' < G"$. Based on the above featured material properties, colloidal gels are commonly been applied in industries, such as pharmaceutical formulations[29], cosmetics, food science[30], ceramics[28], and agricultural products.

1.2.2 Shape effect on colloidal gels

It is well known that strong interparticle attraction can foster particle aggregation. Colloidal gel microstructures are strongly dependent on the strength of the short-range attraction between particles. Spherical colloids diffuse isotropically in the solution until they collide with another particle or growing cluster, they then form physical bonding at the contact position[31]. It is of great interest to study how shape of constituent colloids can influence the larger assembled structures formed by non-equilibrium DLCA. Rothenbuhler et al. use random-walker simulations to model anisotropic particles, as parameterized by particle aspect ratio, diffuse in a viscous fluid and form diffusion-limited aggregation[31]. Their results show that clusters of rods are less dense than those of disks or compact objects of equal volume. In addition, particle shape controls the distribution of the number of interparticle contacts per particle in the cluster. For long thin rods, the maximum nearest-neighbor trends toward one in the limit of very high aspect ratios.

Solomon and Spicer[32] summarized the dynamic arrest volume fraction of colloidal rod systems reported in the literature. From the comparison, gels made of rods are stronger relative to gels made of spheres. In addition, Mohraz and Solomon[33] report that for rod gels created at fixed volume fraction, they become stiffer as their aspect ratio increased. Very little fundamental understanding of what shape of building blocks or microstructures is required to achieve higher elasticity. Some possible mechanisms for anisotropic building particles to contribute to different rheological responses are non-central pair forces, anisotropy in excluded volume, as well as the change in the number of contacts per particle.

1.3 Objectives and Outline

In this thesis, we study two different colloidal assembled structures: crystals and gels. Our goal is to engineer the microstructures of these assemblies for tuning their elastic, rheological, and optical properties for specific applications.

In Chapter 2, we report using cyclic AC electric fields to anneal colloidal crystals. This cyclic field is characterized by its amplitude, on-duration (t_{on}) for crystallization, and off-duration (t_{off}) for melting. We find a fundamental relationship between the time scale for local defects rearrangements during melting and the optimal cyclic external field condition which best accelerates the crystal annealing.

In Chapter 3, we demonstrate colloids anisotropy effects on the kinetics of self-assembly. We use confocal microscopy, small-angle light scattering and molecular dynamics simulation; we in particular compare the behavior of spheres and ellipsoids. The comparison shows that particle shape has a strong effect on the melting kinetics of the ordered phases. Simulation results further establish that the enhanced melting is linked to the dynamical availability of rotational degrees of freedom for the ellipsoids.

In Chapter 4, we study colloids anisotropy effects on rheology properties of gels. We design anisotropic shape particles to synthesize "minimal gels" – colloidal gels at vanishingly small volume fractions. We demonstrate that gels formed by anisotropic building blocks exhibit enhanced solid-like behavior relative to their spherical counterparts.

Finally, this dissertation concludes with a summary of the proposed work and future directions that can be taken based on the results of this thesis.

Chapter 2 Accelerated Annealing of Colloidal Crystal Monolayers by Means of Cyclically Applied Electric Fields[1]

2.1 Abstract

External fields are commonly applied to accelerate colloidal crystallization; however, accelerated self-assembly kinetics can negatively impact the quality of crystal structures. We show that cyclically applied electric fields can produce high quality colloidal crystals by annealing local disorder. We find that the optimal off-duration for maximum annealing is approximately one-half of the characteristic melting half lifetime of the crystalline phase. Local six-fold bond orientational order grows more rapidly than global scattering peaks, indicating that local restructuring leads global annealing. Molecular dynamics simulations[2] of cyclically activated systems show that the ratio of optimal off-duration for maximum annealing and crystal melting time is insensitive to particle interaction details. This research provides a quantitative relationship describing how the cyclic application of fields produces high quality colloidal crystals by cycling at the fundamental time scale for local defect rearrangements; such understanding of dynamics and kinetics can be applied for reconfigurable colloidal assembly.

---

[1] The text in this chapter was originally in P. Kao, B. J. VanSaders, S. C. Glotzer, and M. J. Solomon, *Scientific Reports* (2021), accepted for publication. P. Kao and B. J. VanSaders contributed equally to this work.

[2] Molecular dynamic simulations results reported in this chapter were acquired as part of collaboration with Dr. Bryan J. VanSaders.

2.2 Introduction

Because of their nano to micro dimensions, colloids crystallize more slowly than molecular, surfactant, or polymeric systems[34]. Electrokinetic[8,24,35–38], magnetic[7], and photo-induced[5] methods have been used to drive colloidal self-assembly at accelerated rates. Yet these methods often confront a tradeoff between the rate of crystallization and the quality of the self-assembled crystal[39]. That is, colloidal crystals formed at faster rates are prone to include undesirable defect microstructures such as vacancies, dislocations, and grain boundaries, each of which has negative effects on the overall crystal quality[12]. Understanding how fields can be used to drive colloidal crystallization that is both fast and high quality can be applied to produce ordered arrays with collective properties of value to applications such as reversible structural color[18], photonic polarization[40], and shape-memory retention[41].

In general, annealing refers to a variety of tactics used to improve the microstructure of a condensed phase by controlling the kinetics of diffusion. The most commonly encountered form of annealing is to heat a crystalline solid to a point where internal diffusion rates (and hence grain growth) are significantly accelerated, but below the point of thermodynamic melting. This procedure generally drives the microstructure of the material towards equilibrium, which is often desirable. Annealing has been widely used in metallurgy, macromolecular science, and biotechnology[42]. Steel, for example, is commonly thermally annealed to alter its physical and mechanical properties for commercial applications. In macromolecular crystallization, cryogenic flash-cooling can quickly form crystals for structure determination of biological macromolecules, yet it also dramatically increases the lattice misorientation (mosaicity) of the crystals[43]. The quality of flash-cooled crystals can often be improved by warming and then

cooling for a short amount of time. This annealing procedure can drive local lattice reordering and reduce the distribution of lattice spacing and orientation.

In equilibrium systems, only thermal energy is available to drive transitions to resolve metastable defect states in favor of the free energy minimizing structure. Increasing the system temperature increases the rate of such transitions, as thermal energy is equipartitioned across all degrees of freedom. In out-of-equilibrium systems, however, energy can be introduced heterogeneously to specific degrees of freedom that may strongly drive the system towards new configurations[11,44,45]. Particles that are given just enough mobility to reconfigure their local neighborhoods (but not so much as to form a jammed state[46] or to induce bulk melting) can accelerate the annealing of the colloidal crystals and create highly ordered crystals. Bevan and coworkers designed a closed-loop control scheme to evolve colloidal crystals from polycrystalline states to a single domain crystal under electric field mediated crystallization[47–49]. Active matter has also been applied to overcome naturally occurring kinetic barriers. For example, van der Meer showed via simulation, and Ramananarivo et al. by experiment, that the annealing of passive colloids can be accelerated by introducing self-propelled microparticles[11,50]. Singh et al. showed that the crystallization of passive silica colloids can be directed by a small number of active colloids[51]. Altemose et al. used light-powered oscillations of active matter to induce annealing of colloidal crystals[52].

While accelerated annealing may be accomplished by injecting energy into the colloidal system via active particles or external fields, another alternative to introduce out-of-equilibrium fluctuations to the system is to cycle the potential interactions between colloids. This scheme is conceptually similar to temperature cycling for heat treatment annealing of metals[53]. In this context, strong field-induced colloidal interactions are equivalent to a low temperature state, and

weak field-induced interactions to a high temperature state. Experimentally, Swan et al. showed that a pulsed uniform magnetic field can be used to escape kinetically arrested states and assemble paramagnetic colloids into crystalline domains[7]. Sherman and Swan showed via simulation of a colloidal crystal that a cyclically toggled external field leads to a faster growth rate and fewer defects formed when compared to self-assembly in a steady field[39,54].

In this work, we present simulations and experiments to study the annealing of colloidal crystal monolayers by cyclic application of an AC electric field. We define the cyclically applied waveform by means of three parameters: amplitude, on-duration (t_{on}), and off-duration (t_{off}). Within this cyclic scheme, colloidal particles form close-packed structures during the t_{on} period of the cycle; they are free to thermally diffuse during the t_{off} portion of the cycle. We define the duty cycle as the ratio between t_{on} and t_{off}, and vary this ratio as part of the study. We observe different annealing performance and rates for different duty cycles. Time-resolved confocal laser scanning microscopy (CLSM) and small-angle light scattering (SALS) measurements of the cyclic annealing demonstrate that local ordering precedes global ordering in the annealing process. In addition, we find that the best annealing performance, as measured by CLSM, occurs at a duty cycle time that is approximately one half of τ_{50} ($t_{off} = 0.5\tau_{50}$). Here τ_{50} is the half-life time of a crystal melting under the same field assembly conditions[55]. Using a molecular dynamics (MD) model of cyclically applied field-assisted crystallization, we observe a similar relationship between the best annealing performance duty cycle time and the characteristic system melting time. Furthermore, this duty cycle is robust to changes in the particle interactions. By tracking energy exchanged with the thermal reservoir during simulation, we observe a maximum in heat transfer (dissipated work) at slightly shorter duty cycle times than that of peak annealing. This difference is hypothesized to be due to diffusive motion on length

scales less than a single lattice spacing. By contrast, defect annealing requires cooperative rearrangement over longer distances and times.

Our results suggest the existence of a fundamental relationship between the kinetics of melting and the characteristics of the cyclic field that optimize annealing. That is, colloidal crystal monolayers self-assemble rapidly and with high quality under cyclical loading at a duty cycle that coincides with the fundamental timescale for local defect rearrangements. At this timescale work dissipation rates are nearly maximized. This timescale-matching strategy represents a novel approach to annealing that could be easily extended to other types of systems at different length and time scales without the need to characterize or navigate the free energy landscape.

2.3 Results and Discussion

2.3.1 Cyclic annealing of colloidal crystals with different duty cycles

We study cyclic annealing through the crystallization of polystyrene spheres with diameter 4.00 ± 0.04 μm suspended in 0.1 mM NaCl aqueous solution. The colloidal suspension was injected into a coplanar AC electric field device to generate monolayer colloidal assemblies. Figure 2.1a illustrates the annealing experiment. During each cycle, the electric field is maintained at a constant root-mean-square voltage (V_{rms}) of 8.0 V, creating an electric field strength (E) of 32 kVm^{-1} and frequency 5 MHz for t_{on}, and then switched off for t_{off}. This field strength and frequency were selected to ensure that the colloidal particles assemble into dense 2D crystal structures[55]. Under these conditions the field-induced polarization of the colloids leads to particle chaining along the electric field direction, and eventual 2D crystallization along the bottom surface of the device.

We explored the impact of cycling the applied AC field on crystal annealing. During field-on conditions (of duration t_{on}), polarization of the colloids induced particle attraction. Conversely, during field-off conditions (t_{off}) particle dynamics were controlled by diffusion and hard-sphere like interactions. t_{on} was set to be a constant value of 90 s for all experiments. This on-duration was selected as per previous work[55], which indicated that the half-life of crystallization, $\tau_{crystal}$, in this system is 14.8 ± 0.9 seconds. By applying the electric field for 90 seconds, we ensure that the system has completed its freezing transition during the on-phase of the cycle. During t_{off}, the electric field is turned off, and spheres relax and reconfigure under Brownian motion during this period. At the conditions of these experiments, the half-life for the melting transition (τ_{50}) is 48.0 ± 1.7 seconds. The half-life times for crystallization and melting were measured based on the growth and decay of the light scattering diffraction response under identical external fields conditions by means of small-angle light scattering[55]. The duty cycle of the electric fields, $\xi = t_{on}/(t_{on} + t_{off})$, is varied from 0.16 ($t_{off}$ = 10τ_{50}) to 1 (t_{off} = 0) in this study. All experiments are performed for a total duration of 2,700 s.

Both t_{on} and t_{off} are independent parameters in the study. We observed the degree of annealing as a function of the cyclic duty cycle by specifically changing t_{off} (with t_{on} fixed). We chose this design space so as to focus on the de-correlating effect of the t_{off} period while ensuring that t_{on} is sufficiently long for a complete phase transformation to occur in the period of the cycle. The study can therefore be thought of as probing one region of a design space specified by t_{on} and t_{off}. To analyze this process, we take CLSM images and SALS images at the end of each field-on period. Given the duration of the cycle, we analyzed a number of cycles varying from 6 to 30 over the range of conditions studied. Each condition was tested five times by CLSM, three times by SALS, and seven times by MD.

Figure 2.1b compares representative CLSM results at the end of each field-on duration, with t_{off} = 0, 0.5τ_{50}, and 10τ_{50}. We show the first, third and last cycle of CLSM images to demonstrate particle structural arrangements that occur as time progresses. In the 'always-on' condition (t_{off} = 0), a phase with high orientational order yet with kinetically arrested defects (vacancies and grain boundaries) was observed in the last cycle. When the system undergoes a continual cycle of crystallization with short periods of melting between each cycle, a close-packed monolayer crystal with minimal defects formed, such as shown in the case of t_{off} = 0.5τ_{50}. For t_{off} = 10τ_{50}, the system has sufficient time in the field-off condition to fully melt during each cycle, which allows new defects to be generated at each t_{on}. This condition yielded structures with poor crystal quality and abundant local vacancies and dislocations.

We calculate the area fraction covered by spheres as $d_{2D} = N \times S_a/A$, where N is the number of spheres in a CLSM image, S_a is the projected 2D area of a single sphere, and A is the area of a CLSM image. For t_{off} = 0, the area fractions increase from 65 ± 1.9% to 73 ± 1.5% during the annealing process. For t_{off} = 0.5τ_{50}, the 2D area coverage increased from 65 ± 2.5% to 81 ± 1.0 %. For t_{off} = 10τ_{50}, the area fraction only increases slightly throughout the process – from 66 ± 0.2% to 70 ± 1.7%. The increase of d_{2D} for all cases demonstrates that a more ordered system is created via annealing. The system is able to accommodate more particles within the same 2D area as a consequence of this ordering because the free space (area) is greater when particles occupy crystalline lattices than random configurations[2]. This statement aligns with our observation that the highest steady state d_{2D} value occurs at t_{off} = 0.5τ_{50} and the lowest d_{2D} value occurs at t_{off} = 10τ_{50}. A comparison of how d_{2D} changes as time progresses for these three duty cycles is shown in Figure 2.6.

To quantify colloidal crystal quality, we compute the six-fold bond orientational order ψ_6 (see Materials and Methods Section) for nine annealing experiments with different duty cycles. At the end of each t_{on}, we capture five CLSM images and calculate ψ_6 based on centroidal positions of the particles. The locations where these five images were taken are separated by at least 130 μm along the centerline direction to avoid duplicative characterization of the area. We compute the average value and standard deviation of ψ_6 for each cycle. The time-evolution of ψ_6 for each different duty cycle is shown in Figure 2.1c. ψ_6 data sets are plotted from arbitrary starting positions for purposes of visualization. We observe that ψ_6 increases quickly and remains steady for spheres assembled under steady AC electric field (t_{off} = 0). For t_{off} = $0.5\tau_{50}$, ψ_6 improves rapidly and continues to increase gradually for the entire process. However, if the field is off for a long t_{off} in each cycle, no apparent annealing effect is seen in ψ_6. For example, ψ_6 shows no detectable trend over a ~2700 s duration when t_{off} = $10\tau_{50}$.

We further captured the time scale of the annealing process by regressing the time-resolved ψ_6 data with the following exponential plateau model:

$$\psi_6 = \psi_{6,M} - (\psi_{6,M} - \psi_{6,o})e^{-kt} = \psi_{6,M} - \Delta\psi_6 e^{-kt} \qquad 2\text{-}1$$

where $\psi_{6,M}$ is the maximum ψ_6, $\psi_{6,o}$ is the initial ψ_6, and k is the annealing rate constant. We define $(\psi_{6,M} - \psi_{6,o})$ as $\Delta\psi_6$, which is a convenient parameter to quantify the annealing performance.

Figure 2.1d demonstrates the significant dependence of $\Delta\psi_6$ on t_{off}/τ_{50}, as extracted from Equation (2-1). $\Delta\psi_6$ is singly peaked at t_{off}/τ_{50} = 0.5. The existence of a maximum in $\Delta\psi_6$ indicates that there is an optimal condition at which particles in the film are able to circumvent kinetically arrested states. At this special timescale, re-arrangements during the field-off condition do not hinder crystallization once the field is switched on, but rather enhance it. For

t_{off}/τ_{50} values extending from 0.1 to about 2, the relaxation of the system from its initial condition to the fluid ground state (for the field off condition) was interrupted by turning the field back on. This partial melting followed by recrystallization represents a nonequilibrium kinetic pathway that is leveraged by cyclic annealing to enhance the quality of the assembled colloidal crystal, as quantified by $\Delta\psi_6$. However, for $t_{off}/\tau_{50} \geq 5$, new defects are increasingly created during each cycle's crystallization, and therefore annealing is less successful than the optimal condition.

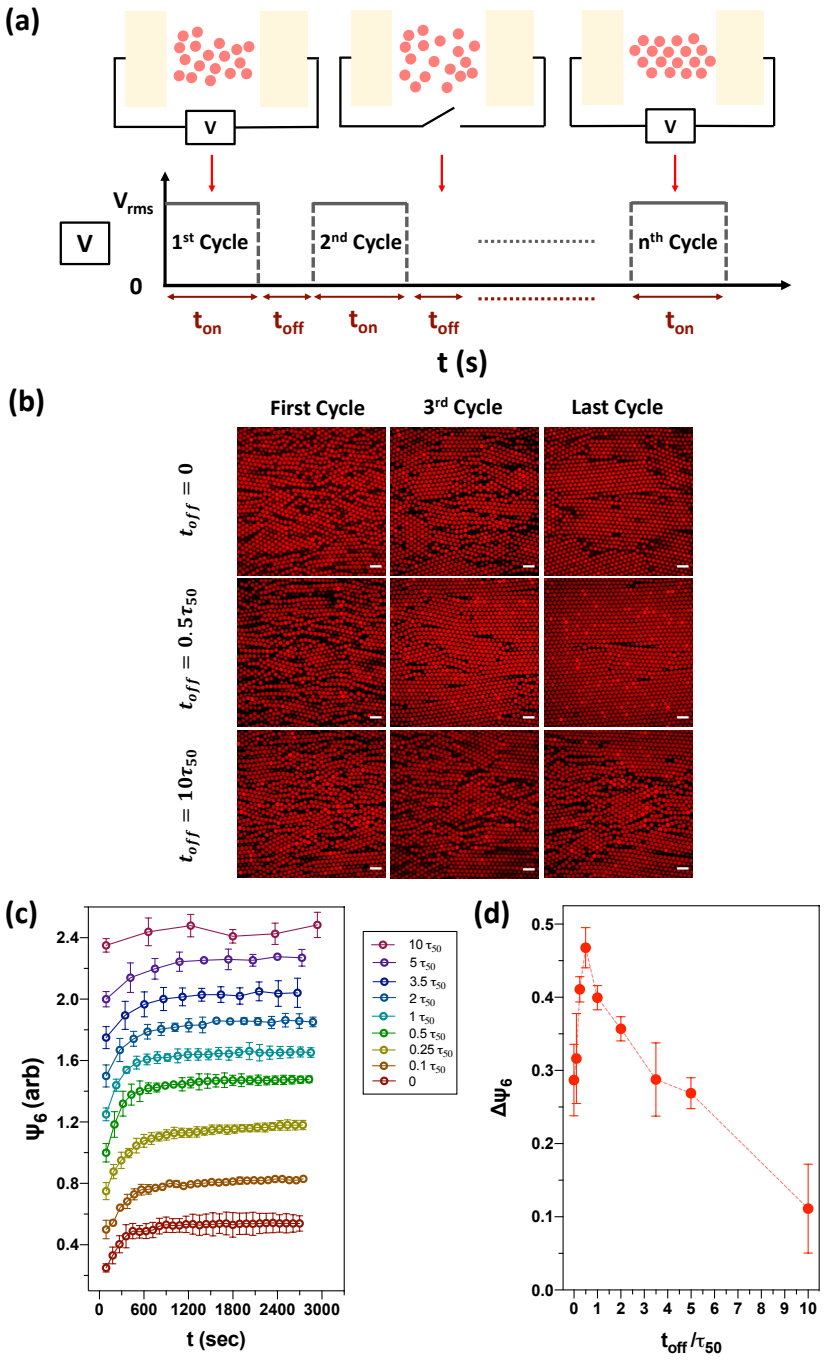

Figure 2.1 The impact of t_{off} on colloidal crystal quality in cycled electric fields experiments. (a) Schematic illustration of the experimental procedure for cyclic annealing of monolayer colloidal crystals. The electric field is initially turned on and maintained at V_{rms} = 8.0 V (E = 32 kVm^{-1}) and u = 5 MHz for t_{on}; the electric field is then off for a period of t_{off}. The applied field is cycled for a duration of 2700 s. (b) 2D confocal laser scanning micrographs of t_{off} = 0, 0.5τ_{50} and 10τ_{50} at the first, third and last cycle, respectively. (c) Time evolution of ψ_6 data for cycled fields experiments with nine different durations of off time. t_{on} = 90 s for all experiments. Data in (c) are offset for clarity. (d) Change in $\Delta\psi_6$ as a function of melting time ratio t_{off}/τ_{50}. The maximum $\Delta\psi_6$ occurs at $t_{off}/\tau_{50} = 0.5$. Scale bars in CLSM images are 10 μm.

The slope of $\Delta\psi_6$ vs t_{off}/τ_{50} is asymmetric about its peak, with larger (smaller) changes in annealing rate observed for small (large) t_{off}. Because it is t_{off} that is varied in Figure 2.1d, the configurational changes leading to $\Delta\psi_6$ are driven by diffusion (as opposed to configurational changes driven by the external field). The magnitude of these changes should scale with the magnitude of particle displacement due to diffusion. For annealing to be successful, there must be a sufficient number of particle displacements of sufficient distance. Small diffusive rearrangements (as occur for short t_{off}) may not allow the configuration of the crystal to meaningfully change, and therefore defects are not annealed. Conversely, we expect that there is an upper threshold for particle displacements beyond which too much disorder is generated in the system, also resulting in unsuccessful annealing.

We measured the two-dimensional short-time self-diffusivity of the colloids, D_s, to gauge the range of displacements that particles undergo during the field-off time. D_s can be determined from measurement of the mean-squared displacement (MSD), $\langle \Delta x^2(\Delta t) \rangle$ [56]. The MSD of all particles in the system during t_{off} was computed from particle trajectories, as determined by *Trackpy*[57]. An average of 1,000 particle trajectories per sample were measured and a small correction for drift applied. D_s is related to the MSD through $\langle \Delta x^2(\Delta t) \rangle = 4D_s(\Delta t)^{\alpha}$. In the case with best annealing performance, $t_{off} = 0.5\tau_{50}$, we find that $D_s = 0.013 \pm 0.002$ μm^2/s and $\alpha = 0.75$ (Figure 2.7a). Here, the scaling exponent α is smaller than 1, indicating particles behave sub-diffusively, a typical occurrence in a crowded system[58]. From these measurements, the average MSD of a colloid by $t_{off} = 0.5\tau_{50}$ in the cycle is 0.67± 0.06 μm. This value is 17% of the diameter of a particle.

Particle trajectories can be further be used to compute the ensemble-averaged van Hove distribution of particle displacements. The displacement distribution for three different lag times,

τ = 0.2s, 1s and 5s is summarized in Figure 2.7b. The van Hove probability histogram data is fit with a Gaussian function[59]. We find good overall agreement between the histogram data and the fitting. Therefore, the diffusion process during the field-off time exhibits a normal distribution and the van Hove function can be expressed as[60]:

$$G_s(\Delta x, \Delta t) = \sqrt{\frac{1}{2\pi\langle\Delta x^2(\Delta t)\rangle} exp\left[\frac{-\Delta x^2}{2\langle\Delta x^2(\Delta t)\rangle}\right]} \quad (2\text{-}2)$$

We then compute the displacement distribution with field-off time equal to $0.1\tau_{50}$, $0.5\tau_{50}$ and $10\tau_{50}$ (Figure 2.7c). Specifically, for the best annealing performance (field-off time equal to $0.5\tau_{50}$) we find that half of the particles diffuse less than 0.36 μm (which is less than 10% of the particle diameter) and only 6% of particles diffuse to 1 μm (which is one-half of the particle radius). These results suggest that displacements on length scales less than a single lattice spacing are optimal for annealing. When larger percentages of particles can move over length scales approaching the lattice spacing during each t_{off} period, annealing gains do not persist from cycle to cycle. Because the distance particles move on average is much smaller than the particle length scale, the coordinated motion of defects is a possible mechanism for the annealing effect. This scenario aligns well with a recent study of the dynamics of 2D crystals; in these cases, coordinated fluctuations of vacancies and interstitials are expected to play a critical role in melting[61].

2.3.2 Local defect rearrangement and kinetically arrested states

To study the coordinated motion of defects, we identify local defect rearrangements and kinetically arrested states of colloidal particles during cyclic annealing by computing Voronoi diagrams for the CLSM images. Voronoi diagrams were computed using the library *Qhull*[62]. Particles within three diameters of the image boundary were not counted when tallying defects (these particles may lack neighbors due to the finite size of the image). Figure 2.2a shows the

Voronoi diagrams of colloidal crystals that have been cyclically annealed at $t_{off}/\tau_{50} = 0.5$. These images were acquired at the end of each electric field-on period. Here, the gray cells represent particles with hexagonal neighbor shells while the red, yellow, light blue and dark blue cells represent four-, five-, seven- and eight-fold coordinated particles, respectively. The presence of topological defects – predominantly arrays of edge-sharing heptagon–pentagon dislocations – indicate the polycrystalline nature of the sample[63]. Many small crystal domains grow progressively between cycles and merge into larger single-crystal grains. By the conclusion of cycle 25, we observe two misoriented crystal domains separated by a low angle grain boundary ($\theta \sim 13.4 \pm 0.8°$). We also observe shrinkage of a closed grain boundary loop as time progresses (Figure 2.2a, top left corner). We find that the total fraction of six-fold Voronoi cells in sample snapshots evolves in a similar manner to the ψ_6 bond order parameter (See Figure 2.8). Furthermore, the concentration of vacancies observed in experiment decreases initially but becomes constant at long times. This reflects that the cyclic annealing procedure accelerates the approach of the system to its thermodynamic ground state, which may include non-zero vacancy concentrations.

To further understand how topological defects are removed by annihilation, we study defect formation and motion during the switch from field-on to field-off ("on to off") and vice versa ("off to on"). Figure 2.2b shows the transition Voronoi diagrams for colloidal crystals cyclically annealed at $t_{off}/\tau_{50} = 0.25$. We captured three types of structural rearrangements at different sites: recombination of defect pairs (indicated by a circle), generation of new defects (indicated by a square) and conserved defects (indicated by a triangle). This example implies that recombination of dislocations generated by cyclic field switching is an important annealing mechanism. During the "on to off" switch, the system creates defects, then in the next "off to on"

switch, those mobile defects (like dislocations) are driven by internal elastic forces to annihilate with preexisting immobile defects (like vacancies and grain boundaries). We observed that the motion of mobile defects can also be hampered by particle polydispersity, a nearby grain boundary, or multi-defect configurations that act as traps. As mobile defects are created, diffuse and annihilate with other defects, only a few kinetically arrested defects persist. Therefore, the efficacy of an annealing cycle depends on the creation of a limited number of mobile defects, which aid in annihilation, while avoiding the creation of additional immobile defects, which further reduce crystal quality.

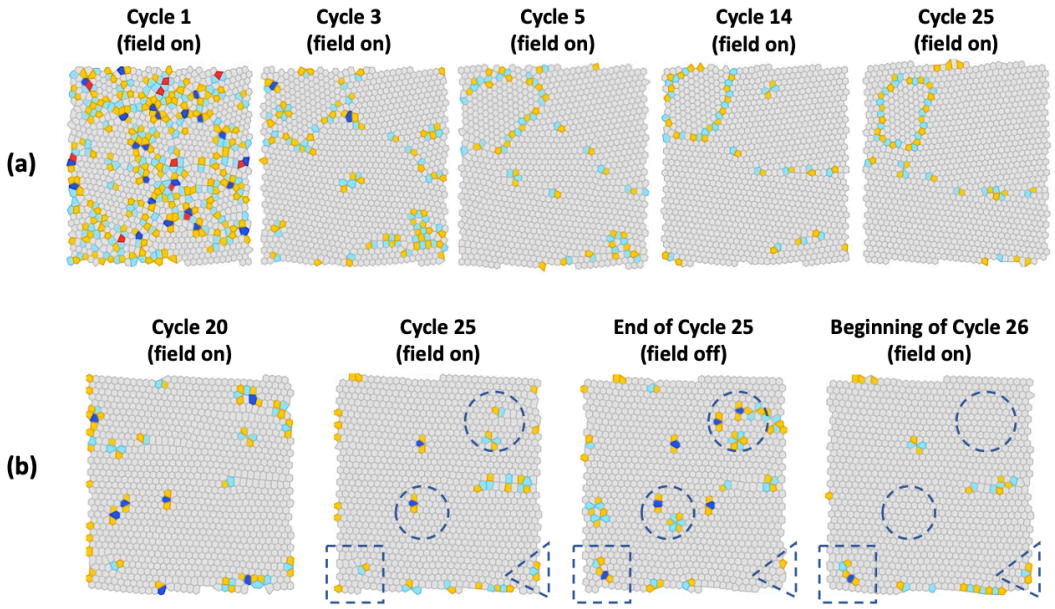

Figure 2.2 Voronoi analysis of colloidal crystals annealing. (a) Voronoi diagrams of experimental CLSM images under field-on condition with $t_{off}/\tau_{50} = 0.5$ at cycle 1, 4, 5, 14 and 25. (b) "On to off" and "off to on" Voronoi diagrams with $t_{off}/\tau_{50} = 0.25$ that show three types of defects rearrangement: recombination of defect pairs (circle), generation of new defects (square), and static defects (triangle).

2.3.3 Molecular dynamics simulation of the cyclic annealing of a colloidal monolayer

In order to study the effect of variable cycling time on monolayer annealing, we also employed a MD model of the field-assisted assembly process. We follow a similar protocol as in previous studies[55], in which particles under the influence of the driving field are simulated to represent induced polarization via discrete charges, with certain differences that are described in the Materials and Methods section.

In Figure 2.3a snapshots of simulated colloidal monolayers are shown for the first, third, and twentieth (last) cycles for different ratios of field-on to field-off. When expressed as fractions of the melting rate constant (calculated from a separate simulation), we find that a trend similar to experiments is observed. For constant field-on simulations, modest annealing of grain boundaries and vacancies occurs. For $0 < t_{off} <\approx \tau_{50}$ significantly accelerated annealing kinetics are observed. For $t_{off} \gg \tau_{50}$, the film can nearly or completely finish its melting to a fluid state within the off period of a single cycle. In this limit, the crystallization of each field-on period is uncorrelated with previous cycles and only the thermal annealing that can occur during the field-on time is seen.

This observation can be quantified for simulated systems in the same manner as for experimental monolayers. Figure 2.3b shows the value of ψ_6 for a variety of t_{off} conditions. Data points represent individual cycles, and error bars are the standard deviation of the mean as calculated from multiple locations within each simulated layer (see Figure 2.9 for additional data). As t_{off} approaches $0.5\tau_{50}$, the improvement of ψ_6 after several cycles increases. For larger t_{off} values however, the improvement in ψ_6 decreases, eventually approaching a flat curve with no improvement for $t_{off} = 10\tau_{50}$. This trend reproduces the behavior of the experimental films (Figure 2.1c). Furthermore, we find that the optimal annealing off time

(t_{off}/τ_{50} = 0.5) is insensitive to the microscopic details of the MD particle interaction model. Several models with different charged interaction strengths, isotropic particle attraction strengths, and electrophoretic force strengths were tested (Table 2.1), and the effect on system melting and freezing timescales is shown in Figure 2.10.

In our system, the dominant interaction driving self-assembly is the particle–particle dipolar interaction, consistent with reports in the literature for comparable systems[9,10,64,65]. As per the simulations, this dipolar interaction at contact is of scale 100 k_BT. Applied AC electric fields such as used here have the advantage of permitting high electric field strengths while minimizing the effects of water electrolysis or electro-osmotic currents. There is some dielectrophoretic contribution to the self-assembly, as demonstrated by the fact that particle densities are highest at the midplane of the device; this contribution is included at a level that is about a factor of ten smaller than the dipole-dipole coupling. We emphasize that the general method of annealing advanced here is independent of the specific means by which the interaction strength is varied. Even in systems where attractions are not the result of induced polarizations, we propose that cycled annealing schemes can accelerate crystal quality.

Although the trend in ψ_6 is consistent between experiments and simulations, a notable difference between the two is the specific shape of the ψ_6 curves over the duration of the cyclic annealing. This can be seen by comparing the $t_{off} = 0$ curves from Figure 2.1c and Figure 2.3b. In the experimental case, the ψ_6 curves quickly reach a plateau and remain steady. In contrast, the simulated layers display an initial logistic rise in ψ_6 followed by a nearly linear increase at long times, especially for $t_{off} \sim 0.25 - 0.5\ \tau_{50}$. Thus Equation (2-1) has a reduced quality of fit for simulated data in this t_{off} range. This gradual rise indicates that annealing is still progressing at a measurable rate in the steady field-on condition for the simulations, unlike in the

experiments. One possible interpretation of this trend is that low energy re-arrangements are occurring in simulations that are kinetically arrested or otherwise inaccessible in experiments.

How might low-energy arrangements proceed differently in simulation and experiment? We find that the strength of damping in the Langevin thermostat, as well as the energy scale of the interparticle attractions, are key variables controlling this long-time behavior. Langevin damping applies a drag force that is proportional to particle velocity. This parameter also controls, for instance, the terminal speed of particle settling in the simulation. For weaker damping and milder interparticle attraction, a greater rate of long-time annealing was seen. As our simulations lack frictional forces for particle-particle contacts, all dissipation occurs through the influence of the damping term. This velocity-based damping is always present, not only when particles are in contact. Frictional contact between particles would provide an additional barrier to the particle rearrangements needed for defect annealing and migration. Colloidal interparticle dissipation due to lubrication and viscous coupling has been measured[66]. This effect, along with direct particle-particle contact, due for example to surface roughness, have implications for the dynamics of dense suspensions[67,68] and colloidal glasses[69]. Because Langevin damping is a global effect (and not confined to particle contacts) we were unable to fully explore the effect of particle-particle frictional interactions on annealing kinetics without also affecting other transport timescales in simulation.

An additional difference between the experiments and the simulations is that the latter lacks hydrodynamic interactions (HI) between the particles. HI is expected to not have a significant role on the equilibrium assembled structures but rather on the movements of the particles. HI complicates the relationship between structural and dynamic properties by having effects on both self- and collective diffusion of colloidal particles in suspensions[70]. For a 2D

colloidal suspensions, Falck et al. reported the collective-diffusion coefficient is strongly coupled to HI[71]. It is possible that colloids in our experimental system undergo faster collective diffusion and reach kinetically arrested states faster. However, despite the difference in the origin of dissipation, the response of the systems to cycling is similar.

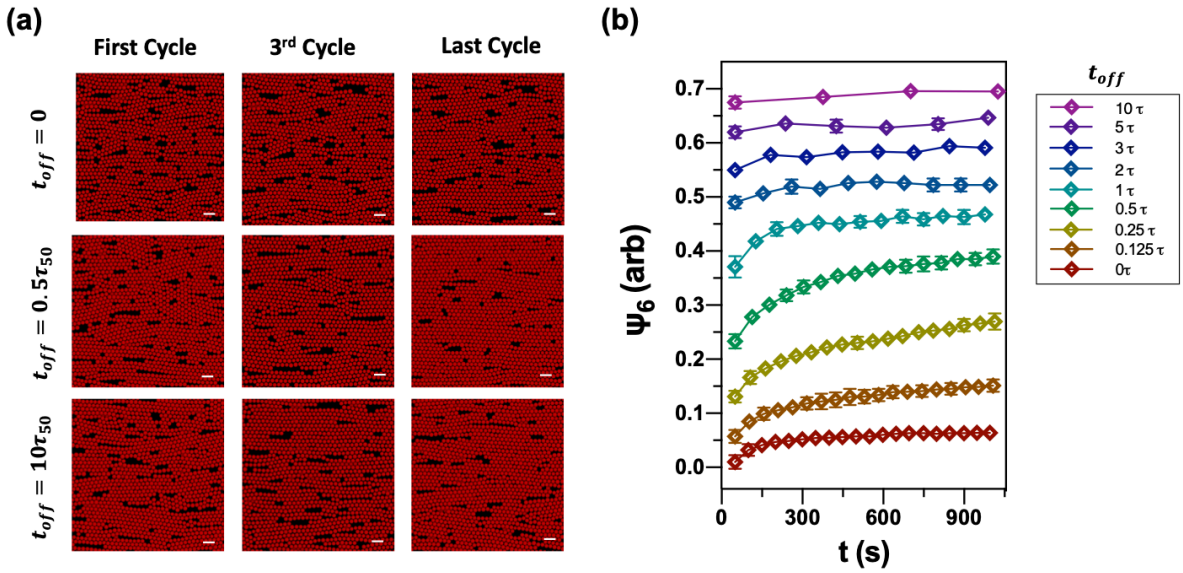

Figure 2.3 The impact of t_{off} on colloidal crystal quality for simulated systems. (a) Images of simulated spheres assembled into dense crystals with t_{off} = 0, $0.5\tau_{50}$ and $10\tau_{50}$ at the first, third and last cycle, respectively. (b) Time evolution of ψ_6 data for cycled-fields simulations with nine different durations of t_{off}. Data in (b) are offset for clarity. Scale bars in images are 10 μm. This data over the full range of long-cycle times can be found in Figure 2.9. These MD simulation data were collected by B. J. VanSaders.

2.3.4 Small angle light scattering

We demonstrate the annealing of monolayer colloidal crystals and the kinetics of global annealing by SALS. Specifically, we measure the light scattering patterns at the optimal annealing condition, as per Figure 2.1d. Figure 2.4a shows the time evolution of the SALS data. In the first cycle, we observe a six-fold symmetric light scattering pattern. The diffuse

appearance of the light scattering pattern implies the formation of polycrystalline close-packed structure, each crystallite with a different orientation. In the fifth cycle, both the 1st and 2nd order scattering peaks can be clearly observed, indicating that a single crystal is developing on the scale of the scattering volume. The locations of these peaks represent the reciprocal lattice for a hexagonal close-packed (hcp) monolayer[72]. In the later cycles, such as cycle 15 and cycle 25, we are able to observe the 3rd order scattering peaks, which indicate that the single crystal is of increasingly high quality. We also observe a scattering pattern at low scattering wavevector (q, Materials and Methods Section) oriented along the direction of the electric field. This scattering is a consequence of the device geometry. Upon the application of the electric field, long-range gradients in particle density are formed along the electric field direction between the electrodes, thereby introducing low q scattering features[55].

The characteristic lattice spacing (σ_i) can be obtained from the SALS data based on the reciprocal relationship $q = 2\pi/\sigma_i$, where σ_i represents the real-space distance. In Figure 2.4a, σ_i is 4.91 ± 0.04 μm at the first cycle and 4.92 ± 0.03 μm at the 5th cycle. As time progresses, σ_i becomes 4.87 ± 0.07 μm at the 15th cycle and 4.86 ± 0.06 μm at the 25th cycle. The results show that the crystal quality improves without appreciable change in the average particle separation.

We analyzed the intensity of peaks in the first ring of the light scattering pattern to quantify crystalline order. Greater peak intensity represents higher quality global ordering of the monolayer crystal. Figure 2.4b compares the time-evolution of the SALS peak intensity I and CLSM local order ψ_6 for t_{off}/τ_{50} = 0.5. During the annealing process, both peak intensity I and local order ψ_6 increase monotonically as a function of time. By applying Equation 2-1 to each data set, we determined k_{SALS} and k_{CLSM}. The rate constant of local order annealing, $k_{CLSM,0.5}$, is 0.0044 s^{-1} and the rate constant of global order annealing, $k_{SALS,0.5}$, is 0.0028 s^{-1}, respectively.

Our results show that short-range ordering achieves steady-state faster than long-range ordering. Therefore, local restructuring leads global annealing; the local rate is about 50% greater than the global rate.

To investigate the lag between local ordering and global ordering, an expanded real-space view of the annealed crystal was acquired by CLSM (image size of 250μm x 600μm). Figure 2.4c shows representative CLSM results during the field-on phase with $t_{off}/\tau_{50} = 0.5$. Although the size of these CLSM images is smaller than the beam size of the SALS device, they can be used to gain insight into the mechanism of crystallite growth that drives the global crystal quality characterized by CLSM. From cycle 2 to cycle 8, there are many small to medium sized crystallites separated by grain boundaries. After cycle 15, a significant reduction in the number of dislocation and grain boundaries was observed.

Six-fold coordinated particles are shown in Figure 2.4d colored by grain membership. The identification and characterization of crystalline grains are described in the Materials and Methods section. Many misoriented grains in cycle 2 merged into two main crystallites in cycle 8, where they gradually coarsen to one crystal after cycle 15. The early stage misoriented grains contribute to the spread in the light scattering diffraction peaks. Finally, we calculate the number of particles in each grain, *N*, and plot the distribution of *N* for each cycle in Figure 2.4e. The histograms show similar distributions after cycle 15, indicative of the appearance of steady ordering in large grains. Based on the above analyses, we can conclude that the vast majority of particles formed local six-fold packings within misoriented grains in early cycles, followed by the merging and reorientation of those grains into large domain, perfect crystals. It is the lag in the annealing of the misoriented grains that generates the retarded kinetics of the (global) scattering relative to the (local) CLSM orientational ordering.

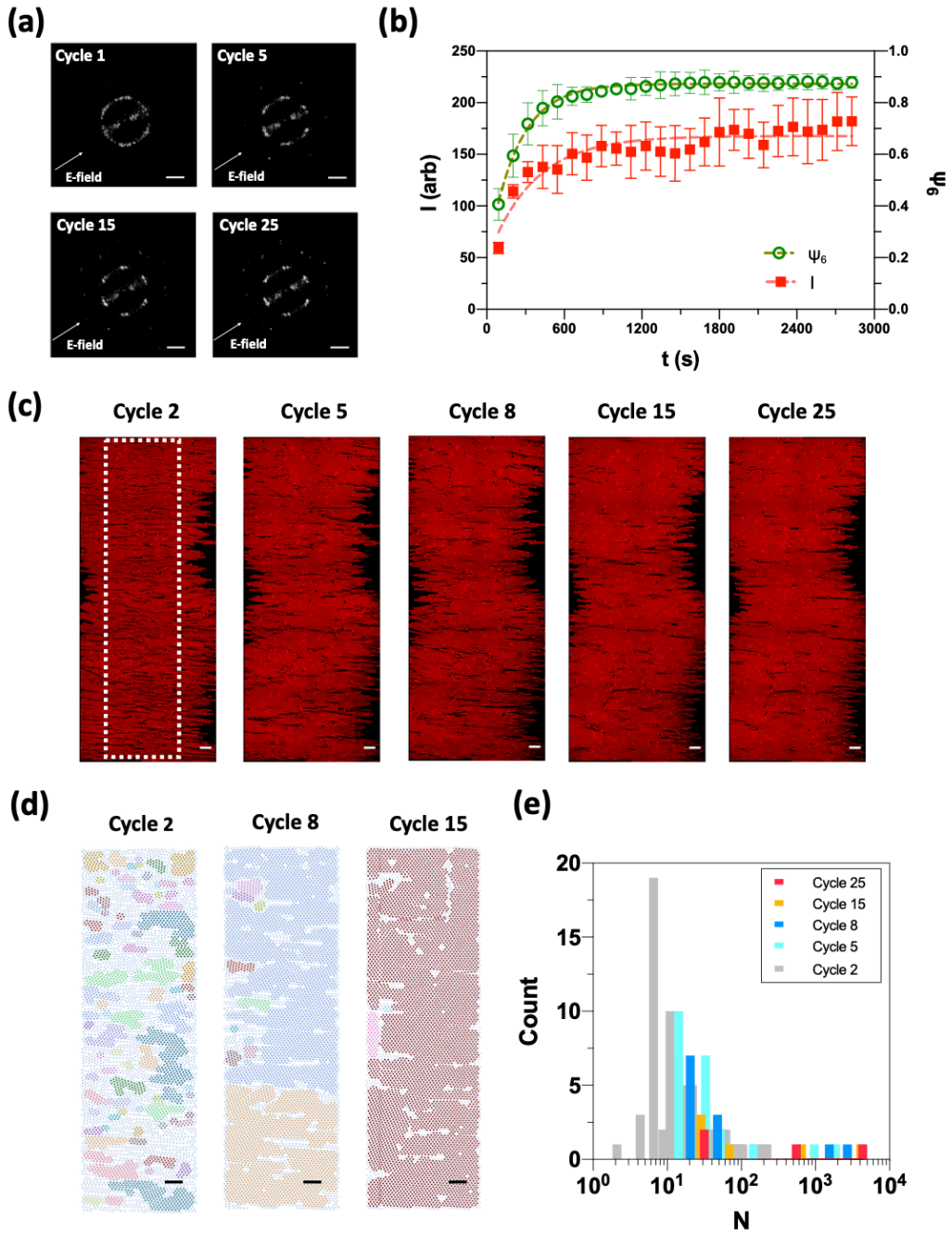

Figure 2.4 Local and global ordering characteristics of spheres under cyclic electric fields of $t_{off} = 0.5\tau_{50}$. (a) SALS images for cycle 1, 5, 15 and 25, respectively. (b) The change of peak intensity of light diffraction responses and the change of ψ_6 as a function of time t. The curves plotted are the mean and standard error of the mean for five and three CLSM and SALS experiments, respectively. (c) 2D confocal laser scanning micrographs for cycle 2, 5, 8, 15 and 25, respectively. The white dotted line encloses the centerline region for analyzing the distribution of crystalline grains. (d) Crystalline grains identified by particle proximity and local ψ_6 phase angle at the device centerline region for cycle 2, 8 and 15,

respectively. (e) Histogram of the grain size (N) characterized for cycle 2, 5, 8, 15 and 25, respectively. Scale bars in SALS images are $q = 1\ \mu m^{-1}$. Scale bars in (c) and (d) represent 20 μm. The algorithm to identify crystal grain as reported in (d) was developed by B. J. VanSaders.

2.3.5 Thermostat energy flow during cycled assembly

Over the course of cyclic annealing simulations, energy flow can be tracked into and out of the system. The Langevin thermostat that is used to maintain a constant temperature is also used to record energy flow between the system and a heat bath to which it is coupled. As the field condition is changed, kinetic energy must be added (in the case of field-on) or removed (field-off) in order to maintain a constant temperature. This energy flow indicates the total sum of work being done on the system by all sources. In this case those sources arise from the cycled field. We find that cycling conditions that lead to rapid annealing have the greatest rates of thermostat heat flow (dE/dt) into the system during the beginning of each cycle. For t_{off}/τ_{50} near 0.5, the drift in the configuration of the monolayer is such that a large quantity of work is done quickly to order the system – furthermore, the system is able to access lower energy configurations on each subsequent cycle. These observations indicate the specific nature of the coupling between the applied cyclic field, the dissipation by the monolayer, and the resulting configurational change as indicated by ψ_6.

For cycling times that couple weakly to the dynamics of the monolayer ($t_{off}/\tau_{50} < 0.25$ or $t_{off}/\tau_{50} > 1.0$), the rate of work (i.e., structural change to the configuration of the monolayer) is low. For $t_{off}/\tau_{50} < 0.25$, only small changes to the configuration of the film have occurred during the field-off time, and so under field-on conditions only a small amount of work over a short time is done on the system to order it (Figure 2.5a). Conversely, for $t_{off}/\tau_{50} > 1.0$, the monolayer's configuration has changed a great deal during the field-off time. When the field is

switched on, the system slowly navigates a kinetically arrested energy landscape to return to the ordered state.

In Figure 2.5a we plot the changes in order parameters for simulated systems as a function of t_{off}/τ_{50}. The change in ψ_6 is most sharply peaked around t_{off}/τ_{50} = 0.5, and rapidly falls off to a low baseline at t_{off}/τ_{50} = 10. The SALS peak intensity follows a similar trend, while showing a broader peak distribution. We interpret this to be a result of the long-range (and therefore many-particle) nature of the SALS measurement. That is, for large t_{off}/τ_{50} local order around any given particle is not improved by cycling. However, long-range correlations, such as probed by SALS, are still impacted for such cycling. These long-range correlations (SALS) might be due to the correlations between the orientations of grains, which can develop because of the tendency of the field to favor alignment of the close-packed crystal directions. This effect is only observable at the scale of the entire system (i.e., via SALS). See Figure 2.4c for examples of such grain alignment).

We also observe that the exchange of energy between the integrator and the particles in the simulated system is, unlike the other measures, peaked at t_{off}/τ_{50} = 0.25 (Figure 2.5a). The energy exchange rate is the most local of the three measures, being dominated by nearest-neighbor interactions. That is, the heat flux from the system to the bath involves contributions from each of the two-body interactions between the particles. The local ψ_6, by comparison, requires the coordination of six neighbors around a particle. SALS further includes sensitivity to long-range correlations. From this data we see a general trend that short field-off times preferentially anneal pair-wise correlations in the monolayer, whereas larger field-off times affect more highly coordinated structures.

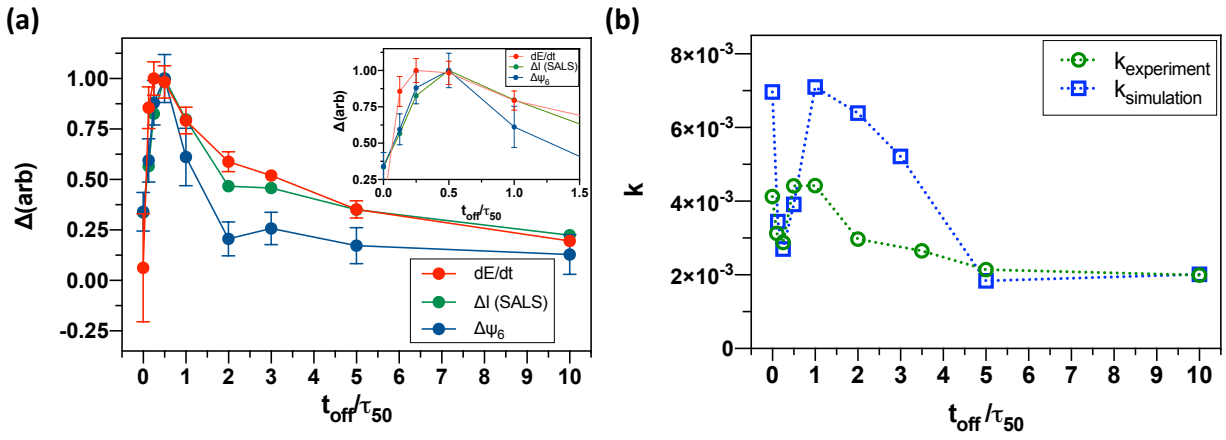

Figure 2.5 Performance and kinetics of colloidal crystals annealing as a function of melting time ratio t_{off}/τ_{50}. (a) Relative changes of system order parameters as a function of t_{off}/τ_{50} for simulated systems. The difference of local order (ψ_6) and global order (I) are shown alongside rate of energy exchange with the Langevin thermostat. (I is measured by simulated SALS.) The change in ψ_6 is most sharply peaked around t_{off}/τ_{50} = 0.5. SALS peak intensity shows a somewhat broader peak distribution. Energy exchange rate with the thermostat is also broad; it furthermore shows a shift in peak position to t_{off}/τ_{50} = 0.25 (inset). (b) Relative changes of annealing rate constant k as a function of t_{off}/τ_{50} for both simulated systems and experiments. Here k has units of s^{-1}. The MD simulation data were collected by B. J. VanSaders

2.3.6 Annealing kinetics

Previous computer simulations suggest that the operation of a cyclic field offers a simple and easily controlled scheme for creating colloidal crystals at a faster rate compared with steady-state assembly[39]. In Figure 2.5b we demonstrate the impact of t_{off} on the annealing rate constant, acquired by fitting Equation (2-1), for both experiments and simulation (see Figure 2.11 for examples of simulated data curves). For the experimental results, the maximum annealing rate appears at t_{off}/τ_{50} = 1. (Note in Figure 2.5b that the larger the value of k the faster the dynamics of annealing.) A slightly lower annealing rate is observed at t_{off}/τ_{50} = 0.5, the condition that has the best annealing performance. A high rate constant also appears at t_{off}/τ_{50} = 0. Recall that this is the steady field condition. By comparison, as per the results of

Figure 2.1d, the crystal quality measure $\Delta\psi_6$ is comparatively low at $t_{off}/\tau_{50} = 0$. These two results, taken together, indicate that spheres assembled under steady electric fields crystallize quickly; however, these structures are not high quality. The strong attractive forces that are induced by the field drive rapid crystallization, but do not promote reconfiguration and defect diffusion that supports further improvement in crystal quality. On the other hand, the simulations show that high quality crystals assembled at the optimal cyclic condition have lower k and therefore slower kinetics.

Figure 2.5b shows that similar trends in kinetics are present for both the experimental and the simulated systems, yet with quantitative differences observed near the optimal annealing condition. The magnitudes of the simulated rate constants are generally larger than those from experiment, with the exception of times near the optimal annealing cycling timescale ($t_{off}/\tau_{50} = 0.5$). Near this region, the simulated annealing rate constants are reduced even more than the experimental ones. We interpret this result as follows: Due to the lack of frictional damping in simulations, they generally display faster particle dynamics. However, near the optimal annealing timescale, the simplified simulation model experiences a kinetic slowdown that is ameliorated by other factors in the experimental case. Although this remains a hypothesis, we propose that such a factor might be HI between particles.

The interpretation of the complex annealing kinetics behavior for experimental and simulated systems are as follows: The low annealing rates present near the optimal cycling timescale suggest that local configurational changes in the monolayer at these timescales are delaying the rise of ψ_6 without negatively impacting its eventual magnitude. Additionally, the trend of high rate constants at low t_{off}/τ_{50} is expected for the following reason: For short field-off times, the local particle configurations do not have enough time to significantly reconfigure.

Therefore, when the field is turned on, the previous close-packed configurations are quickly recovered. Similarly, slow kinetics at large t_{off}/τ_{50} is also expected. At these conditions the local ordering of particles has sufficient time to relax to the fluid structure, and so when the field is turned on the close-packed configuration must be rebuilt from a completely disordered fluid state.

In conclusion, we have shown that colloidal monolayers assembled under AC electric fields exhibit significantly improved crystal quality under certain cyclic conditions. By using a local probe of structural order (CLSM) as well as a bulk measurement (SALS), we found that local ordering generally precedes global re-arrangement in this system. For both experiments and computer simulations we find that the cycling timescale that produces the highest quality crystals is similar to the fundamental characteristic timescale of crystal melting (t_{off}/τ_{50} = 0.5). By investigating the timescale of order parameter growth ($\Delta\psi_6$), the rearrangements and annihilation of mobile defects, and the heat exchange between the simulated system and thermostat, we find evidence that cycling timescales near t_{off}/τ_{50} = 0.5 activate coordinated reconfiguration mechanisms that progressively improve crystal quality over approximately 15 cycles. Our results suggest a general principle to design annealing by cycling induced potential interactions between particles. The cyclic conditions are optimized at a time that is approximately the characteristic melting time of the system. Future work could extend the annealing strategy developed in this report to encompass crystallite length scales greater than those investigated here (~ 250 μm), so as to address the dimensions needed for large-scale applications in fabrics, vehicles, and structures.

2.4 Materials and Methods

2.4.1 Experimental design

A monolayer of colloidal polystyrene spheres (F8858, Invitrogen) was introduced in the coplanar AC electric field device, as shown in Figure 2.12. The device was prepared by deposition of Ti/Au electrodes onto a glass substrate, followed by cleaning the device in a freshly prepared base bath (1N potassium hydroxide solution in isopropanol, Fisher Scientific) for thirty minutes before use. The electric field is cycled between t_{on} and t_{off} by means of an AC power source (RIGOL, DG1022). During t_{on}, a square wave with constant V_{rms} 8.0 V and frequency 5 MHz was applied across the 250 μm gap between the electrodes, creating an electric field strength of 32 kVm^{-1}. The electric field device is 1 mm in height, and it took one hour for particles to complete sedimentation. The initial number of colloids per unit surface area is 0.055 spheres μm^{-2}, as determined by hemocytometry (NanoEnTek Inc.).

2.4.2 Characterization of the colloidal assembly structure

CLSM is used (Nikon A Piezo z-drive, 100x, NA = 1.45 oil immersion objective) to visualize the particle-level microstructure. The image size is 512 x 512 square pixels, and the pixel size is 250 x 250 nm^2. The centroid of any given particle in the images is identified with a resolution of ±0.07 μm by means of the MATLAB circle detection function *imfindcircles*. To quantify the crystallinity, we calculated the six-fold bond orientational order ψ_6. For each spherical particle, $\psi_{6,j} = \frac{1}{N_j}\sum_{k=1}^{N_j} e^{i6\theta_{jk}}$ is computed based on N_j of nearest neighbors within the first peak of g(r), where θ_{jk} is the angle between a sphere j and its neighbor k with an arbitrary reference direction[73]. This analysis utilized the *freud* library[74]. We note that at this magnitude and frequency of applied electric field the colloids also undergo dielectrophoresis in addition to

crystallization. The colloids are therefore more concentrated at the centerline between the two electrodes. In this study, we conducted microstructure characterization at the centerline region.

Colloidal particles are grouped into grains by clustering over a vector of their positions and ψ_6 phase angle (using the DBSCAN clustering algorithm[75]). We used a normalization where close-packed particles with no phase angle have a metric distance of 1. Clusters with a maximum member metric distance of 1.25 were computed. This value was found to produce good separation of grains; only nearest neighbors are considered as grain members (second nearest neighbor distance with no rotation under this metric is $\sqrt{3}$), and orientational differences must be small. This procedure is an adaptation of Gray et al.[76]. Six-fold coordinated particles are colored by their grain membership.

2.4.3 Analysis of light scattering response

SALS is used to quantify the global order of the colloidal crystal. The design of the SALS device is as in Kao et al.[55]. A laser (JDS Uniphase, 1135P) of wavelength 632.8 nm with a $1/e^2$ diameter of 0.71mm was used as the light source. The analyzed radial width of the light scattering pattern was set to be 20 pixels to match the average width of the primary scattering patterns, which was 20 ± 3 pixels. This analyzed region corresponds to a scattering wavevector $q = 1.34\ \mu m^{-1}$ in the radial direction and radial width $\Delta q = 0.17\ \mu m^{-1}$. Here, the scattering wavevector, $q = \frac{4\pi n}{\lambda} \sin\left(\frac{\theta}{2}\right)$, is equal to the difference between the incident wavevector and the scattered wavevector, where n is the effective refractive index of the sample and λ is the wavelength of the incident light. We then used locally weighted least squares smoothing (LOWESS) to fit the intensity data as a function of azimuthal angle to a Gaussian peak after baseline correction. The LOWESS peak intensity is used to quantify the light scattering response.

2.4.4 Molecular dynamics simulation[3]

MD simulation of cyclic, AC-electric field assisted self-assembly was conducted using HOOMD-Blue (v2.0)[77–79]. The interaction potential between particles is split into two components; a hard-sphere like repulsive force, represented by a Shifted Lennard-Jones potential[80], and a screened dipole-like interaction represented by two discrete charge centers located within the interior of the repulsive particle core. The Shifted Lennard-Jones potential takes the form:

$$V_{SLJ}(r) = 4\epsilon \left[\left(\frac{\sigma}{(r-\Delta)}\right)^{12} - \left(\frac{\sigma}{(r-\Delta)}\right)^{6}\right] \quad (2\text{-}3)$$

For $r < r_{cut} + \Delta$, and zero for larger distances. In this study $\sigma = 0.5$, and Δ was chosen so that the potential minima lay at $r = 2^{1/6}$ in simulation distance units. The potential was truncated at $r_{cut} = 2^{1/6}$, and shifted in energy so that $V_{SLJ}(r = r_{cut}) = 0$. For this interaction, $\epsilon = 1$. These choices result in a potential that is purely repulsive and behaves more similarly to a hard sphere than the traditional Lennard-Jones potential with $\sigma = 1$ [81].

Particle interactions which modeled the effect of polarization were manipulated to represent the cyclically applied field. The discrete charge representation for the dipolar interaction follows the implementation of Crassous et al., which assumes that particle polarization due to the applied AC field is instantaneous and homogenous over the volume of the simulation[82]. Also included was an isotropic, short-ranged interparticle attraction, represented by a Shifted-Lennard Jones potential with $r_{cut} = 2.5 * 2^{1/6}$, and $\epsilon = 2$. This isotropic attraction, as

[3] The molecular dynamics methods were developed and documented by B. J. VanSaders.

well as the anisotropic attractions due to screened dipole forces are the 'polarization-induced' interparticle forces used in this study.

The hard core and two charge-representing particles were simulated as a rigid body[83], but without rotational freedom. This is because we assume the polarization direction of the particles to be fixed by the applied AC field direction. In the field-on condition, particles interacted via both hard-core repulsion and polarization-induced charge interactions. In the field-off condition, only the hard-core repulsion was simulated. All simulations employ Langevin integration at constant temperature. Particle masses are chosen to match 4μm polystyrene particles. No hydrodynamic interactions between objects were considered explicitly in these simulations.

Particles were induced to settle onto a repulsive plane (with normal in the z-direction) by a constant force (with the strength of the gravitational force on 4μm diameter polystyrene particles immersed in water at room temperature). In addition, in the field-on state a one-half wavelength sinusoidal potential of depth 8 k_bT was applied across the simulation domain, parallel to the direction of particle polarization. This potential represents the effect of dielectrophoretic forces which drive particles towards the center of the device.

For each run 10,000 particles were simulated. To determine the crystallization and melting rate constants, simulations of duration equivalent to 150 seconds were performed and SALS curves fit according to the methods of Kao et al.[55]. Notably, we use here charge mediated interactions (of strength 100 k_bT) between particles that are significantly stronger than in reference[55]. This large interaction strength was necessitated by the large size of the particles used in this study. For $4\mu m$ diameter polystyrene particles immersed in water at room temperature, the energy of raising a particle by its own diameter against gravity is in excess of 10 k_bT. This interaction strengths brings the kinetics of the simulation into close agreement with observation

(for simulations crystallization τ_{50} = 12.8 ± 1.2 s, compared to experimental τ_{50} = 14.8 ± 0.9 s). At these parameters, maintaining the field-on conditions for several τ_{50} yielded dense, polycrystalline monolayer films. Crystal grains within these films have characteristic sizes of approximately 10 particle diameters, similar to experiment. A system size of 10,000 particles therefore allowed several dozen to 100 grains to be observed simultaneously.

In the cyclic simulations, systems were held for 4.5 crystallization half-life times in the field on state, then in the off state for various fractions of the melting rate constant time. In addition to simulated SALS spectra, ψ_6 was calculated using the analysis package *freud*[74]. Similar to in the experimental case, several circular regions of radius 1200 mm near the dense center of the simulation domain were selected and averaged to obtain ψ_6. Lastly, the energy exchange with the Langevin thermostat was logged during numerical integration.

2.5 Supplementary Information

2.5.1 Area fraction of assembled structures

The area fraction of spheres (d_{2D}) value represents how many colloidal particles assembled in the characterized region. A completer comparison of d_{2D} changes as time progresses with t_{off} = 0, 0.5τ_{50}, and 10τ_{50} is reported.

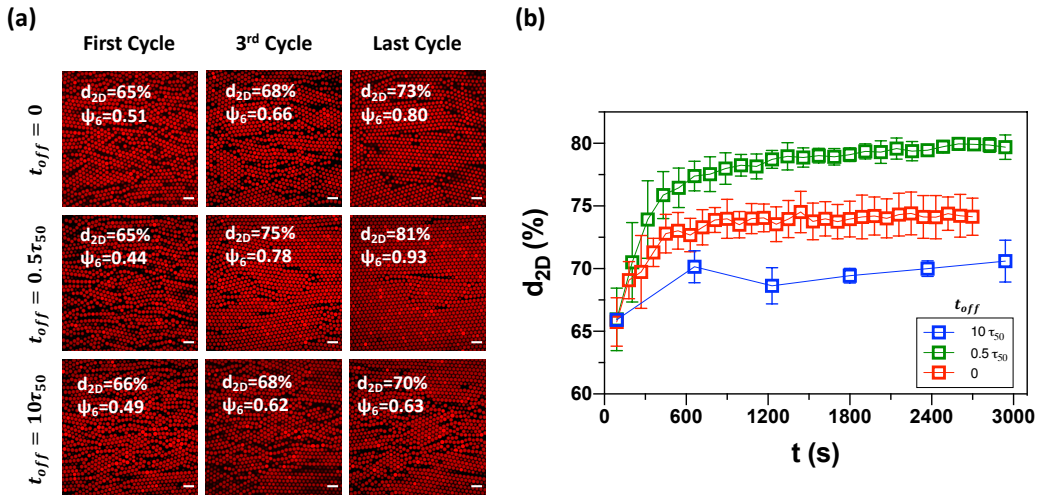

Figure 2.6 The change of area fraction of the colloids as time progresses. (a) Confocal laser scanning micrographs with calculated ψ_6 value and area fraction of spheres (d_{2D}) value for t_{off} = 0, $0.5\tau_{50}$, and $10\tau_{50}$ at the first, third, and last cycle, respectively. (b) Time evolution of d_{2D} for t_{off} = 0, $0.5\tau_{50}$, and $10\tau_{50}$. Scale bars in images are 10 μm.

2.5.2 Diffusion of particles during the field-off time

Under the best annealing performance condition $t_{off} = 0.5\tau_{50}$, there are about 6% of the particles diffused at a distance greater than 1μm during each field-off period (which is only half of the particle radius).

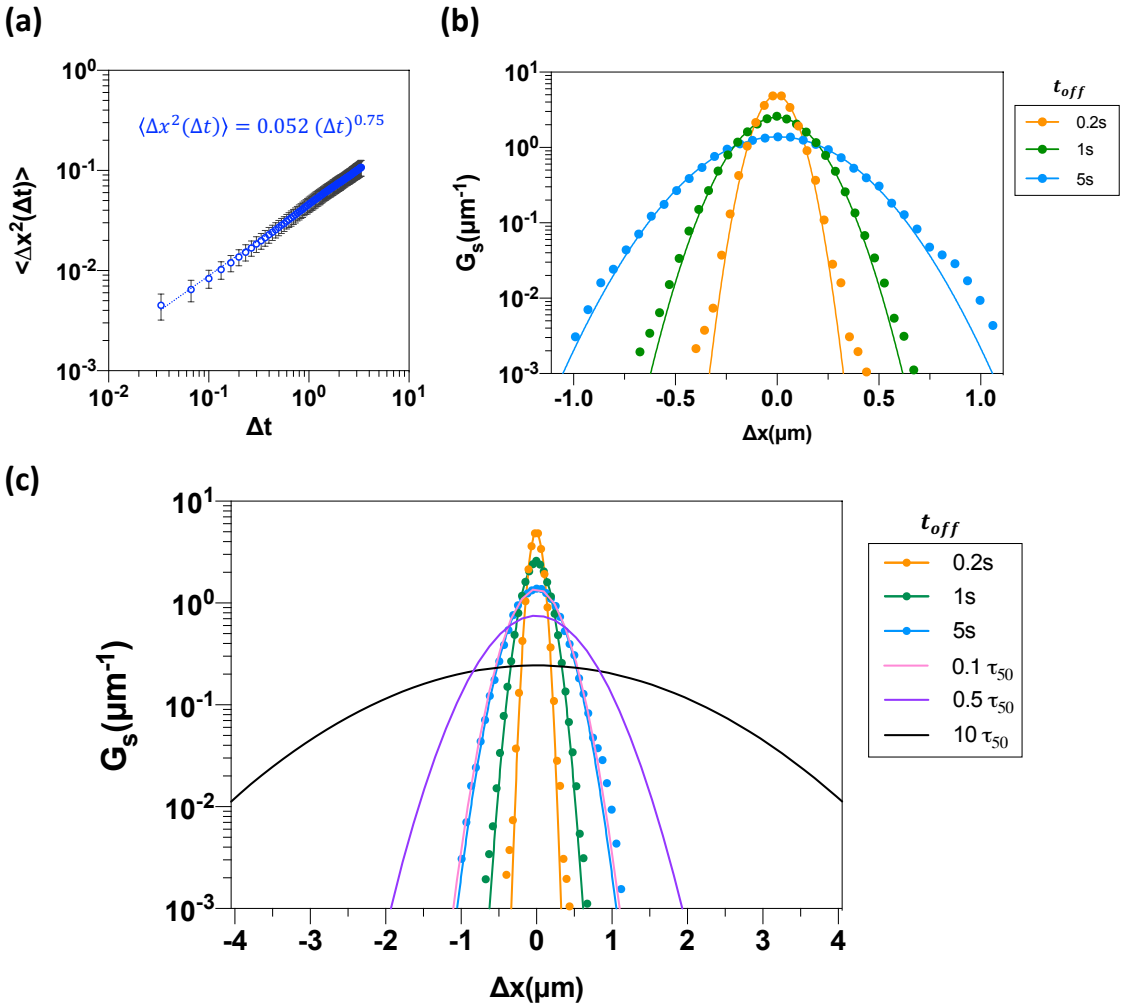

Figure 2.7 Two-dimensional short-time diffusion of particles under cyclic electric fields. (a) The MSD of particles in the first 10 s during field-off. (b) The van Hove distribution of particles in the first 0.2 s (orange), 1 s (green) and 5 s (blue) during field-off. (c) The computed displacement distribution based on Gaussian dynamics – as indicated per panel (b) – for field-off time equals to $0.1\tau_{50}$(pink), $0.5\tau_{50}$(purple) and $10\tau_{50}$ (black). Error bars are standard deviations from independent measurements.

2.5.3 Voronoi defect evolution

We track sample-wide changes to the number and area belonging to Voronoi defects for experiment and simulation. Defect area (A_{defect}) is defined as the summed area of all non-six-sided Voronoi cells. Additionally, the average area of all six-sided Voronoi cells is found (A_{ave}). The excess area belonging to defective particles is then approximated as: $A_e = A_{defect} -$

$N_{defect}A_{ave}$. The quantity $\frac{A_e}{A_{ave}}$ then approximates the number of additional particles which could be added to the system if defective particles occupied the same area as non-defective particles. Expressed as a fraction of total snapshot particles, the quantity $f_{excess} = \frac{A_e}{A_{ave}N_{total}}$ is shown in Figure 2.8 (row a) for simulation (column i) and experiment (column ii). Simulations begin with a smaller fraction of excess area belonging to defective particles than experiments, and that area does not change much over the course of annealing. In contrast, experimental samples begin with a larger defect area and experience a reduction in defect area for annealing protocols which also improve the other measures (SALS, ψ_6) measured in this study. Together these results indicate that the proposed annealing strategy is effective at accelerating the approach of the system to a baseline defect concentration. The value of the baseline concentration is controlled by the thermodynamics of the crystalline state, and therefore we do not expect it to be modified by the annealing procedure. Figure 2.8 row b shows the fraction of six-sided Voronoi cells observed in snapshots during annealing. The fraction of six-fold Voronoi cells ($f_{6-sided}$) grows in a similar fashion to others measures of crystal quality.

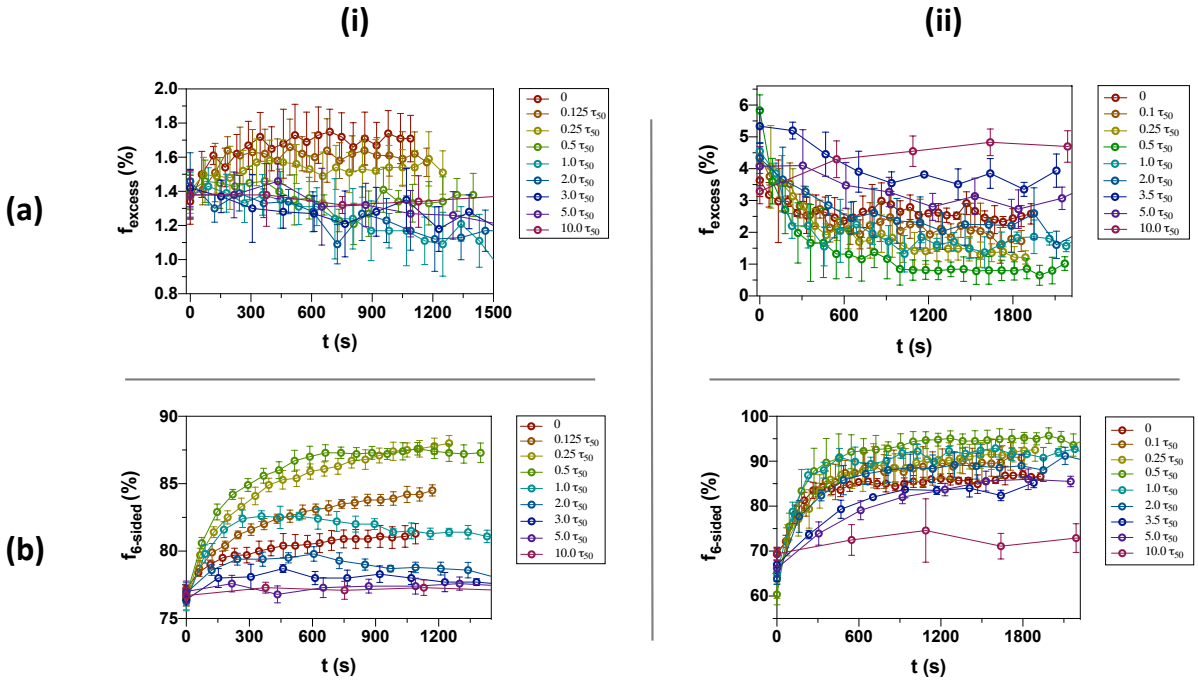

Figure 2.8 Evolution of defect and six-fold Voronoi cells during cyclic annealing. Row (a) excess area, which expressed as a fraction of particles that could be added if defective particle neighborhoods were transformed to ordered crystalline ones. Row (b) the fraction of six-fold Voronoi cells over the course of annealing. Column (i) reports simulation data; Column (ii) reports experimental data. The MD simulation data were collected by B. J. VanSaders

2.5.4 Local ordering in MD simulation

Time evolution of ψ_6 data for a simulated system showing twenty cycles of cyclic field annealing with nine different durations of t_{off}. For long t_{off}, little or no improvement in ψ_6 is seen over twenty cycles. As the t_{off} is decreased, the maximum improvement of ψ_6 is found for $t_{off} = 0.5\tau_{50}$. As the t_{off} is further decreased, the linear growth rate decreases and the ψ_6 improvement from zero to twenty cycles also decreases.

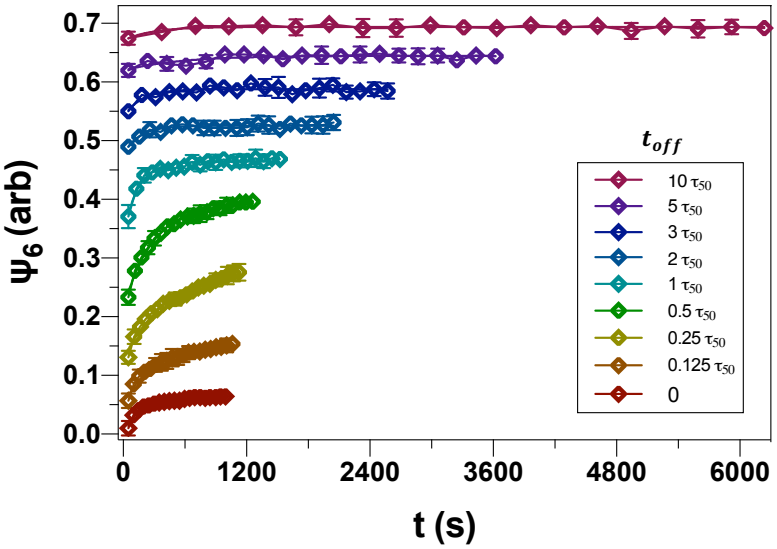

Figure 2.9 Local ordering over the full range of long-cycle times in MD simulation. Time evolution of ψ_6 data showing twenty cycles of cyclic field annealing. Curves are offset for comparison. These MD simulation data were collected by B. J. VanSaders

2.5.5 MD model parameter variations

Table 2.1 Model parameters for studying their impact on annealing performance in the simulated systems. Additional MD simulation models by variation of potential parameters controlling the electric field strength, interparticle attraction, and electrophoretic strength. The model used in the body of the text is model O. Half lifetimes here are reported in simulation units. The screening length for particle interactions is two particle diameters in all cases. These MD simulation data were collected by B. J. VanSaders

Model	Electric field strength [x1/kT]	Attractive interparticle interactions [x1/kT]	Electrophoretic potential strength [x1/kT]	Crystallization half lifetime ($\tau_{crystal}$) [s]	Melting half lifetime (τ_{50}) [s]
O	100	2	8	12.8 +/- 1.2	31.9 +/- 3.1
A	150	1	8	10.3 +/- 1.3	27.6 +/- 3.6
B	200	1	8	9.0 +/- 1.7	24.5 +/- 1.8
C	150	1	16	10.5 +/- 1.25	27.8 +/- 2.7
D	200	1	16	10.4 +/- 2.25	24.5 +/- 2.4
E	150	2	8	11.4 +/- 1.7	28.5 +/- 3.6
F	200	2	8	8.6 +/- 1.1	23.7 +/- 2.6
G	150	2	16	10.5 +/- 1.0	29.5 +/- 2.5
H	200	2	16	10.2 +/- 1.9	24.8 +/- 3.1

2.5.6 *Annealing performance with MD model variations*

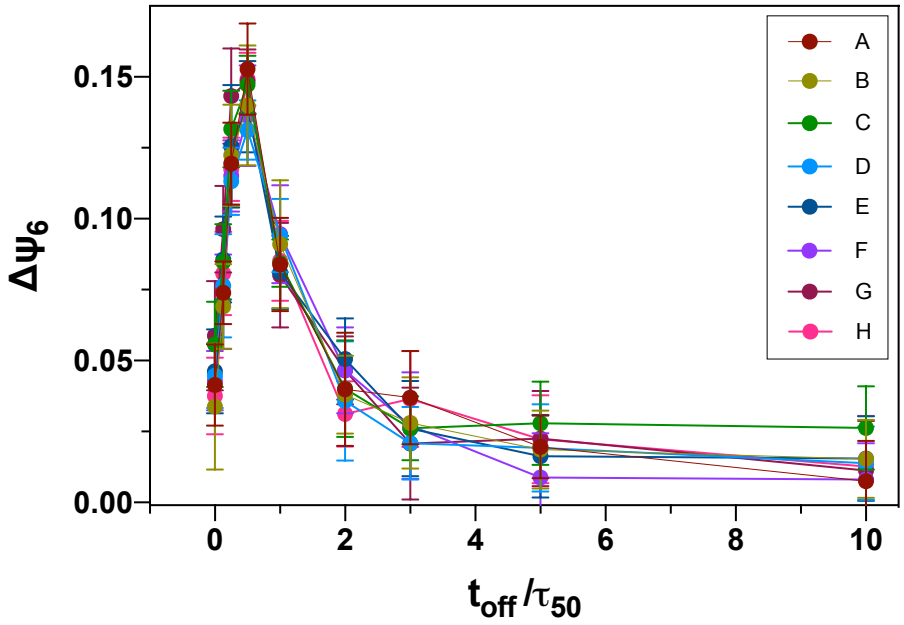

Figure 2.10 The impact of MD parameters on annealing performance in the simulated systems. Simulated $\Delta\psi_6$ changes over 20 cycles for MD models with a range of parameter values. The model parameters include electric field strength, interparticle attraction, and electrophoretic strength. Model parameter choice has some effect on peak shape, but for all models considered optimal annealing was found at $t_{off}/\tau_{50} = 0.5$. These MD simulation data were collected by B. J. VanSaders

2.5.7 *Local and global ordering in MD simulation*

Unlike in the experimental measurements, only negligible differences are present in the growth rate of SALS and ψ_6 curves in MD simulation. We attribute this difference to the comparatively smaller size of the simulated system, which is 250 μm x 500 μm as compared to 250 μm x 5000 μm for the experimental system. With fewer particles, the local and global re-arrangements are strongly coupled and have minimal differences in their rate of change.

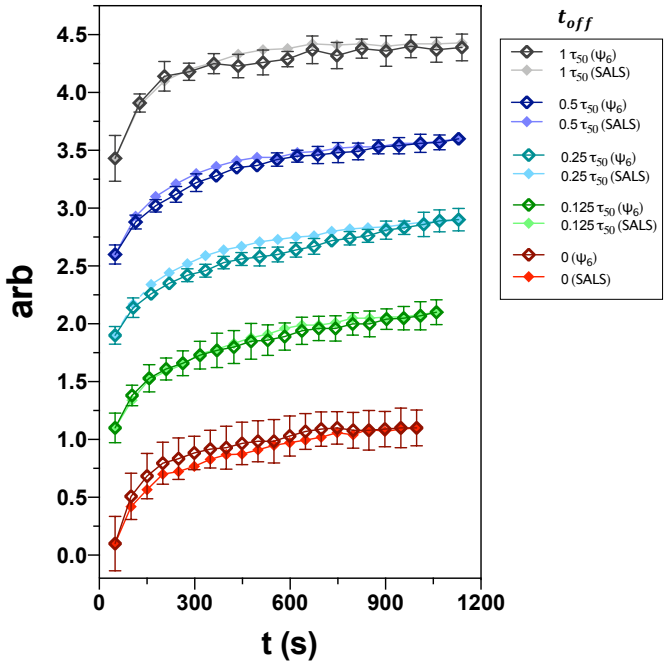

Figure 2.11 Comparison of local and global ordering in the simulated systems. Time evolution of ψ_6 data and SALS data for computer simulation system showing cyclic field annealing with five different durations of off-time. Curves are offset for comparison. These MD simulation data were collected by B. J. VanSaders

2.5.8 AC electric field device

The AC electric field device was prepared by first depositing 2.5 nm of titanium followed by 25 nm of gold onto a glass substrate. The gap between the two Ti/Au electrodes is 250 μm wide. The colloidal suspension was injected into the spacer, which is 1 mm in height. The inner diameter of the spacer is 5 mm.

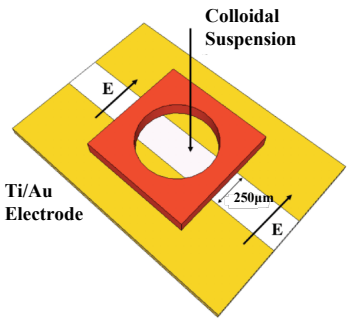

Figure 2.12 Illustration of the coplanar AC electric field device.

Chapter 3 Anisotropy Effects on The Kinetics of Colloidal Crystallization and Melting: Comparison of Spheres and Ellipsoids[4]

3.1 Abstract

We use alternating current (AC) electric field assisted self-assembly to produce two-dimensional, millimeter scale arrays of ellipsoidal colloids and study the kinetics of their phase reconfiguration by means of confocal microscopy, light scattering, and computer simulation[5]. We find that the kinetics of orientational and positional ordering can be manipulated by changing the shape of the colloids: ellipsoids with aspect ratio 2.0 melt into disordered structures 5.7 times faster compared to spheres. On the other hand, ellipsoids self-assemble into ordered crystals at a similar rate to spheres. Confocal microscopy is used to directly visualize defects in the self-assembled structures. Small-angle light scattering (SALS) quantifies the light diffraction response, which is sensitive to the kinetics of positional and orientational ordering in the self-assembled anisotropic structures. We find three different light diffraction patterns: a phase with high orientational order (with chain-like structure in real space), a phase with high positional and orientational order (characteristic of a close-packed structure), and a phase that is disordered in position but with intermediate orientational order. The large influence of aspect ratio on the kinetics of the positionally and orientationally ordered phase is explored through simulation; it is found that the number of particle degrees of freedom controls the difference between the melting

---

[4] The text in this chapter was originally in P. Kao, B. J. VanSaders, M. D. Durkin, S. C. Glotzer, and M. J. Solomon, *Soft Matter* (2019), **15**, 7479-7489. DOI: 10.1039/c9sm00887j

[5] Molecular dynamic simulations results reported in this chapter were acquired as part of collaboration with Dr. Bryan J. VanSaders.

rates of the ellipsoids and spheres. This research contributes to the understanding of reconfiguration kinetics and optical properties of colloidal crystals produced from anisotropic colloids.

3.2 Introduction

Self-assembled colloids can reconfigure their equilibrium phase or lattice parameter through dynamic manipulation of physical parameters such as the colloid size, shape, and interaction potential as well as the magnitude and direction of externally applied fields[3]. Photo-induced[5], electrophoretic, electrokinetic[84–89], and acoustic assembly[90] have been used to drive reconfigurable colloidal assembly. Applications of such kinetic information include the development of reconfigurable structural color[18] as well as soft robotics[41] and sensing[91]. In addition, some animals – including chameleons[16] and cephalopods[92] – are able to rapidly switch their coloration through reconfiguration of iridophores, which are structures that use diffraction to produce biological coloration[13,92,93]. In artificial systems, self-assembled colloids that can reconfigure their phase or lattice parameter offer similar possibilities for active coloration. Control of temperature[94], osmotic pressure[95] and the strength of electric fields[96] have been demonstrated to shift the wavelength of Bragg iridescence; however, more information about the kinetics of phase changes in such driven systems is needed.

Applications in which optical response is controlled by reconfiguration of ordered colloidal structures can be facilitated by better understanding what factors control the kinetics of crystallization and melting, which are the physical processes that control reconfiguration. Here we perform a comparative study of such in suspensions of colloidal spheres and ellipsoids. The kinetics of crystallization and melting has received significant attention in colloid science[97–99]. In this article, we extend the study of colloidal phase transitions to compare such transitions in

systems spheres and ellipsoids, as driven by the application of an electric field. The comparison of isotropic and anisotropic shapes[20,82] illuminates the fundamental effect of building block anisotropy on the kinetics of field-induced phase change, as observed by light diffraction. Comparing the simple geometries of spheres and ellipsoids is an ideal way to study the role of anisotropy in determining local and global order.

Confocal laser scanning microscopy (CLSM) is used to visualize the particle-level microstructure, including crystal arrays with vacancies, dislocations, and grain boundaries. We characterize the local microstructure of three different kinds of colloidal assemblies (chains, close-packed structures, and dense positionally disordered structures) using CLSM. Positional and orientational order parameters are used to describe the shortrange defect types and density observed by CLSM. Small-angle light scattering (SALS)[100,101] is used to characterize global, ensemble-averaged colloidal crystal quality through measurement of the integrated intensity of light diffraction peaks. This measure includes information about the intensity and azimuthal angular broadening of diffraction peaks; it can thus be used as a measure of the quality of global order. We use these measures to investigate the kinetics of crystal quality development by executing a reconfigurable fluid-crystal transition with AC electric fields. A molecular dynamics simulation model is developed to explore how polarization-induced forces, as generated by AC electric fields, drive assembly, and how particle geometry affects the kinetics of crystal assembly and melting. Using a coarse-grained representation of polarization-induced forces and excluded volume interactions only, the simulations demonstrate a large difference in melting kinetics between isotropic and anisotropic particles. From simulations, we find that this difference is linked to rotational dynamics. This result highlights the fundamental effect of building block anisotropy on melting kinetics.

3.3 Methods and Materials

3.3.1 Monodisperse colloidal ellipsoids

The ellipsoidal particles were produced by uniaxial stretching of polystyrene spheres with diameter 4.00 ± 0.04 μm (F8858, Invitrogen), as described in Shah et al.[23]. The ellipsoids used in this study have an aspect ratio of 2.0 ± 0.3 (major axis L = 6.4 ± 0.5 μm, minor axis D = 3.2 ± 0.2 μm, as determined by measuring 68 ellipsoids using scanning electron microscopy). After stretching, the ellipsoids were dispersed in 0.1 mM NaCl aqueous solution for self-assembly experiments. Initial colloidal volume fractions of 0.0015, 0.003, and 0.006 were studied. Concentrations were determined by using a hemocytometer (NanoEnTek Inc.). The initial number of colloids per unit surface area of the above systems are 0.044, 0.087 and 0.175 ellipsoids μm^{-2}, respectively[102].

3.3.2 Self-assembly by AC electric fields

To generate 2D monolayers of colloids by self-assembly, a coplanar AC electric field device was used. Briefly, the device was prepared by deposition of Au/Ti electrodes onto a glass substrate, as described in Shah et al.[41]. The device was cleaned before each use by means of a freshly prepared base bath (1 N potassium hydroxide solution in ethanol, Fisher Scientific). The colloidal suspension was injected into the device, which is 1mm in height. It took about one hour for particles to complete the sedimentation process. Particle sedimentation was completed before applying the AC electric field. A square wave with constant root-mean-square voltage (V_{rms}) ranging from 0.5 to 10.0 V and frequencies ranging from 500 Hz to 5 MHz was applied across the 250 μm gap between electrodes by means of an AC power source (RIGOL, DG1022). Particles are more concentrated at the centerline between two electrodes due to dielectrophoresis. The subsequently reported area fraction of particles is computed for the same region in which the

relaxation kinetics is studied and characterized. The resulting self-assembled structures were visualized by CLSM (Nikon A1 Piezo z-drive, 100×, NA = 1.45 oil immersion objective). The image size is 512 × 512 square pixels. The pixel size is 250 × 250 nm^2. For kinetics measurements, the frame acquisition rate was 15 frames per second.

3.3.3 Nearest neighbors and nearest neighbor angles

We used the number of nearest neighbors and the angles between those neighbors as local order parameters to quantify short-range positional order. The nearest neighbors of each ellipsoidal particle are identified in the assembled structure by comparing the distance between it and other particles to a chosen cutoff distance set by the radius of an elliptical coordination shell. The major axis of this shell is set as 2.1 times the second peak of g(r) of the close-packed colloidal ellipsoid structure. This cutoff is set to ensure that we include the first coordination shell in the counting. Figure 3.7(a)–(c) illustrates the process to find the nearest neighbors of a close-packed assembly of ellipsoids. The nearest neighbor angle, θnn, is also used to determine the quality of local positional ordering of an assembly. As shown in Figure 3.7(a), vectors connecting the centroid of a given particle to the centroids of its nearest neighbors are used to compute a set of nearest neighbor angles.

To quantify the orientational order of each assembled structure, we calculated the 2D alignment factor, $S = \frac{1}{2}\langle 3\langle u_i \cdot u_{ref}\rangle^2 - 1\rangle$ [103,104]. The alignment factor has been utilized to quantify the degree of particle orientation in liquid crystalline polymers[105] and ellipsoidal colloidal suspensions[24]. For S = 1, particles are perfectly oriented; S = 0 represents randomly distributed particle orientations.

3.3.4 Small-Angle Light Scattering

The design of the SALS device was adapted from Somwangthanaroj et al[106]. (See Figure 3.8). A laser (JDS Uniphase, 1135P) of wavelength 632.8 nm with a 1/e2 diameter of 0.71 mm was used. A neutral density filter of optical density 2.0 was used to attenuate the laser light. Two 45-degree mirrors were used to control the path of the light so that the colloidal sample could be placed in the horizontal position. After the laser light was scattered as it traversed the sample, an aspheric lens (diameter = 50 mm, focal length = 37 mm; Newport Inc., Irvine, CA) was used to collimate the scattered light. A pair of achromatic lenses (first achromatic lens, diameter = 50.8 mm, focal length = 250 mm; second achromatic lens, diameter = 12.7 mm, focal length = 40 mm) was utilized to collect the scattered light onto a 12-bit CCD camera. To enhance sensitivity, a beam stop (neutral density filter of optical density 5.0) was placed between the collimating lenses to block the central (unscattered) laser light. From this collected data, the intensities at each scattered angle can be derived. The range of accessible scattering angles is from 2° to 13°.

3.3.5 Analysis of light diffraction response

SALS is well suited to studying the collective dynamics of colloid assemblies, as it integrates over large areas. The pattern of light scattering recorded for fluid-like and crystal-like colloidal assemblies was primarily contained within a spherical or elliptical ring (for spheres and ellipsoids, respectively). We analyzed this ring to detect the disorder-to-order transition. The major axis of the ring was aligned in the field direction. The radial width of the analyzed region was set to a fixed value of 31 pixels because the average width of the primary scattering patterns was 31±2 pixels (c.f. 3.7.3). The average intensity is computed as a function of an azimuthal angle ψ; this angle is defined relative to the field direction. The analyzed region corresponds to a scattering vector $q = 1.69\ \mu m^{-1}$ in the direction of the field and $q = 1.11\ \mu m^{-1}$ in the perpendicular

direction, with a radial width $\Delta q \sim 0.32\ \mu m^{-1}$. Here, the scattering wavevector, $q = \frac{4\pi n}{\lambda} \sin\left(\frac{\theta}{2}\right)$, is equal to the difference between the incident wavevector and the scattered wavevector, where n is the effective refractive index of the sample, λ is the wavelength of incident light and θ is the scattering angle.

We use locally weighted smoothing (LOWESS[107]) to fit the intensity data as a function of azimuthal angle to a Gaussian model after baseline correction. Finally, we computed peak intensity, full width at half maximum (FWHM) and peak area of each scattering peak to quantify the light diffraction response. Greater peak intensity or smaller FWHM both represent higher long-range ordering quality of the self-assembly. Peak area incorporates information about both peak intensity and FWHM of the light diffraction response We find that peak area is sensitive to crystallization or melting, while being relatively insensitive to changes that occur after (or before) the system has transitioned. For this reason, we use peak area to quantify the light diffraction response in what follows, although we confirmed that our conclusions were not impacted by the specific choice among these three measures. A comparison of peak area, peak intensity and FWHM of light diffraction peaks as a measure of the colloidal phase change for simulated systems is included in the 3.7.3 (Figure 3.11).

3.3.6 Molecular Dynamics Simulations

Simulations of colloid assembly and melting were carried out with HOOMD-Blue[77,83], using Langevin dynamics simulations. The simulated model approximates experimental forces present on colloidal particles via four components: (1) A pair potential interaction with a steep repulsive core (representing excluded volume) and a weak attractive well (representing mild attraction between neighbors) in spherical or ellipsoidal coordinates; (2) Electrostatic forces between particles representing the effect of induced dipoles; (3) A torque aligning the particles

with the field direction; (4) A gravitational force to induce settling. For details concerning the implementation of these forces, see the 3.7.1.

The parameters of this particle interaction model were tuned to produce the experimentally observed crystal structures for spheres and ellipsoids of aspect ratio 2. This fitting was most sensitive to the parameters governing the electrostatic interactions of the particles. For ellipsoidal particles, different induced dipole moments can produce the crystal structure experimentally observed for spheres or that observed for ellipsoids. For spheres, the preferred motif of charge-mediated interactions is to form chains. Inter-chain attraction due to charge forces alone was too weak to result in long range 2D crystals. A weak direction independent attraction (the attractive part of the pair potential) was required for long-range spherical crystallization. Changes to the angular freedom of particles under 'field-on' conditions were not found to have strong consequences for the phase behavior of the model, but instead introduced additional spread into the peaks present in the Fourier domain representation of the crystals. The downward force representing gravity was chosen to match the force experienced by a polystyrene sphere of diameter 4.0 μm immersed in water. We found that the magnitude of this force needed to be sufficiently large to prevent the formation of 3D cluster assemblies but was otherwise unimportant to phase behavior. For the force we used, lifting a particle by its own diameter required $13k_bT$.

The initial simulation domain size was chosen so that the global particle area coverage was 0.5. During simulation, particles aggregate and form dense regions. For spheres, local area coverage (calculated in circular regions 20 times the size of a single particle) after assembly was 0.82±0.11. For ellipsoids, local area coverage (calculated for the same area as spheres) was 0.84±0.13.

3.4 Results

3.4.1 Light diffraction responses of ellipsoidal colloid assemblies

Depending on the initial concentration as well as the strength and frequency of the electric field, structures with a broad range of orientational and positional order were self-assembled. Figure 3.1 reports representative CLSM and SALS results at each concentration level (initial volume fraction (ϕ_i) 0.0015, 0.003 and 0.006) at an AC electric field strength and frequency of E = 40 kV/m and 5MHz, respectively. For an initial volume fraction of 0.0015, a phase with high orientational order and numerous positional defects was observed by CLSM (Figure 3.1 a-I). These positional defects were predominantly vacancies that were formed during sedimentation of the dilute colloidal suspension. This chain-like structure is similar to the structure Singh et al.[108] reported. Macroscopically, from SALS, a bright diffraction ring pattern was observed (see Figure 3.1 d-I).

When we doubled the initial volume fraction to 0.003, a phase with both high positional and orientational ordering was observed by CLSM (Figure 3.1 a-II). A monolayer of close-packed ellipsoids aligned with the AC electric field direction formed after sedimentation. Under the applied electric field, ellipsoidal colloids aligned their long axes with the field and tended to form zig-zag chain configurations with contacts offset from the tip. A clear six-fold diffraction pattern appeared in the SALS (Figure 3.1 d-II). The SALS diffraction patterns are anisotropic because of the geometry of the unit cell, which is impacted by the ellipsoidal shape of the colloids.

Upon further increase of the initial volume fraction to 0.006, application of the AC electric field yielded a positionally disordered structure, as shown in Figure 3.1 a-III. This disordered structure is composed of multiple layers of ellipsoids assembled on top of the

coplanar electrode. The intensity of the corresponding diffraction response was low (see Figure 3.1 d-III).

We calculated the area fraction covered by particles as $d_{2D} = N \times S_a/A$ where N is the total number of particles in an image from image analysis, S_a is the area of a single ellipsoid, and A is the image area. The area fraction is 60.3% for the chain-like structure, 82.1% for the close-packed structure and 66.2% for the dense positionally disordered structure. The area fraction for the dense positionally disordered structure is for the bottom layer of the structure.

A non-monotonic relationship between the initial volume fraction and the density of the assembled layers is observed. This non-monotonicity is due to arrested crystallization kinetics at the highest initial densities studied. At lower area concentration, the low number of particles per area on the substrate leads to the low-density chain-like structure. At intermediate area concentrations, the density is sufficient to permit the formation of a dense crystalline structure. At high concentrations, dynamics are slow enough to yield kinetic trapping, particularly because of the anisotropic shape of the particles and the presence of multiple layers. This sequence of transitions has been predicted theoretically[109] and observed experimentally[23,110] in three dimensions.

For ellipsoids of initial volume fraction of 0.0015, 0.003 and 0.006, the alignment factor (S) values are 0.88 ± 0.02, 0.93 ± 0.01, and 0.58 ± 0.02 respectively. For the dense positionally disordered phase (ϕ_i = 0.006, d_{2D} = 66.2%), S is relatively low and thus is distinguishable from the other two cases. To further distinguish the chain-like structure and the close-packed structure, we turn to analysis based on the position and orientation of nearest neighbors (c.f. Methods). For the chain-like structure (ϕ_i = 0.0015, d_{2D} = 60.3%, S = 0.88), as shown in Figure 3.1 b-I, the average number of nearest neighbors is 3.5 with standard deviation of 1.1. There are 23±4 % of nearest

neighbor angles (θ_{nn}) ranging from 140° to 180° observed in the distribution of nearest neighbor angles (Figure 3.1 c-I), indicating chaining of ellipsoids due to the polarization attraction between particles and the appearance of vacancies in the assembly.

As shown in Figure 3.1 b-II, for the close-packed structure (ϕ_i = 0.003, d_{2D} = 82.1%, S=0.93), the average nearest neighbors are 5.5 with a standard deviation of 1.3. There are 53±8 % of particles that have six nearest neighbors and 85±4 % of particles that have a number of nearest neighbors between five to seven, indicating this is a hexagonally close-packed structure, which is consistent with the six-fold symmetry we observed in Figure 3.1 a-II. The real space and light scattering data are connected by Fourier transform. From the nearest neighbor angle distribution analysis (see Figure 3.1 c-II), we observed two distinct peaks at 41.3±1.3° and 69.4±1.6°. These two peaks are very close to the Fourier transform results of a simulated hexagonally close-packed particles array, with the same particle aspect ratio as in our experiments. The corresponding modeling results are 41.3±0.1° and 69.4±0.1°. The chaining angle between ellipsoids which are half of θ_{nn} is therefore about 20.7°. Singh et al. reported an average chaining angle between 10° and 15° for ellipsoids with three different aspect ratios (3.0, 4.3, and 7.6) assembled in an AC electric field. Azari et al. reported the contact angle between two adjacent ellipsoids at their minimum energy configuration as a function of particles aspect ratio. Using the two-point charge model, a contact angle of 12° between ellipsoids with aspect ratio two was reported.

Lastly, for the dense positionally disordered structure, the average nearest neighbors are 3.9 with a relatively large standard deviation of 2.2 (Figure 3.1b-III). No obvious patterns are found for the distribution of nearest neighboring angles (Figure 3.1c-III). Thus, we successfully resolve and differentiate between three different structures: hexagonal chain-like structure, close-

packed structure and dense positionally disordered structure by introducing the comparison of alignment factor, nearest neighbors and nearest neighboring angles.

We determined the quality of the self-assembled colloidal crystals from analysis of light scattering images (Figure 3.1d I-III) by computing the peak area as a function of the azimuthal angle, ψ (cf. Methods and Materials). We assigned the peak at ψ = 20.7°, 90.0°,159.4°, 200.7°, 270.0°, and 339.4° as peak 1, 2, 3, 4, 5, and 6 respectively (Figure 3.1d-II). Peaks 2 and 5 are generally much brighter than peaks 1,3,4 and 6 (Figure 3.1 e I-III). This phenomenon is a consequence of the ellipsoidal shape of the particles; that is, the shape of the scatterer generates the angular variation in the scattering[111].

For the chain structure, the average peak area of peaks 1,3,4, and 6 is 480±24 arbitrary unit (au) (46% of light scattering peak area compared to that of the close-packed structure), and for peaks 2 and 5 is 985±50 au (21% of light scattering peak area compared to that of the close-packed structure). For the close-packed structure, there are six significant scattering peaks. The average peak area of peaks 1,3,4, and 6 is 1,041±25 au, and the average peak area of peaks 2 and 5 is 4,684±182 au. For the dense positionally disordered structure, the scattering peaks are minimally resolvable with the average peak area of peaks 1,3,4, and 6 equal to 85±14 au (only 8% light scattering peak area compared to that of the close-packed structure), and the peak area of peaks 2 and 5 is 524±38 au (11% light scattering peak area compared to that of the close-packed structure). The Figure 3.1 results reveal the connection between the long-range optical properties and the short-range defect microstructures in the ellipsoidal suspensions. The close-packed structure that displays the least number of defects exhibits the most intense light scattering peak area.

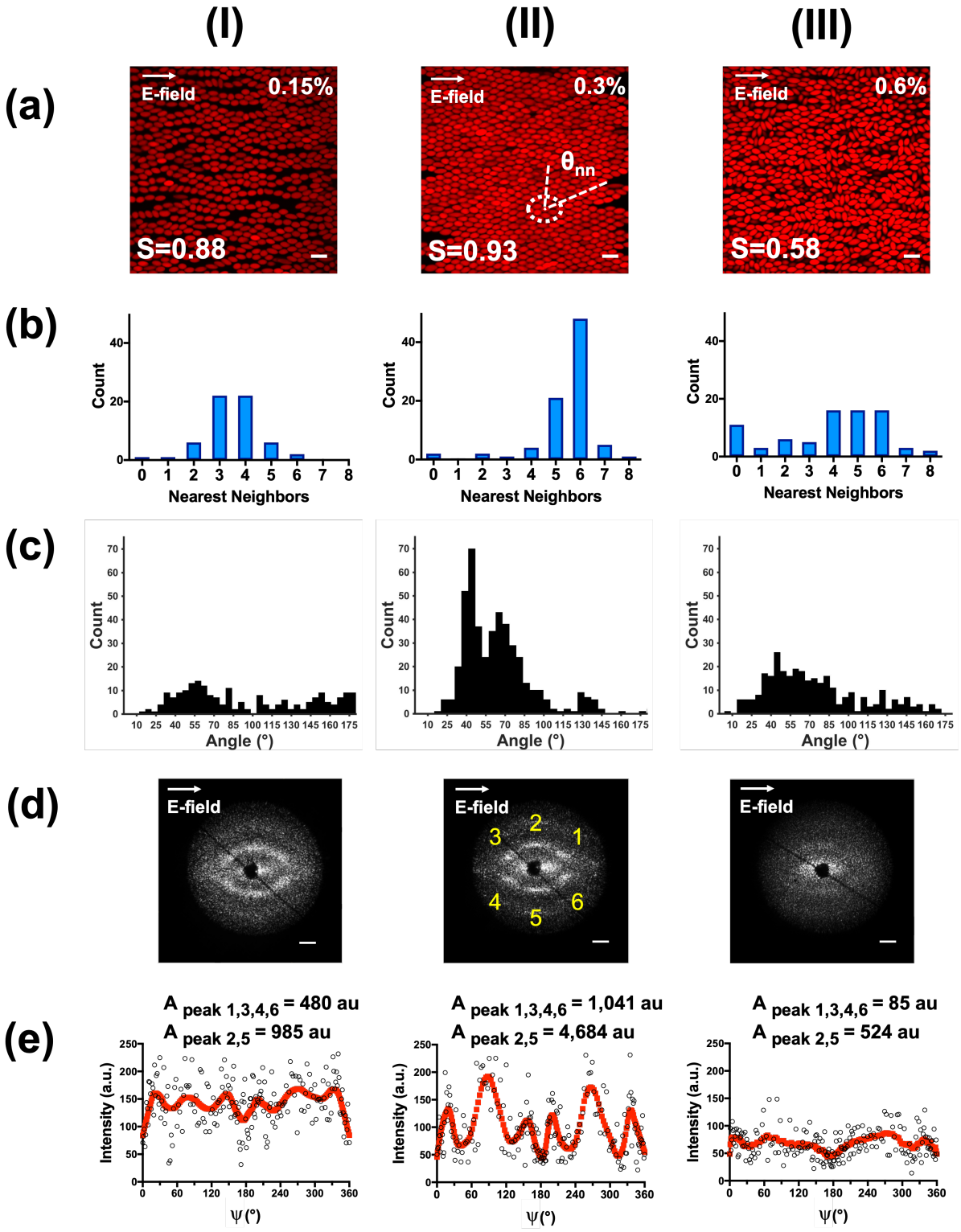

Figure 3.1 2D confocal laser scanning micrographs of (a-I) a high orientational order chain-like phase, (a-II) a high positional and orientational order close-packed phase, and (a-III) a dense positionally ordered phase. The counts of nearest neighbors of (b-I) chain-like phase, (b-II) close-packed phase, and (b-III)

dense positionally ordered phase. The distribution of nearest neighboring angles of (c-I) chain-like phase, (c-II) close-packed phase, and (c-III) dense positionally ordered phase. SALS images of (d-I) chain-like phase, (d-II) close-packed phase (with peak numbering), and (d-III) dense positionally ordered phase. The intensity of light scattering responses along the azimuthal angle ψ was acquired from SALS analysis for (e-I) chains-like phase, (e-II) close-packed phase, and (e-III) dense positionally disordered phase. The black circles are SALS data points and the red-square curves are the corresponding Gaussian fitted curves. Scale bars in CLSM images are 10 μm. Scale bars in SALS images are $q = 1\mu m^{-1}$.

3.4.2 Dependence of crystal quality on self-assembly conditions

To study the kinetics of colloidal crystal quality development, we first evaluate the impact of applied electric field strength and applied frequency Ω on ellipsoid self-assembly. We focus on the intermediate initial concentration condition going forward, because this specimen yielded a high-quality single-layer structure with positional and orientational order, as reported in Figure 3.1. Figure 3.2(a) reports images of colloidal self-assembly at electric field strength E= 8 kV/m, 18kV/m and 40kV/m, respectively, with applied frequency fixed at 5MHz, as well as the SALS images of the assembled structures. Prior to application of the electric field, particles are homogeneously dispersed at d2D = 82.1%. For electric field strengths smaller than 8 kV/m, the magnitudes of the light diffraction peak areas are at a minimum level. At E=8 kV/m, the assembled structure is disordered (Figure 3.2a-I), and diffraction peaks are minimally resolvable by analysis of light scattering images (Figure 3.2a-II). At AC E=18 kV/m, the ellipsoids assemble along the direction of the electric field and form structures with poor crystal quality and abundant local defects (Figure 3.2a-III). Peaks 2 and 5 become bright and visible, while peaks 1,3,4, and 6 remain close to background level (Figure 3.2a-IV). At E=40 kV/m, close-packed assemblies with a low concentration of defects are observed (Figure 3.2a-V). In addition to low defect density in the images, the corresponding SALS image show a bright six-fold diffraction pattern indicative of high global crystal quality (Figure 3.2a-VI).

Figure 3.2 (b) shows the peak area of the light diffraction response (A) under varying electric field strengths with constant applied frequency (5MHz). As the electric field strength was increased, the peak area tended to increase, indicating a field-induced disorder-to-order transition. Once the electric field strength exceeds the threshold value of 24 kV/m, the magnitude of the peak area increased only slowly with field strength. The results demonstrate that good colloidal crystal quality can be achieved as the electric field strength exceeds the threshold value of 24 kV/m.

It is noteworthy that a scattering response at low q is apparent in Figure 3.2a-IV and a-VI. This response occurs for $q \leq 0.46$ μm-1. Based on the reciprocity of Fourier transforms, whereby a functional width σ in real-space maps to a spread of $q = 2\pi/\sigma$ in the corresponding diffraction-space, this low q diffraction response is generated from structures of functional width $\sigma \geq 13.7$ μm. This peak is consistent with the device geometry. That is, within the coplanar electric field device which has a gap dimensions of 250 μm, colloidal particles form a dense phase in the center; gradients in particle density are observed along the electric field direction. This real-space phenomenon is consistent with the low-q scattering response.

The frequency of the electric field also influences crystal quality through its effect on the field-induced polarization of the colloids. We measured the crystal quality at various frequencies with a fixed electric field strength of 32kV/m. At frequency $\Omega = 0.5$ kHz, ellipsoidal particles rapidly clustered between the electrodes (Figure 3.2c-I). The phenomenon is caused by dielectrophoresis, as observed in other studies[112]. A dim elliptic ring-shape scattering response was observed instead of a six-fold diffraction pattern (Figure 3.2c-II). At frequency 100 kHz, colloids assembled into structures with low positional order (Figure 3.2c-III), showing elliptical ring-shape scattering (Figure 3.2c-IV). Six-fold scattering patterns can be observed as the applied

frequency exceeds 0.5 MHz. At frequency 5 MHz, ellipsoidal particles generated colloidal crystals with high positional and orientational order (Figure 3.2c-V). The corresponding light scattering image shows a bright six-fold pattern (Figure 3.2c-VI)

Figure 3.2 (d) shows the peak area of the light diffraction response with field frequency varying from 0.5 kHz to 5 MHz under constant field strength 32 kV/m. For frequency Ω in the range of 0.5−10 kHz, the magnitudes of light diffraction peak areas are at a minimum level. For 10-100 kHz, the average magnitude of the light diffraction peak areas is 3.6±0.7 times brighter for peaks 2 and 5 and 3.8±0.8 times brighter for peaks 1,3,4 and 6 compared with frequency in the range of 0.5−10 kHz. For Ω in the range of 0.5−5 MHz, the average magnitude of peak areas is 13.4±2.4 times brighter for peaks 2 and 5 and 23.7±2.8 times brighter for peaks 1,3,4 and 6 compared with Ω in the range of 0.5−10 kHz.

The interparticle distance (σ_i) can be calculated from the SALS data based on the reciprocity relationship $q=2\pi/\sigma_i$ between diffraction-space and real-space. From Figure 3.2(a), the major axis and the minor axis of the SALS pattern are 1.29 μm^{-1} (σ_i = 4.87 μm) and 0.86 μm^{-1} (σ_i = 7.31 μm) at electric field strength 18kV/m. Upon increase of the electric field strength to 40kV/m, the major axis and the minor axis of the SALS pattern are 1.30 μm^{-1} (σ_i = 4.83 μm) and 0.87 μm^{-1} (σ_i = 7.22 μm), respectively. The above results show that interparticle distance decreases with increasing applied field strength. From Figure 3.2(c), the major axis and the minor axis of the SALS pattern are 1.23 μm^{-1} (σ_i = 5.11 μm) and 0.81μm^{-1} (σ_i = 7.76 μm) for applied frequency 100kHz. With frequency increased to 5MHz, the major axis and the minor axis of the SALS pattern are 1.27 μm^{-1} (σ_i = 4.95 μm) and 0.87 μm^{-1} (σ_i = 7.22 μm). The results also demonstrate that interparticle distance decreases with increasing frequency. These average

interparticle distances change only modestly for electric field strength 18-40kV/m and frequency 100kHz-5MHz. However, at the same time the diffraction patterns evolve from a ring (disordered phase) to a six-fold pattern (crystallization). This indicates that while interparticle distances are largely conserved, the particles are aligned in specific directions with increasing electric field strength and frequency.

Based on the above results, we selected E = 32 kV/m and Ω = 5MHz, shown as red boxed data points in Figure 3.2(b) and (d), for further kinetic studies. These conditions ensure that the colloidal particles assemble into high quality crystals by means of AC electric fields.

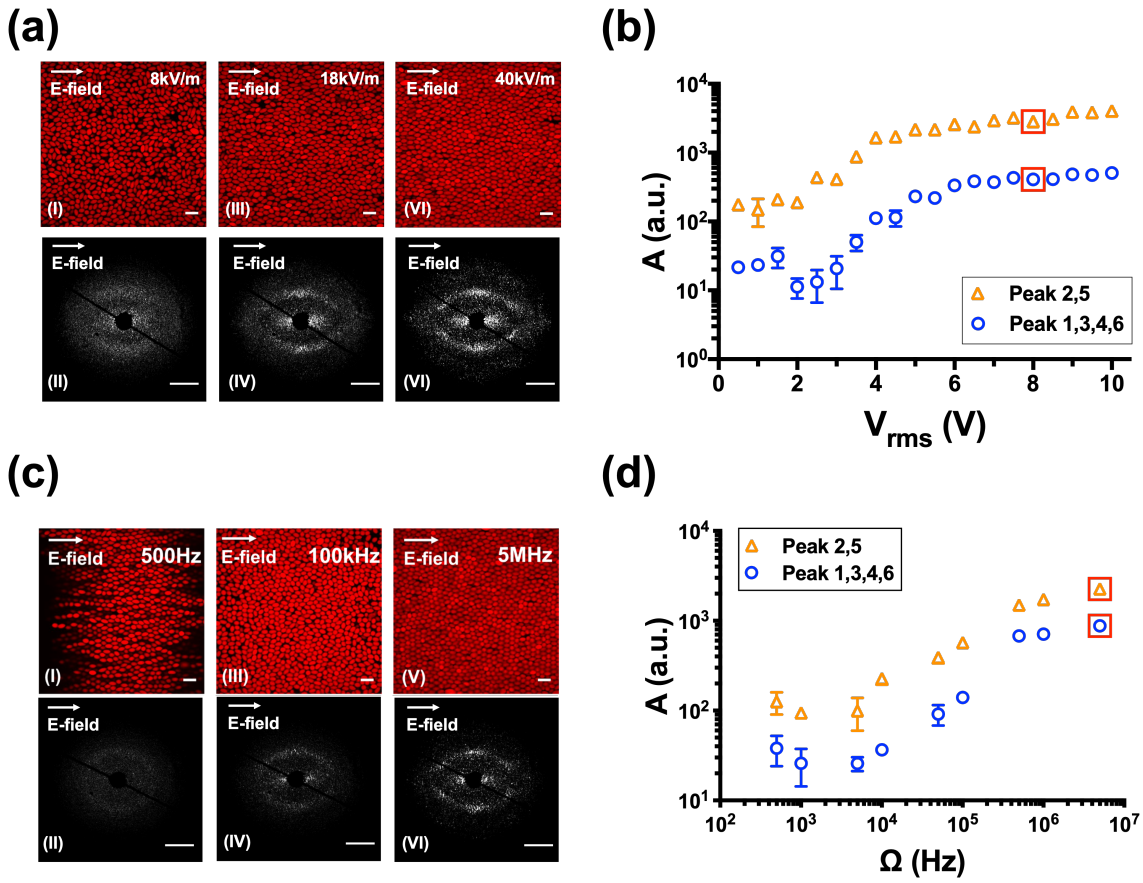

Figure 3.2 The impact of electric field-applied voltage and frequency on colloidal crystal quality, as quantified by peak area. (a) The CLSM and corresponding SALS images of ellipsoidal colloids assemblies under applied electric field strength at 8kV/m, 18kV/m and 40kV/m respectively. (b) The

change of peak area of light diffraction response (A) under different applied electric field strength. (c) Characteristic CLSM and corresponding SALS images of ellipsoidal colloids assembled under applied frequency at 500 Hz, 100 kHz and 5 MHz, respectively. (d) The change of peak area of light diffraction response (A) under different applied frequency Ω. Scale bars in CLSM images are 10 μm. Scale bars in SALS images are $q = 1\mu m^{-1}$. E = 32 kV/m and Ω = 5MHz, shown as red boxed data points in (b) and (d), are selected field strength and frequency for further kinetic studies to ensure that the colloids assemble into high quality crystals.

3.4.3 The effects of shape anisotropy on colloidal ordering kinetics

Figure 3.3 compares the time-evolution of the SALS peak area of the $d_{2D} = 82.1\%$ specimens for the ellipsoids under field-on (assembly) and field-off (melting) conditions. Comparative experiments with spheres were performed at the same conditions. The initial state for the field-on experiments were the disordered suspensions at the initial volume fraction. Particle sedimentation was allowed to complete before the field was switched on; the number of particles within the region probed by SALS does not vary significantly during the study. The melting experiments were conducted by first creating a close-packed crystal with the electric field on for five minutes and then turning off the field. This melting-assembly cycle was repeated five times with 10 minutes between each cycle. The SALS were analyzed as described to obtain the time dependence of the peak area.

Figure 3.3(a) shows that there is a monotonic decay of peak area upon melting of the solution of spheres. The six peaks have two sets of decays. It takes approximately 150 seconds for peaks 1,3,4 and 6 to reach the steady-state value and 180 seconds for peaks 2 and 5 to reach the steady-state value. Figure 3.3(b) reports the assembly of spheres and shows a monotonic increase of peak area. It takes approximately 70 seconds for all peaks to reach steady-state values.

Under the same experimental conditions, the melting of aspect ratio 2 ellipsoids showed a much faster transition from one peak area to another. As shown in Figure 3.3(c), it took

approximately 30 seconds for peaks 1,3,4, and 6 to reach the steady-state value and 40 seconds for peaks 2 and 5 to reach the steady-state value. The difference in the kinetics between the two sets of peaks may be related to the symmetry breaking of the field. Differences in ordering between the field direction and the other two close-packed directions lead to different melting kinetics. Figure 3.3(d) reports the assembly of the ellipsoids, showing a monotonic increase of peak area. Similar to the assembly of spheres, it takes the ellipsoids approximately 70 seconds to reach steady-state values of the peak area.

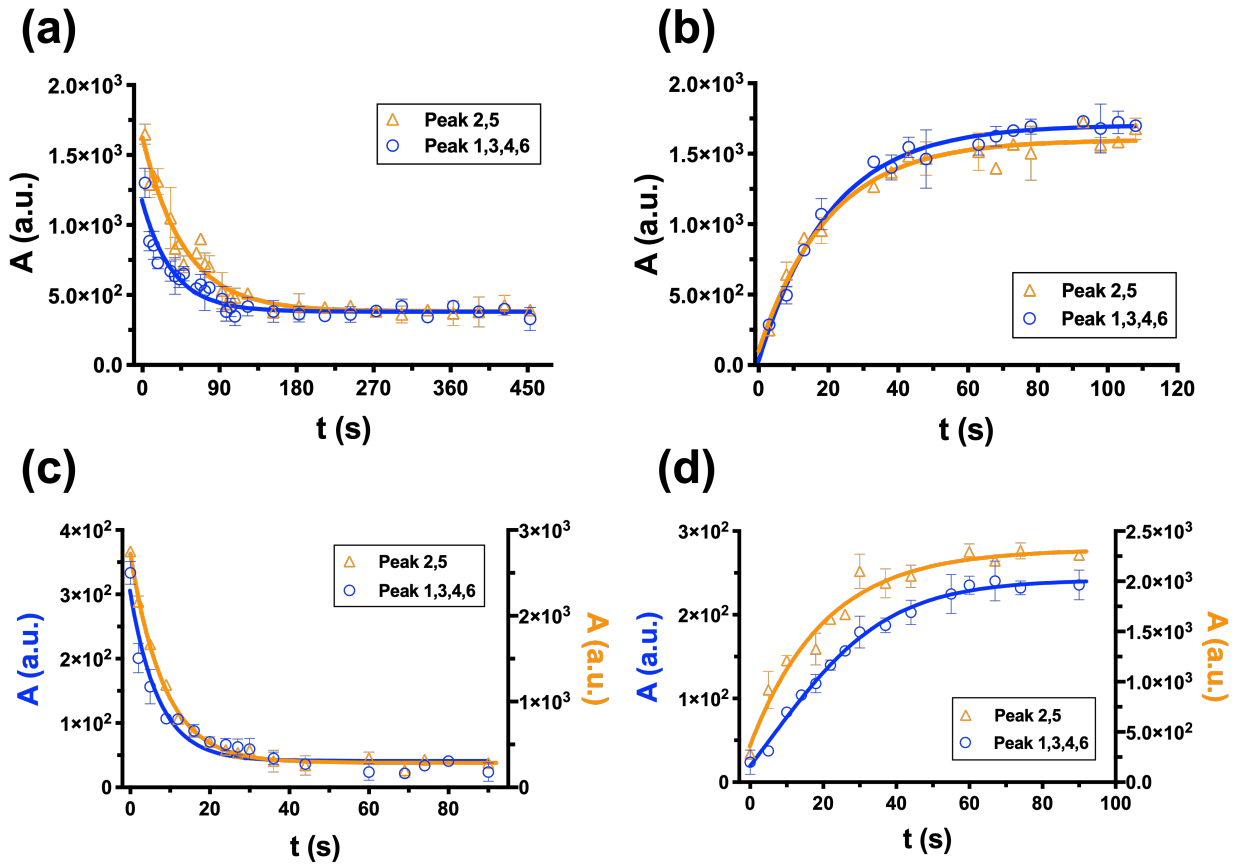

Figure 3.3 The change of peak area of light diffraction responses as a function of time t for (a) spherical colloid melting, (b) spherical colloid assembly, (c) ellipsoidal colloid melting, and (d) ellipsoidal colloid assembly.

Using a pair potential model appropriate to the conditions of the self-assembly (c.f. Figure 3.4(a) and methods), Figure 3.4 compares the self-assembled structure and diffraction patterns of the experimental and simulated systems. Figure 3.4 (b) and (d) show CLSM images of spheres and ellipsoids, respectively. These can be compared to Figure 3.4 (f) and (i) which show the simulated systems. Comparing the SALS diffraction patterns (Figure 3.4 (c) and (e)) and the 2D Fourier transform of the simulated systems (Figure 3.4 (g) and (j)) shows that the symmetry of crystal ordering is the same for experimental and simulated systems. The largest deviation occurs at small q-values, which correspond to large spatial scales. This deviation is expected, because the simulated systems are of limited size and particle number compared to the experiments.

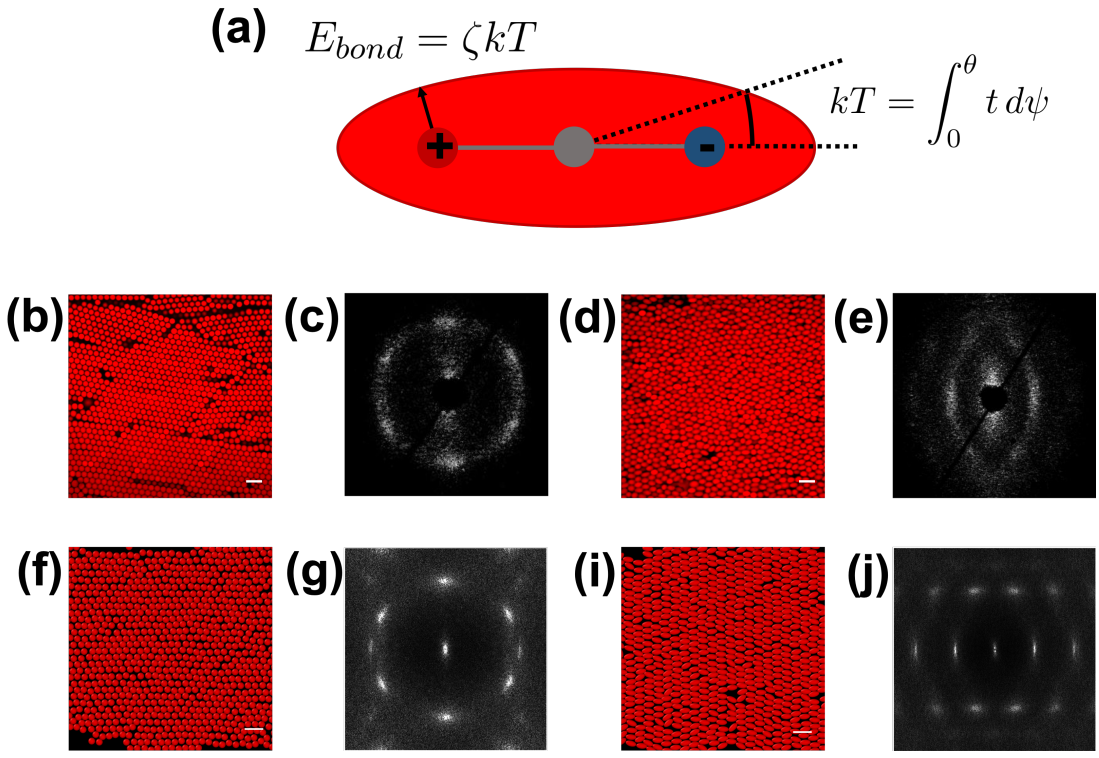

Figure 3.4 (a) Schematic of the interaction model used to simulate polarized particle interactions using rigid bodies and discrete charges. Experimental images of spheres (b) and ellipsoids (d) assembled into dense crystals. Matching SALS patterns for experimental sphere (c) and ellipsoid (e) systems. Images of simulated

spheres (f) and ellipsoids (i) assembled into dense crystals. Matching 2D Fourier transforms of simulated spheres (g) and ellipsoids (j). Scale bars in images are 10 μm. The MD simulation results were collected by B. VanSaders.

Another difference between the experimental and simulated systems is that the simulated ellipsoidal crystal appears to have higher quality. The higher degree of crystallinity of the model may arise from the differences in electrostatic fields surrounding an experimental particle as it rotates in a field and the interaction model based on discrete charge used here. Snapshots of simulated systems as they assemble show that a lower quality polycrystalline solid is formed first, and a slower annealing process follows (cf. Figure 3.10). This annealing might be arrested by other factors in the experimental case.

Detailed particle position data were collected for 20 simulated seconds after the field was switched on to observe the kinetics of assembly. After 11 simulated minutes of field-assisted assembly, the field was switched off and detailed system data were again collected to observe crystal melting. Figure 3.5 (a) and (b) show the growth curves of projected peak area for simulation of spheres and ellipsoids. Peak areas were computed by angle-binning the Fourier domain scattering pattern of the simulated system via the same method as for the experimental SALS data (c.f. Methods). Spheres form end-to-end chains aligned with the field direction. Ellipsoids instead form zig-zag chains aligned with the field direction[108]. Both findings agree with the experiments. Despite spherical particle symmetry, Figure 3.5(a) shows that peaks aligned with the field direction (peaks 2 and 5) have different kinetics relative to the other peaks. As discussed earlier, the symmetry of the peaks is broken by the anisotropic forces present due to the applied field.

Figure 3.5 (c) and (d) shows the same data as Figure 3.5(a) and (b), but now for melting, when the simulated field is switched off. Figure 3.5(c) shows that the melting kinetics of the peaks

for spheres collapses onto the same curve after the field is turned off, consistent with the peak differences being a consequence of the applied electrostatic forces. Figure 3.5(d) reveals that unlike assembly, melting kinetics is strongly affected by the anisotropy of the particles.

In order to capture the time scale of a transition from one peak area to another, the curves were fit with the logistic decay equation:

$$A(t) = \frac{B-C}{1+e^{-k(t-t_0)}} + C \qquad (3\text{-}1)$$

where A(t) is the peak area of light diffraction response, B is the initial peak area value, C is the long-time value of A(t), and k is the rate constant. The larger the value of k, the faster the self-assembled structures respond to the change of the field.

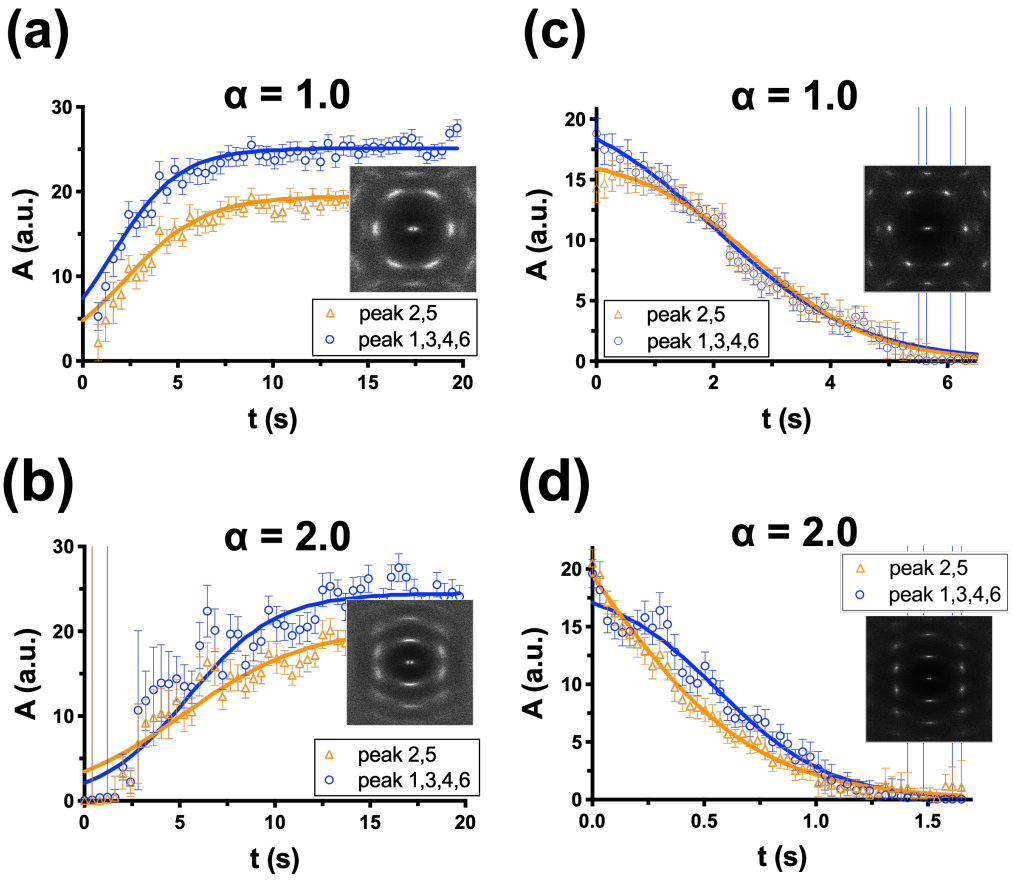

Figure 3.5 (a) and (b) show assembly kinetics. Projected peak area growth curves for simulated (a) spheres and (b) ellipsoids. Insets show the 2D Fourier transform of the assembled crystal structure. Error

bars represent uncertainty in the peak fitting procedure. (c) and (d) show melting kinetics. Projected peak area decay curves for simulated (c) spheres and (d) ellipsoids. Insets in (c) and (d) show the Fourier transform of the crystal structure before disassembly. These MD simulation results were collected by B. VanSaders

Table 3.1 reports the assembly time constant (k) of the logistic growth function (eqn. 3-1) for ellipsoids and spheres relative to the assembly rate constant measured from peaks 2 and 5 of spheres, as reported in Figure 3.5 (a), (b). The results show that ellipsoids and spheres assemble into a crystal with long-range ordering, as quantified by the diffraction peak area, with roughly equivalent kinetics to within the uncertainty of the fitting parameters. Our results show that shape anisotropy strongly affects the melting kinetics, but not the assembly kinetics. In the field-on condition, rotation of the ellipsoidal particles is restricted by polarization-induced effects. Therefore, the rotational degrees of freedom do not significantly influence the kinetics of concentrating ellipsoids into a dense structure; the difference in the assembly rate between spheres and ellipsoids is therefore small. The assembly kinetics for crystallization are thus controlled by the strength of electrostatic forces and the translational diffusion of particles, which are seemingly similar for spheres and ellipsoids.

Table 3.1 Experimental and simulated assembly rate constants for ellipsoids and spheres relative to the assembly rate constant measured from peaks 2 and 5 of spheres. Error in rate constants is found from uncertainty in fitting Eqn. 3-1 to experimental/simulated data. The MD simulation results were collected by B. VanSaders

	Assembly	**Experiments**	**Simulations**
Spheres	k/k_1 (peak 2,5)	1.00 ± 0.01	1.00 ± 0.19
	k/k_1 (peak 1,3,4,6)	0.98 ± 0.01	1.16 ± 0.25
Ellipsoids	k/k_1 (peak 2,5)	0.98 ± 0.17	0.63 ± 0.19
	k/k_1 (peak 1,3,4,6)	1.21 ± 0.38	0.89 ± 0.23

Table 3.2 reports the melting time constant (k) for ellipsoids and spheres relative to the melting rate constant measured from peaks 2 and 5 of spheres, as reported from Figure 3.5(c) and (d). For spherical particles, melting occurs somewhat slower (smaller time constant) than assembly. For ellipsoidal particles, melting is ~2.4 times faster (larger time constant) than assembly. In addition, Table 3.2 indicates that the ellipsoids melt at a rate that is ~5.7 times faster than spheres. This dichotomous effect of anisotropy on kinetics is a key finding of the study; colloidal shape affects melting kinetics to a much greater degree than assembly kinetics

Table 3.2 Experimental and simulated disassembly rate constants for ellipsoids and spheres relative to the disassembly rate constant measured from peaks 2 and 5 of spheres. The MD simulation results were collected by B. VanSaders

	Melting	**Experiments**	**Simulations**
Spheres	k/k_1 (peak 2,5)	1.00 ± 0.07	1.00 ± 0.12
	k/k_1 (peak 1,3,4,6)	1.36 ± 0.09	0.83 ± 0.08
Ellipsoids	k/k_1 (peak 2,5)	5.74 ± 0.17	2.94 ± 0.32
	k/k_1 (peak 1,3,4,6)	6.76 ± 0.56	4.09 ± 0.54

3.4.4 Effect of rotational degree of freedom on melting rate

To understand the origin of the kinetic differences for sphere and ellipsoid melting, we investigated the effects of rotational degrees of freedom. A simulation of the melting process without particle rotation for ellipsoids was carried out. The starting configuration for this simulation was the crystal assembled under full consideration of the rotational degrees of freedom, as reported, for example, in Figure 3.5. Beginning at the point when the simulated field is turned off, this new simulation was carried out with the ellipsoidal particles unable to rotate.

Particles in the previous simulations had 5 degrees of freedom (3 positional and 2 rotational). When rotation is not permitted only the 3 positional degrees of freedom remain.

Figure 3.6 shows the change in simulated SALS peak area with time of ellipsoidal particles for $N_{DOF=5}$ and $N_{DOF=3}$. When rotation is not allowed, the rate of peak area change is significantly reduced. Table 3.3 shows the value of the logistic fit parameter (k) for the simulations shown in Figure 3.6, as well as for spheres. Ellipsoids without rotational degrees of freedom are shown to melt at a very similar rate to simulated spheres. The comparison clearly indicates that the rotational degrees of freedom for these systems are responsible for the striking change in melting kinetics for spheres and ellipsoids.

During melting, the decreasing area of the light scattering peaks is a consequence of the reduced global crystal quality and the increased defect density. These defects, which lead to melting, are generated as ellipsoids undergo both translational and rotational Brownian diffusion. Of course, the rotational Brownian motion of spherical colloids does not affect their crystal ordering. That is, spherical colloids melt only by translational diffusion while both translational and rotational diffusion contribute to colloidal crystal melting of ellipsoids.

On the other hand, for assembly, the diffusion of the spheres and ellipsoids is the same as in melting; however, there exists an additional field-induced interaction that aligns and assembles particles into a dense crystal. As a result, the differences due to rotational Brownian diffusion during assembly are less dominant than for melting.

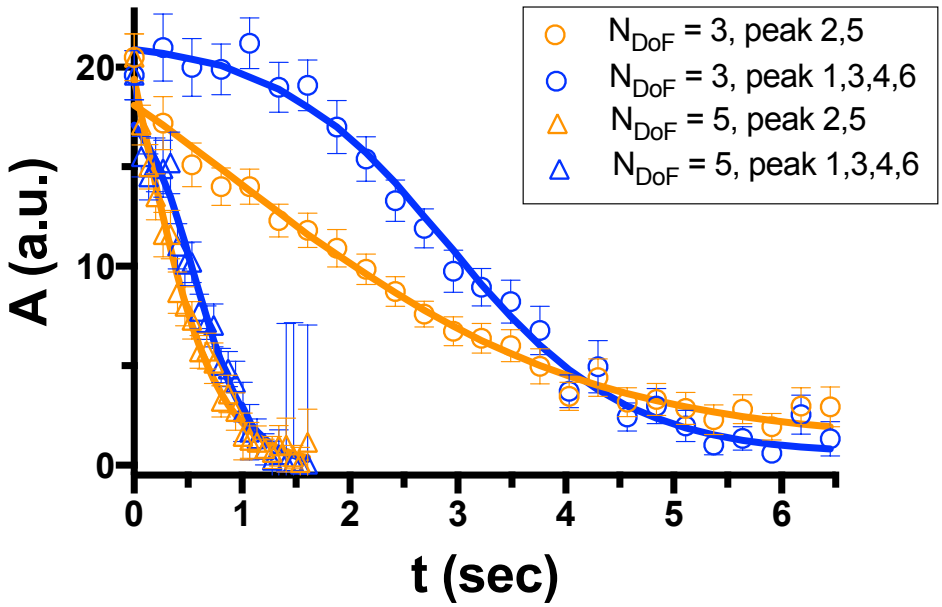

Figure 3.6 Change in area of the simulated SALS peaks as a function of time for a simulation of ellipsoids. Two cases are shown: melting under full translational and rotational diffusion (N_{DoF} = 5, circles) and when rotational degrees of freedom are not included (N_{DoF} = 3, triangles). Error bars are calculated from uncertainty in peak fitting, which is higher in the fluid phase. These MD simulation results were collected by B. VanSaders

Table 3.3 Simulated disassembly rate constants relative to the disassembly rate constant measured from peaks 2 and 5 of spheres at different aspect ratios with (N_{DoF} =5) or without (N_{DoF} =3) degrees of rotational freedom. The MD simulation results were collected by B. VanSaders

		Degrees of freedom = 3	**Degrees of freedom = 5**
Spheres	k/k_1 (peak 2,5)	1.00 ± 0.12	
	k/k_1 (peak 1,3,4,6)	0.83 ± 0.08	
Ellipsoids	k/k_1 (peak 2,5)	0.64 ± 0.09	2.94 ± 0.32
	k/k_1 (peak 1,3,4,6)	1.26 ± 0.10	4.09 ± 0.54

3.5 Discussion

3.5.1 The effects of applied electric field strength and frequency on crystal quality

From both SALS and CLSM data, we observed higher crystallinity of colloidal assemblies at electric field strengths greater than 24 kV/m. Singh et al.[108] investigated the applied electric field strengths ranging from 0 to 40 kV/m and frequencies varying between 1 and 10 kHz for 2D ellipsoids assembled by an AC electric field. As the field strength increases over 10kV/m, the induced polarization of the particles led to interparticle chaining in the field direction. Azari et al.[113] likewise reported a transition from fluid to either a crystal or tubular structure for electric field strengths greater than 75 kV/m, depending on the particle aspect ratio. At the applied frequency of 5 MHz, increased electric field strength leads to an increased crystallinity because of the larger strength of electrostatic coupling and induced polarization of the particles.

Turning to the effect of frequency, higher crystal quality was observed for applied frequencies greater than 0.5 MHz. The applied frequency affects self-assembly through its role in determining the polarization of the dielectric particles. That is, the polarization is affected by the movement of ions around the particles and the dielectric relaxation of the electrolyte[10]. Both of these polarization phenomena are frequency dependent. For micrometer-sized particles, ion migration around the particles is significant for kilohertz frequencies and lower. For particles in salt solution with concentrations at 0.1mM, the frequency scale for electrolyte relaxation is megahertz and lower. In our system, for a fixed electric field strength (E=32kV/m), assembly quality tended to increase as frequency was increased (Figure 3.2(d)). Previous studies on polarization-induced pair forces between particles[10] indicate that polarizability, and hence dipolar attraction strength, tend to decrease with frequency, because polarization mechanisms active only at slow timescales can no longer contribute to total particle polarizability. Other

studies[82] have also observed complex effects of AC field frequency on ellipsoidal self-assembly; these effects warrant further study.

The order-to-disorder transition of particles under and AC electric field occurs as dipolar interaction energy scales approach and exceed the thermal energy scale[10]. However, the quality of crystalline assembly for dipolar energy scales significantly above the system thermal energy are expected to be low; for attractions which far exceed system thermal energy the number of kinetically trapped defect states is expected to be high. `Jammed' states with high disorder and low particle mobility have been observed in many attractive colloidal systems, and generally arise when interparticle attraction far exceeds thermal energy scales in dense systems[114].

Our results indicate that higher particle polarizability does not necessarily result in a greater degree of crystalline order in dense systems. The peak voltage (which increases polarizability) and frequency (which decreases polarizability) of the applied AC field should be tuned so as not to produce jammed states. In simulation, we assume static charges on both ends of particles to represent the AC polarization modeling at higher applied frequency, similar to as reported in Azari et al.[113]. We also maintain a fixed maximum dipolar interaction strength between particles, so as to focus on the effect of geometry alone on crystal assembly quality.

3.5.2 Comparison of simulation and experiment

The experiments and simulations, while matching qualitatively, show some quantitative differences. One difference is the magnitude of the kinetic effects observed in the ellipsoids upon melting: the melting rate constant for ellipsoids relative to spheres is greater for the experiments than the simulations (Table 3.2). The pair potential model employed in the simulations is a simplified representation of the true interactions; the model neglects two effects which could contribute to the discrepancy between experiments and simulations. First, bulk flows of solvent

which would drive cooperative motion were not included in this MD integration method. Differences in particle shape and starting crystal structure may lead to differences in the hydrodynamics of these systems. Secondly, the discrete-charge model used here to represent particle polarization (see Supplementary Information) does not depend upon the angle of the particle relative to the applied field. Experimentally, the polarization of an ellipsoid will change depending upon its orientation relative to the field.

Another difference between experiment and simulation is the difference in melting rates observed for the two sets of diffraction peaks in the sphere systems. Despite their inherent symmetry, spherical particles are driven to assemble by the application of a unidirectional field, which breaks the symmetry of the SALS peaks aligned with that field direction. Simulation results show that crystalline order corresponding to these in-line peaks melt slower than the others, while the reverse is true of experiments (Table 3.2). The sphere structure can be thought of as a set of linear chains that have joined in the direction lateral to the field via inter-chain attraction. The difference between intra- and inter-chain attractive strength controls the steady state field-on configuration of intra- and inter-chain spacing, and hence the melting kinetics of these neighbor bonds. The slower breakup of intra-chain bonds in the simulated systems implies that the discrete-charge model (see Supplementary Information) used to represent particle polarization produces a higher ratio of in-chain/out-of-chain bond strength than observed in experiment.

3.6 Conclusions

We have shown that crystals of ellipsoids assembled under AC fields lose their positional order during melting at rates that are more than five time more rapid than for spheres in the same condition. Molecular dynamics simulations confirm that the anisotropy of the ellipsoids has a

significant effect on crystal melting kinetics, while exerting limited influence over crystal freezing kinetics. In addition, simulations of ellipsoids with and without rotational degrees of freedom demonstrate that it is the Brownian rotation of the ellipsoids that is responsible for the faster melting kinetics relative to spheres. Insights from our work can be applied to design the kinetics of reconfiguration of colloidal crystals.

3.7 Supplementary Information

3.7.1 Molecular dynamics methods

Simulations of colloid assembly and disassembly were carried out with HOOMD-Blue[77,83] using Langevin dynamics integration. The experimental forces present on colloidal particles arise from several sources and were represented using different simulated analogs. Figure *3.4*(a) schematically illustrates the particle interaction model used. Simulation units can be converted to physical units by choosing a set of self-consistent base units. Thermal energy can be converted to temperature by the expression $T_{phys} = E\, kT_{sim}/k_b$, where E is the energy base unit and $k_b$is Boltzmann's constant in units matched to E. By choosing E to be the energy required to lift the polystyrene ellipsoids used in this study (immersed in water) by two times their minor axis, the simulation thermal energy of 0.1 corresponds to 300K. Other energies reported here are given in terms of this thermal energy. In our simulations, the mass unit is taken to be the mass of one polystyrene sphere of diameter 4um. The distance unit is the sphere diameter. With these units and the energy unit, the conversion factor for time is $\tau = \sqrt{mD^2/\epsilon}$, where m, D, and ϵ are the mass, distance, and energy units respectively.

Particle-particle interactions are modeled using a Gay-Berne ellipsoidal potential[115] to represent hard core anisotropic repulsion and mild direction-independent attraction. The value of

ε in the Gay-Berne potential is chosen as $2.0kT$. For particles in quasi-2D, this is insufficient to induce condensation into a dense fluid. The major and minor axes of the prolate ellipsoid represented by this potential are chosen so that the minimum-energy isosurface encloses the same volume for spheres (minor axis equal to major) and ellipsoids (axis ratio of 2). The Gay-Berne potential was truncated at a distance of 4 times the major axis of the particles being simulated.

Anisotropic attractions and repulsions between particles are the result of electrostatic forces as particles are polarized in the AC electric field device used for self-assembly. This induced polarization is represented discretely, following Crassous et. al.[82]. Rigid bodies[83] were used to enforce the relative orientation and position of two charge-representing particles (positive and negative) placed on the ellipsoid major axis with respect to the ellipsoid center. The separation of these charge-representing particles was chosen to be a function of aspect ratio (α), linearly decreasing from 1.75 times the particle major axis length at $\alpha = 1.0$ and 1.6 times the particle major axis length at $\alpha = 2.0$. These values are chosen to reproduce the experimentally observed crystal structure of 2D assemblies at $\alpha = 1.0$ and $\alpha = 2.0$. The charge-representing particles have their interaction strength scaled to a common value for the closest distance of approach at the Gay-Berne minimum-energy isosurface. For spheres, this distance is parallel to the applied field direction. As α is increased, the closest distance from a point on the major axis to the ellipsoid edge is no longer parallel to the field direction. By choosing to scale charged interactions in this way, the simulation model matches the sphere-sphere and ellipsoid-ellipsoid electrostatic bond strength. Charge based particle-particle bonds are compared at a common strength for spheres and ellipsoids. This focuses the model on the effect of geometric changes of the particle's shape. The value of all charge-mediated bonds was scaled to $6kT$ at the surface of the ellipsoidal repulsion.

The electrostatic interactions were truncated at a range equal to twice the diameter of the simulated spheres.

In experiment, ellipsoids are observed to align with the electric field direction, as reported in the main text. The alignment force is represented in simulation by a constant force applied (in opposite directions) to each charge-representing particle. To determine the strength of these alignment forces, a maximum angle is chosen. The forces are then scaled so that the integrated work of turning a particle from alignment with the field to the chosen angle while under these forces is equal to kT. In this parameterization scheme, the maximum deviations of particle alignment from the force direction during a thermalized simulation are approximately equal to the chosen maximum angle. For all simulated systems shown here, the maximum angle was chosen to be 60°.

Sedimentation is represented in simulation by the application of a constant downward force and a repulsive wall in the xy-plane. For all systems shown here this force was chosen as $F = 20kT/D$, where D is the diameter of an $\alpha = 1.0$ particle. This force is applied to the particle centers. Ellipsoidal particles are prevented from rotating out of plane when the alignment field is turned off by the repulsive effect of the wall. The wall interacts with particle centers and charge-representing particles via a Weeks-Chandler-Andersen[116] repulsive potential. Any rotation of particles out of plane forces the body center to a higher z-position, thereby incurring an energy penalty. All particle simulations shown here are systems with 10,000 colloid particles. All boundaries are periodic.

Model parameter fitting to recapitulate the observed experimental crystal structure, which was then the basis for the characterization of kinetics, was most sensitive to the position of the charge-representing particles within the repulsive core. For ellipsoidal particles, different

separations of the charged particles along the major axis can produce the crystal structure experimentally observed for spheres or that observed for $\alpha = 2$ ellipoids. For spheres, the preferred motif of charge-mediated interactions is to form chains. Inter-chain attraction due to charge forces alone was too weak to result in long range 2D crystals. The attractive component of the Gay-Berne potential was needed to provide a weak direction-independent attraction in order for spheres to fully order. Given the unknowns present in the electrodynamics of the fluid and particle polarizations, applying an isotropic attraction in this manner was deemed an appropriate, parsimonious approximation. Changes to the angular freedom of particles under 'field-on' conditions were not found to have strong consequences for phase behavior of the model, but instead introduced additional spread into the peaks present in the Fourier domain representation of the crystals. The magnitude of the downward force (representing the effect of particle settling) needed to be sufficiently large to prevent the formation of 3D cluster assemblies but was otherwise unimportant.

3.7.2 Structural characterization

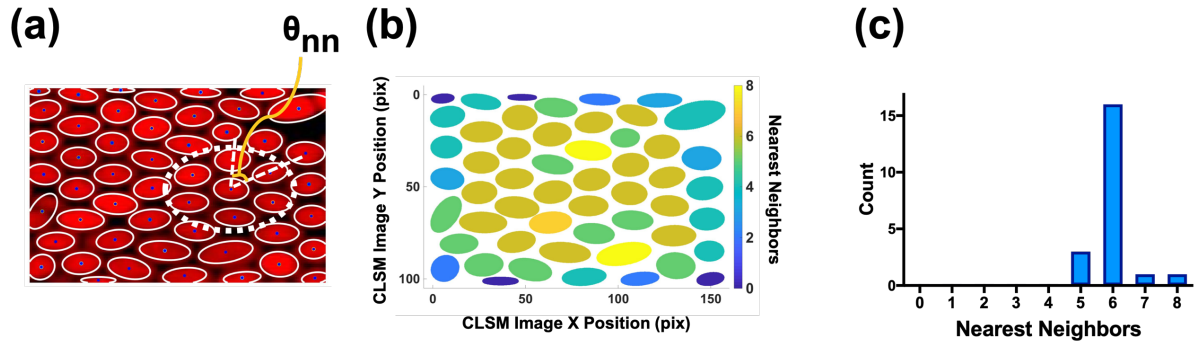

Figure 3.7 (a) The white dotted region illustrates the elliptic coordination shell for determining the positional order parameters, including the nearest neighbors and the nearest neighboring angles of a self-assembled structure. (b) The map of local nearest neighbors of the close-packed assembly as shown in Figure 3.7-(a). (c) The counts of nearest neighbors of the close-packed assembly as shown in Figure 3.7-(a). Particles at the edge are excluded in the counting.

In this study, we determine the number of nearest neighbors of a colloid as those within a set radius of that colloids surface. We set this radius of the elliptic coordination shell to be 2.1 times the second peak of g(r) of the close-packed colloidal ellipsoids array, as shown in Figure 3.7(a). The overall positional order of the assembly environment of Figure 3.7(a) is shown in Figure 3.7(b). Particles at the periphery of the microscopic image are not considered because all their neighbors cannot be identified due to boundary effects. Figure 3.7(c) shows that for the close-packed assembly in Figure 3.7(a), 76% of the ellipsoidal particles have six nearest neighbors. The average number of nearest neighbors of this assembly is 6.0±0.6.

We computed nearest neighboring angles, θ_{nn}, from CLSM images as another local order parameters to quantify short-range positional order of colloidal assemblies. θ_{nn} are the angles between each two adjacent vectors within the elliptic coordination shell. For example, for each spherical particle in a hexagonally close-packed assembly, there are six nearest neighboring angles, each with the value of 60°.

3.7.3 Small-angle Light Scattering Apparatus and Characterization

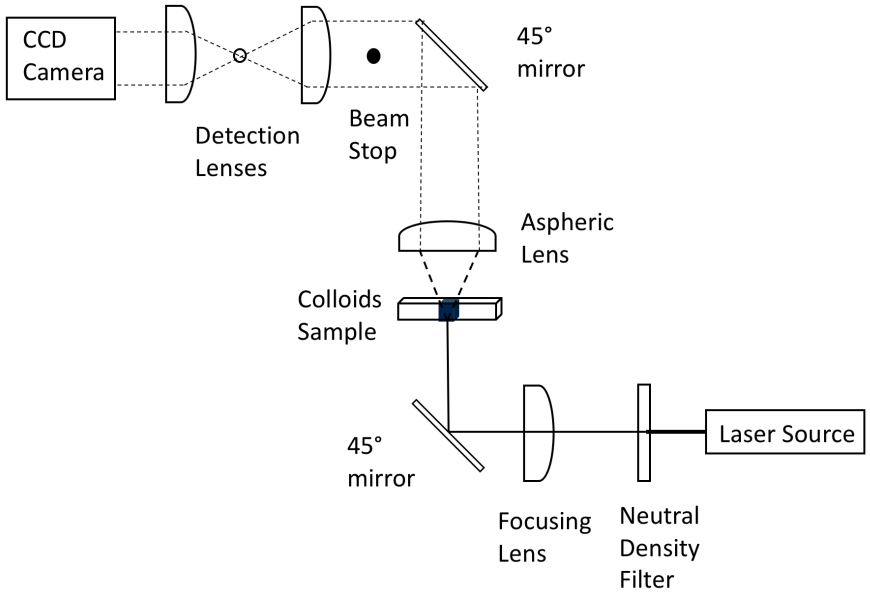

Figure 3.8 Schematic of the small-angle light scattering apparatus.

The SALS device collects real-time light diffraction measurements over the angular range of 2°-13°. The performance of the device, assessed by comparison to calculations by Mie scattering theory, is good to within 12.5% from 2° to 12°.

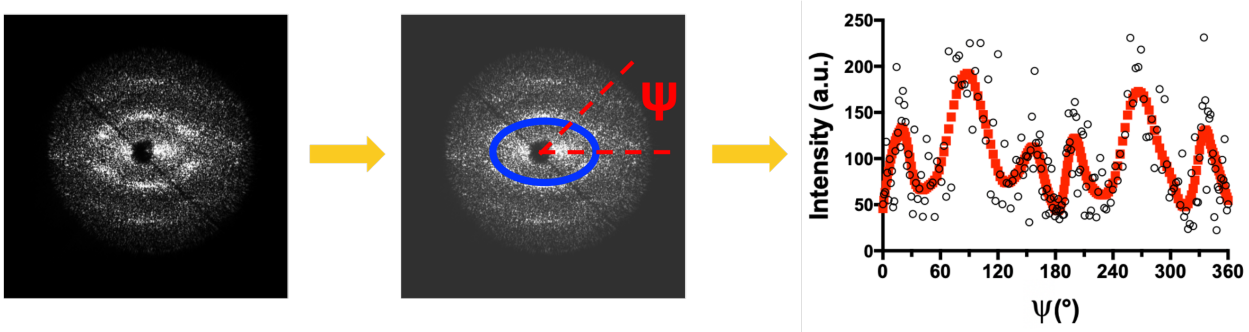

Figure 3.9 Analysis of the small-angle light scattering (SALS) data. In the first order scattering peaks (the blue elliptical ring), ψ is defined as the angle between the semi-major axis of the elliptical ring and the line connecting a peripheral point to the centroid of the elliptical ring. The intensity of light scattering responses varies at each ψ within the first order scattering responses.

The blue ring shown in S3 has a finite width of 31 pixels due to the average width of the primary scattering patterns being 31±2 pixels.

3.7.4 Evolution of Grain Microstructure by Molecular Dynamics

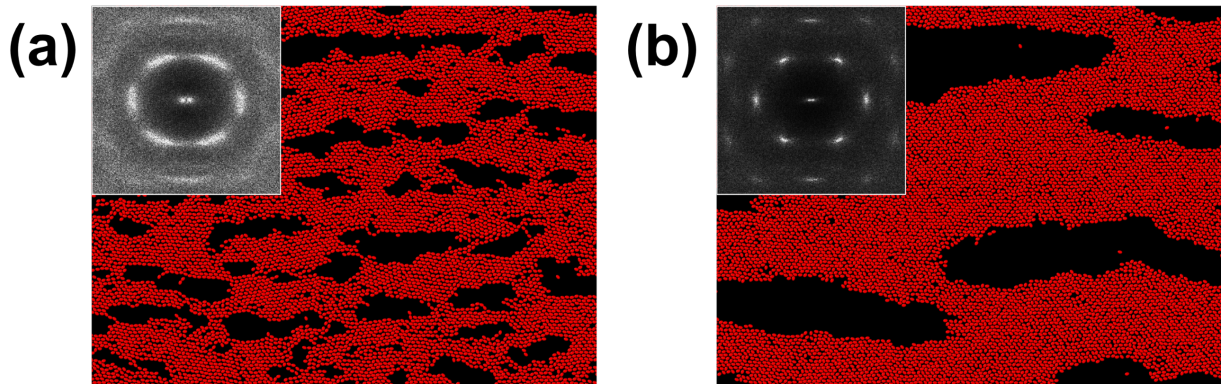

Figure 3.10 The evolution of simulated grain microstructure. (a) System snapshot and Fourier domain pattern for ellipsoids with an axis ratio of 1.4 after 20 seconds of simulated time with the field on. (b) The same system after 11 minutes of simulated field-assisted assembly. Differences in the system's Fourier domain pattern and void structure are due to grain boundary annealing. The MD simulation results were collected by B. VanSaders

3.7.5 Comparison of Different SALS Measures

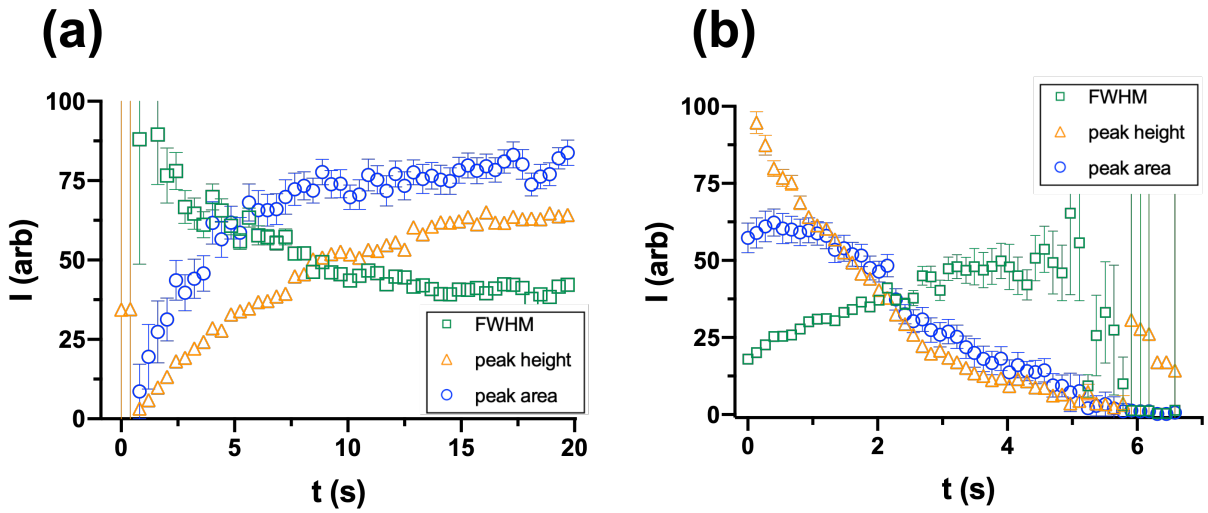

Figure 3.11 Comparison of different measures of a simulated SALS peak during (a) assembly and (b) melting for spheres. The intensities of curves have been scaled to allow comparison across the panels of the figure. The time scale of all curves is equivalent; however, the curve shape of peak area is most favorable for fitting as a useful convolution of the two other states, namely a low peak area state and high peak area state. In this study peak area is used, but equivalent conclusions can be drawn from any of these measures of the diffraction peaks. The MD simulation results were collected by B. VanSaders

Chapter 4 Ultra-efficient Elasticity in Colloidal Gels by Means of Particle Anisotropy[6]

4.1 Abstract

Physical gelation of colloids produces elastic structures that are used to stabilize industrial complex fluids. However, rheological control is greatly limited by the universality of the arrested spinodal decomposition mechanism that governs colloidal gelation. Because of their universal microstructure, volume fraction and pair particle bond strength are the limited tools available to manipulate gel modulus, and even these variables are often unavailable to formulators because they are otherwise deployed to achieve the gel's desired function. Here we demonstrate, through manipulation of shape anisotropy, that we can expand the design space for colloidal gels. Specifically, gels formulated from discoids exhibit expanded elasticity states that are shifted relative to the universal behavior of sphere gels by a factor of as much as 15. We apply a well-known predictive model of colloidal gelation and explain this efficient generation of elasticity as a series of multiplicative factors dependent on the network fractal dimension, the backbone topology, and the existence of non-central pair forces. Our study consequently reveals a new strategy for designing gels with tailored mechanics at ultra-low volume fractions.

4.2 Introduction

Colloidal gels are tenuous, sample spanning structures that exhibit soft, solid-like rheology such as finite elastic modulus and yield stress[2]. They are commonly used to impart

[6] The text in this chapter is in preparation for publication by P. Kao, M. J. Solomon, and M. Ganesan.

quiescent elasticity to complex fluids such as paints, agrochemicals, and cosmetics[117–119]. Gels are formulated by quenching particles through strong, short-range pair potential attractions[120]. However, at low particle volume fractions ($\phi \leq 0.1$) – where industry often seeks to operate due to cost – rheological control of gels is greatly hampered by the universality inherent in colloidal gelation[121,122]. Specifically, studies have established that gelation proceeds generically through a process of arrested spinodal decomposition[120]. At these dilute colloid concentrations, this mechanism of spinodal decomposition presents as diffusion limited cluster aggregation (DLCA) leading to fractal cluster structure[2,120]. The fractal dimension (d_f) describing the DLCA gel microstructure is a universal value, $d_f \approx 1.8$[120,121]. The only other microstructural parameter, the cluster size, is determined by the gel volume fraction. Gel rheology is consequently tunable only by particle volume fraction, ϕ and interparticle bond strength, often quantified as the bond spring constant[123]. Romer et al show that in the range $10^{-3} \leq \phi \leq 10^{-1}$, the ϕ dependence of the linear shear elastic modulus, G' of colloidal gels consisting of spherical monomers collapses onto a universal curve when normalized by particle size[124]. This universality implicitly constrains opportunities to design the elasticity of colloidal gels. The possibility to overcome this constraint by altering the attractive interparticle potential is often unavailable to formulators because factors that mediate attractions (e.g. salinity, solvency, and additive concentration) are typically otherwise deployed to satisfy the functional requirements of the formulation. Technologically, it would be particularly useful to engineer efficient gels with high G' at low volume fraction since this combination is effect from the point of view of both sustainability and cost. We here propose and test an approach to step outside the constraints imposed by the universality of arrested spinodal decomposition. In doing so, we reveal a previously unknown relationship between gel microstructure and elasticity. We uncover the microstructure-rheology link and

show how to generate ultra-efficient efficiency in colloidal discoid gels – at volume fractions up to 15 times less than spherical gels. Our results suggest new ways in which colloidal building blocks might be constructed for design and control of colloidal gels

There are prior indications that shape anisotropic colloids can produce fractal objects with unusual microstructural and microrheological behavior. For instance, DLCA of colloidal rods yielded networks with d_f that had a strong dependence on particle aspect ratio, deviating from the universal value of ≈ 1.8 found for colloidal spheres[125,126]. Furthermore, the localized microdynamics of rod aggregates showed an unforeseen transition from floppy to brittle behavior that departed from microrheological theories of cluster dynamics[33,123]. Other early studies showed that aggregate networks of anisometric colloids exhibit higher interfacial modulus[127] and yield stresses[128,129] than the case in which the primary constituents were simply spheres. However, the specific mechanism by which shape anisotropy mediated these different elastic states is not known. Speculations as to the mechanism have included non-central pair forces[33,129], anisotropy in excluded volume[125], as well as an increase in the number of contacts per particle[33,130] due to the asphericity of particle shape. Moreover, although anisotropy effects on gelation boundaries have been discussed[32], the specific shifts in gel elastic modulus due to anisotropy have been neither quantified nor explained.

Inspired by the fact that the shape and structure of carbonaceous building blocks lead to non-universal features in the fractal aggregation of soot[131], we here explore the idea that colloidal particle shape anisotropy can likewise generate gel microstructures that deviate from the universal features of the arrested spinodal decomposition of spheres. We use colloidal discoids as a model system because recent progress in fabrication techniques yield uniformly sized colloids in quantities sufficient for rheometry[132,133]. The discoid shape is furthermore common in

engineered[134] and living systems[135]. Across multiple aspect ratios, r, we observe that the ϕ dependence of G' in discoid gels exhibits a remarkable shift from the universality of sphere gels. In addition to a shift of the modulus curve to very low volume fractions, we also find that the power-law exponent describing the ϕ dependence of G' changes with r. We investigate the microstructural origin of these phenomena by characterizing particle-level connectivity through confocal microscopy and morphological image analysis. These independent measures of microstructure are inputs into the well-known predictive theory for the elasticity of fractal cluster gels developed by Shih and co-workers[136,137]. We find that the fractal dimension and shape of the elastic backbone in discoidal gels differs from the universal values for spheres; these differences explain the r dependence of the $G' - \phi$ power-law exponent. In addition, the anisotropy in pair potential interactions contributes an aspect ratio dependent shift in the volume fraction dependence of the elastic modulus.

This work reveals a simple, efficient means for expanded design and control of the rheology of colloidal gels. In addition to its direct utility for producing and using colloidal discoid gels, the identification of the specific mode by which the discoidal shape impacts the rheology is further significant. Our study therefore motivates further research on the capabilities afforded by anisometric building blocks to self-assembly colloidal gels with rheology that accesses regions of the design space that were previously unavailable.

4.3 Results

4.3.1 Colloidal gels assembled from discoids of different aspect ratios

Discoids used in this study are prepared by thermo-mechanical squeezing of spheres[132]. The seed polystyrene (PS) microspheres (diameter $2A$ = 1.00 ± 0.02 μm) were embedded in a polymer film and heated above their glass transition temperature in a bench-top press (c.f.

Methods, Figure *4.7*). Uniaxial compression at pressures of 750, 2800, and 4200 kPa were applied, resulting in discoids with aspect ratio, $r = (B/A) = 0.42 \pm 0.01$, 0.20 ± 0.01 and 0.09 ± 0.03 respectively. The major axes for these particles are $2A = 1.34 \pm 0.02$ μm (for $r = 0.42$), 1.72 ± 0.01 μm (for $r = 0.20$) and 2.23 ± 0.04 μm (for $r = 0.09$); the corresponding minor axis are $2B = 0.56 \pm 0.01$ μm, 0.35 ± 0.01μm and 0.21 ± 0.01 μm. Figure 4.1(a)-(d) show scanning electron micrographs of the seed spheres and the as fabricated discoids. Insets in Figure 4.1(b)-(d) provide an orthogonal view; the shape uniformity and successive flattening of the spheroidal shape of the particle with decreasing aspect ratio are apparent.

Particles were suspended in a density-matched mixture of H_2O-D_2O and gelation was induced by addition of 10mM $MgCl_2$[138]. The salt screens charges on the particle surface promoting short-range van der Waals attractions that drive gelation through a DLCA process[120,123]. Figure 4.1(e)-(l) compares maximum projections of the three-dimensional structure of the self-assembled colloidal gels. A self-similar, fractal structure is apparent for both the sphere ($r = 1.00$) and discoid ($r = 0.09 – 0.42$) gels. The heterogeneous, inter-connected microstructures that span the image space at intermediate length scales (Figure 4.1 (e)-(h)) are seen to persist even at smaller length scales shown in Figure 4.1(i)-(l). This description is consistent with the well-known fractal cluster architecture of dilute colloidal gels[139]. In addition, the gels formed by discoids possess a microstructure (Figure 4.1(j)-(l)) that is interspersed with both condensates – aggregates with no orientational ordering, and strands – particles with a face-to-face orientational alignment. This mixture of partially ordered and disordered aggregates is similar to the configuration reported by Hsiao et al. for discoids self-assembled by means of the depletion attraction[140].

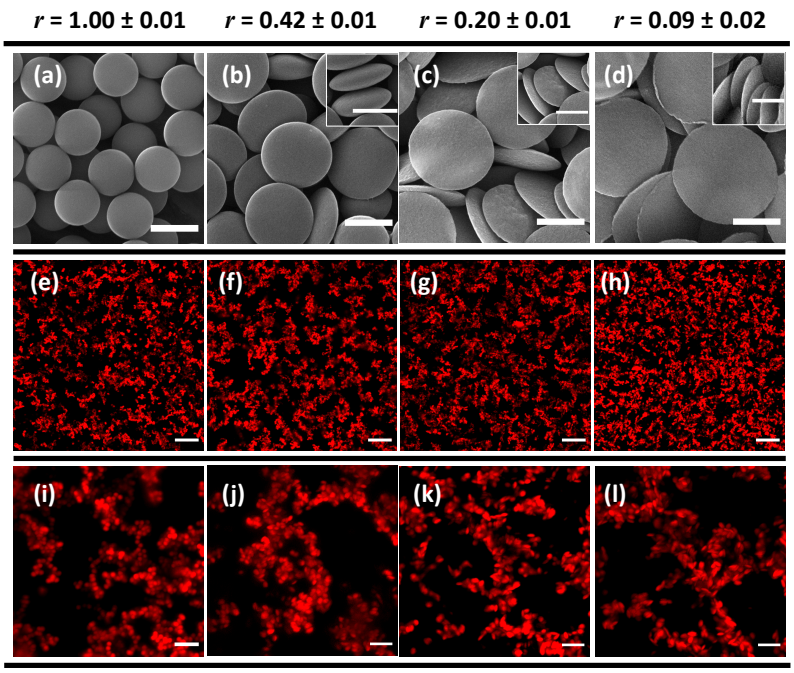

Figure 4.1 (a-d) Representative SEM images of colloidal particles with aspect ratio r = 1, 0.42, 0.20, and 0.09 respectively. Insets of different viewing angles show the thickness of the discoids. Scale bars for (a-d) are 1μm. Confocal projections ($\Delta z = 20\mu m$) of colloidal gels with aspect ratio r = (e, i) 1.0, (f, j) 0.42, (g, k) 0.20, and (h, l) 0.09. Here, $\phi = 0.015$ and [$MgCl_2$] = 10 mM. Scale bars are (e-h) 20 μm and (i-l) 5 μm.

4.3.2 Gel rheology and aspect ratio dependence

In the range of volume fractions studied here, both sphere and discoid gels exhibit similar functional dependence of G' on oscillatory strain (γ): a linear regime with plateau elasticity at low strains ($\gamma < 0.003$) followed by an onset of non-linearity and a rapid drop in modulus with increasing strain amplitude (Figure 4.2, Figure 4.8). The tan(δ) – defined as the ratio of viscous to elastic modulus – is about 0.20 in the linear regime and increases to values > 1 in the non-linear regime (insets in Figure 4.2 and Figure 4.8). The finite G' together with $\tan(\delta) < 1$ indicates a solid-like, elastically dominated response, characteristic of physical gels[138]. At higher strains, the rapid loss of elasticity represents a fluidization transition[141].

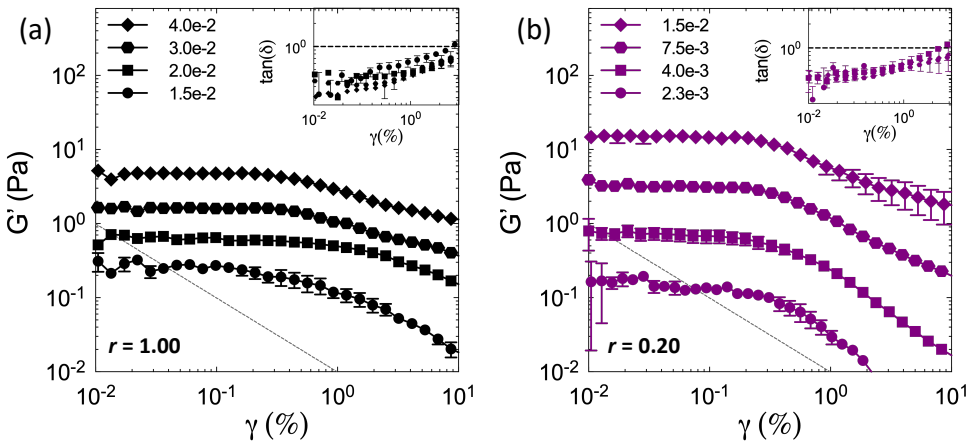

Figure 4.2 Storage modulus (G') and (inset) tan(δ) as a function of strain amplitude, γ at ω = 1 rad/s of colloidal gels made from (a) spheres (r = 1.00) and (b) discoids (r = 0.20). Dotted line indicates the instrument sensitivity limits (c.f. Methods). Corresponding strain sweep measurements for r =0.42 and r = 0.09 discoids are included in Figure 4.8.

Extreme differences between discoidal and spherical gels are seen by plotting the dependence of their linear storage moduli on volume fraction (Figure 4.3). First, we observe elastic rheology in discoid gels at a volume fraction that is more than an order of magnitude lower than spheres. For instance, sphere gels display a G' = 0.2 Pa at ϕ = 1.50% while gels consisting of r = 0.20 and r = 0.09 discoids already exhibit similar elasticity at ϕ = 0.23% and 0.11% respectively. Relatedly, quiescent gels made from the discoids are about 10^1–10^2 fold stiffer than spherical gels at fixed volume fraction, with level of stiffening increasing with anisotropy. For example, at ϕ = 1.50 %, G' = 0.17 Pa and 18 Pa for sphere and r = 0.20 discoid gels, respectively. At ϕ = 0.75%, gel modulus increases by 20-fold as discoid anisometry increases from r = 0.42 to 0.09. Second, we find that the exponent, Π, describing the ϕ dependence of G', $G' \sim \phi^{\Pi}$, decreases with decreasing particle aspect ratio: Π= 3.53 ± 0.16, 2.93

± 0.10, 2.52 ± 0.05 and 2.15 ± 0.15 for r = 1.0, 0.42, 0.20 and 0.09 respectively (Figure 4.3). These differences in the power law behavior are statistically significant ($p < 0.05$). The value Π = 3.53 for the sphere gels agrees with previous reports, which average Π = 3.51 ± 0.15[123,124,138]. The slower growth in elastic modulus with volume fraction for the anisotropic gels is in itself noteworthy and agrees with the shear rheology of rod[128,129] and platelet clay gels[142]. In addition to this feature, the power law curve itself shifts to progressively lower volume fractions with aspect ratio, culminating with a shift of 22.4 ± 5.5 at the lowest discoid aspect ratio. Figure 4.3 therefore shows that the shifts in pre-factor and exponent combine to generate very large absolute effects in gel rheology.

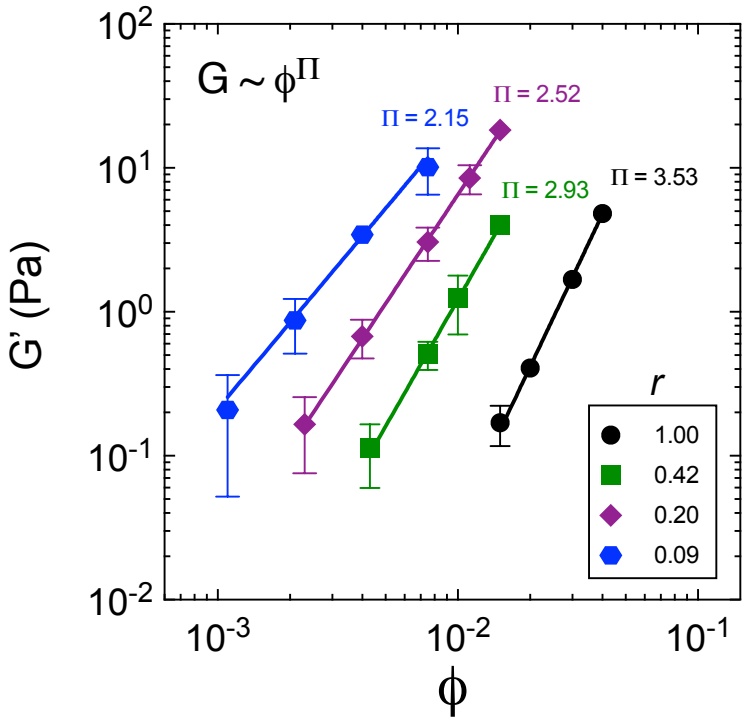

Figure 4.3 The dependence of linear storage modulus, G' on particle volume fraction ϕ for colloidal gels made from spheres (r = 1.00) and discoids (r = 0.42, 0.20 and 0.09). The reported G' is an average over the linear region which is identified as the strain amplitudes less than the point at which G' deviates by 5% from its maximum value[136].

4.3.3 Theory of gel elasticity

To develop an explanation for the aspect ratio dependence of the power law pre-factor and exponent, we apply a well-known predictive theory for elasticity in dilute colloidal gels. In this model, developed by Shih et al[136] and further extended by de Rooij et al[143], the gel microstructure is described as a random packing of fractal clusters and the gel elastic modulus is determined by the size and spring constant of the clusters. In the dilute limit ($\phi < 0.1$)[143], the model predicts:

$$G'(\phi) = f\kappa_0 V_p^{-\frac{1}{3}} \phi^{\frac{1+\beta}{3-d_f}} \qquad (4\text{-}1)$$

In this model, the pre-factor to the scaling with volume fraction is determined by: κ_0 – the interparticle bond strength, V_p – the hard particle volume and f – a modulus proportionality constant. The power-law exponent is described by: d_f – the network fractal dimension and β – an elasticity exponent expressed as $\beta = 2\epsilon + d_B$; ϵ and d_B are respectively the isotropicity and dimension of the stress bearing backbone[137]. As written, the model applies to general fractal cluster gels and does not specify particle shape[124]. As a consequence, it has been widely applied to study the rheology of gels formed from spheres (e.g. latex colloids[124,144,145], mineral particles[146,147]), spheroids (e.g. carbon nanotubes[148], boehmite ellipsoids[149], starch granules[150]), polymeric chains (e.g. proteins[151–153], polysaccharides[154–156], fat molecules[157]) and patchy particles[158]. Eqn (4-1) differs from the authors' model only in that the characteristic length scale in its formulation has been taken as $V_p^{1/3}$ rather than the original specification of particle radius, in anticipation of our applying the model to anisotropic particles.

Numerical values for the parameters in equation (1) are well known for DLCA sphere gels: $d_f \approx 1.85$, $\beta \approx 2.80$ and the modulus pre-factor $f \approx 1 - 3$ [33,124,144,145,159]. However, deviations in these parameters occur when the interparticle interactions and shape of constituent

monomers differ from those of simple spheres. For example, from measurements of the dynamic structure factor, Mohraz and co-workers found that gels consisting of rod-like particles displayed variations in both d_f and β with aspect ratio[33,125]. Simulations by West et al[160] showed that introducing angular rigidity in the gel backbone resulted in values of $\beta < 2$. Through theoretical fits to experimental rheology data, Laxton and Berg reported that the modulus pre-factor increased from f ~ 1-3 to f ≈ 50 for discotic clay gels[161]. In the subsequent sections, we report independent, confocal microscopy derived, determinations of the model parameters f, d_f, β and κ_0. We therefore generate a no adjustable parameters prediction of the aspect-ratio dependent gel rheology of Figure 4.3 by means of equation (4-1).

4.3.4 Fractal dimension of the gel network

We measure d_f from confocal image volumes. Here, we use box-counting analysis, which utilizes spatial intensity data to quantify the dimensionality of the structure[162,163]. Box analysis has previously been applied for quantifying the microstructure of colloidal sphere gels[164,165], albumin gels[151,166], plasma protein gels[167] and soot aggregates[168]. The method is well-suited to the discoid shapes studied here because it does not required centroid identification. Briefly, the number of cubes $N(L)$ of size L required to cover the gel are computed (Figure 4.4a) at different cube sizes, yielding d_f from the power-law $N(L) = c_1(I/L)^{d_f}$, where I is the image size and c_1 is a proportionality constant (c.f. Methods). Figure 4.4b shows the resulting log-log plot. The fitted lines corresponding to all r = 0.09 – 1.00 gels have power law slope of magnitude smaller than three, confirming the fractality of these structures.

Figure 4.4(c) shows that increasing particle shape anisotropy causes an increase in gel d_f. For sphere gels (r = 1), d_f = 1.86 ± 0.02, is consistent with the DLCA value of $d_f \approx$ 1.85[144,158,169]. For discoid gels (r < 1), the value increases up to d_f = 2.04 ± 0.02 for the lowest

aspect ratio discoid (r = 0.09). This result is consistent with prior measurements for gels of rodlike particles (r > 1), which also reported an increase in gel d_f with increasing monomer anisotropy[125]. In Figure 4.4(b), the curves display an upward shift with aspect ratio, indicating an increase in c_1 (inset Figure 4.4(c)).

The increase in network dimensionality indicates a deviation from the universality of DLCA aggregation[121]. Higher d_f indicate that discoids form denser cluster than spheres. The reason for the increased fractal dimension is attributed to the anisotropy in excluded volume as per simulations reported by Mohraz et al[125]. Physically, the shift in the c_1 indicates that the discoid fractal structures are more space filling relative to spheres. For instance, for a given box-size, r = 0.09 discoid gels require seven-fold more boxes to fill the gel structure.

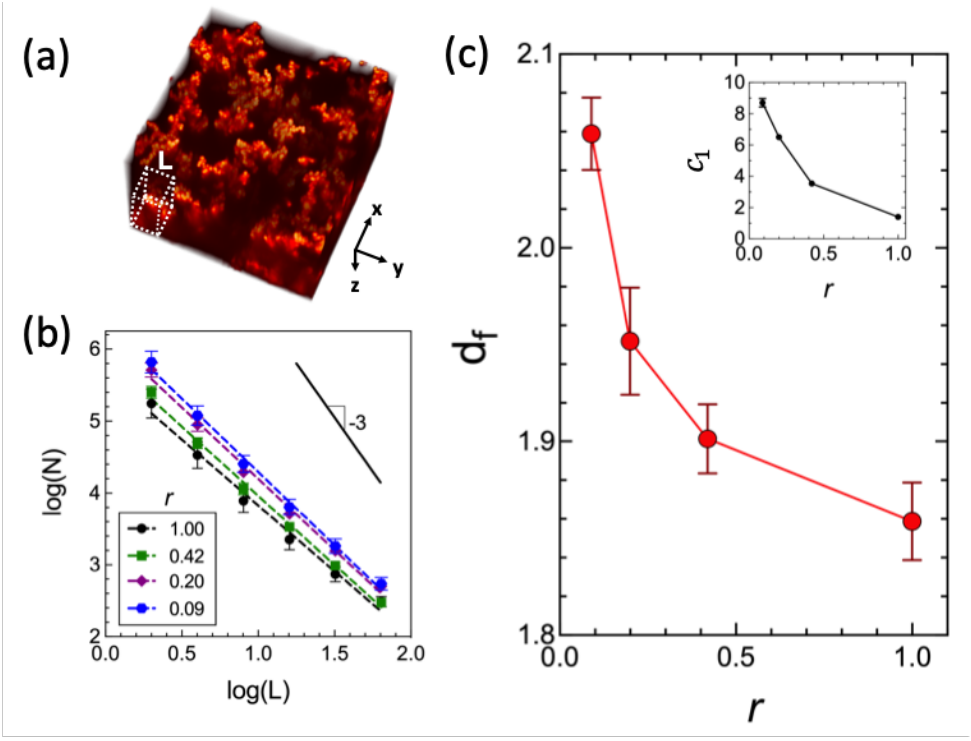

Figure 4.4 (a) 3D confocal microscopy visualization of the spheres colloidal gels to characterize fractal microstructure. Here, $\phi = 0.015$ and [$MgCl_2$] = 10 mM. The white dotted lines illustrate a single cube in the box counting method. L is the resolution of the cube. (b) Log-log plot of number of cubes vs. cube

size for colloidal gels made from spheres (r = 1) as well as r = 0.42, 0.20 and 0.09 discoids. The slope of the curve is the fractal dimension of the aggregates. The solid line represents a Euclidean scaling of $N \sim L^{-3}$. (c) The fractal dimension of colloidal gels d_f as a function of aspect ratio r. (inset) Prefactor c_1 as a function of r. The lines are included to guide the eye.

4.3.5 Backbone dimension and isotropicity

We extract the gel backbone from confocal image volumes using skeletonization – a sequential thinning process that produces a voxel-thick skeleton that encodes the topography of the gel (c.f. Methods). The technique reconstructs the three-dimensional backbone from this intensity map. It has been applied to measure backbone tortuosity of pNIPAm colloidal gels[170], nanoparticle aggregates[171] and osteocyte networks[172]. The backbone dimension, d_B is obtained from the relation between the length of the shortest path, l, between any two points on the skeleton and the end-to-end distance, r_E between them: $l = c_2 r_E^{d_B}$ [159,173]. d_B reflects the tortuosity of the chain. The isotropicity, ϵ is given as $r_\perp^2 = c_3 r_g^{2\epsilon}$ where, $r_\perp$ is the radius of gyration of the shortest path projected onto a plane perpendicular to its end-to-end axis and r_g is its center-of-mass radius of gyration[174,175]. de Rooij and co-workers identify the following limiting cases for these two parameters: $\epsilon = 1$ and $d_B = 1.3$ applies for an isotropic flexible backbone leading to gels with lower elasticity, while $\epsilon = 0$ and $d_B = 1$ apply to an anisotropic rigid backbone leading to higher gel moduli[143]. Here, c_2 and c_3 are proportionality constants.

The skeletonization reveals the gel microstructure as a sparse, interconnected network interspersed with voids (Figure 4.5(a)). Figure 4.5(b)-(c) shows the corresponding plots of l vs r_E and $r_\perp^2$ vs r_g and the power-law fits to obtain d_B and ϵ, respectively. For sphere gels, the value $d_B = 1.26$ and $\epsilon = 0.80$ agrees well with the results of computer simulations (d_B = 1.30 and ϵ = 0.77)[173,176,177] and direct measurements by Dinsmore and Weitz ($d_B = 1.20$ and ϵ = 0.7)[159]. With

increasing anisotropy, we find that d_B, ϵ (inset of Figure 4.5(d)) and consequently the elasticity exponent, $\beta = 2\epsilon + d_B$ (Figure 4.5 (d)) rapidly decrease, culminating at a value of β = 1.66 $\pm$ 0.08 for the lowest discoidal aspect ratio. A similar result was observed for rod gels where a value of $\beta \approx 1.20$ for r = 3.9 – 30.1 was measured by dynamic light scattering[33]. The constants c_2 and c_3 are of order unity and relatively insensitive to r (Figure 4.5(b)-(c)).

The decrease in β indicates that the stress backbone in discoidal clusters becomes progressively more anisotropic relative to spheres as the discoid aspect ratio decreases. Mechanistically, lower values of β have been link to an increase in angular rigidity of the gel network[160]. However, the microstructural origin for this behavior in gels of anisotropic building blocks is not known. Mohraz and Solomon[33] hypothesized that, in clusters of anisotropic particles, the presence of noncentral forces and additional contacts per particle limit bond rotations. This limitation leads to gel backbones with large angular rigidity. This rigidity results in values of β that are lower than those reported for spheres. Comparing to sphere gels, centro-symmetric forces in this case allow pivot points along the gel backbone. These pivots generate a more flexible backbone. This hypothesis is supported by recent simulations that show non-centrosymmetric interactions produce gels with less tortuous backbones[178] and higher macroscopic shear modulus[179].

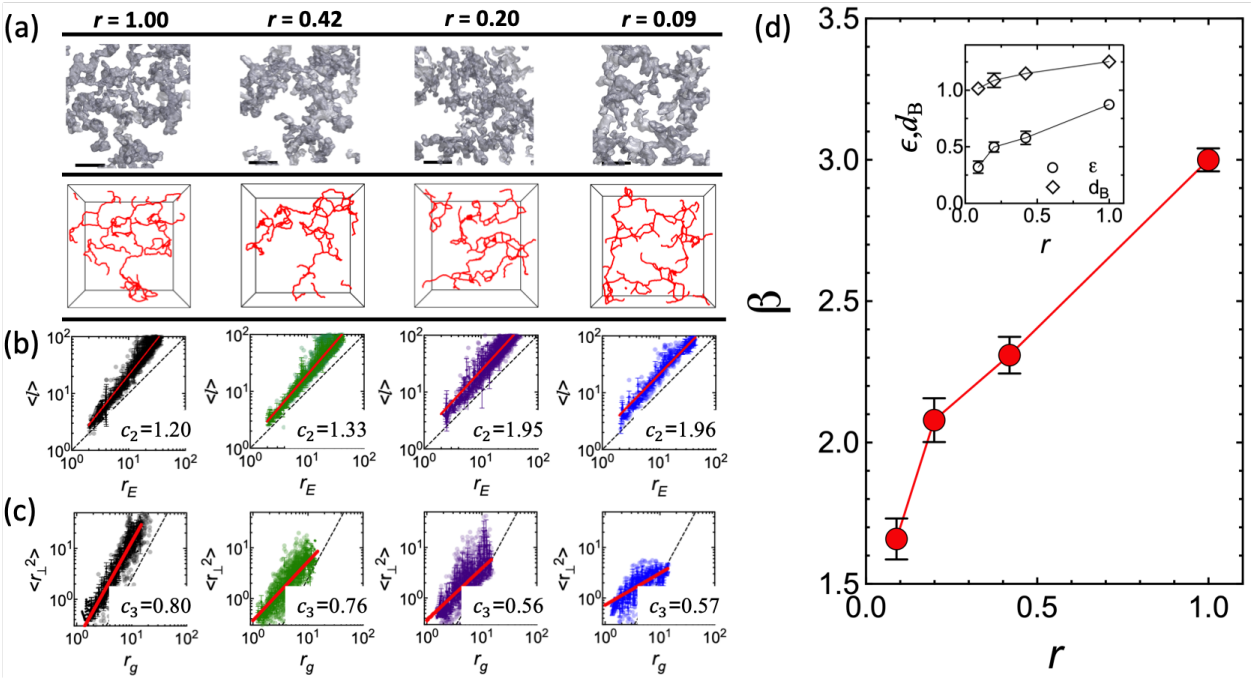

Figure 4.5 (a) Representative iso-surface rendering of binarized image volumes of the gels (top row) and their corresponding backbone extracted using skeletonization (bottom row). The aspect ratio of constituent particles are indicated on the top. (b) Log-log plot of $\langle l \rangle$ versus r_E for different aspect ratio gels to determine the backbone fractal dimension d_B. The solid lines are power-law fits $\langle l \rangle = c_2 r_E^{d_B}$ and the dashed lines indicate the case d_B=1.00. Values of the pre-factor c_2 are included in the inset. (c) Log-log plot of $\langle r_\perp^2 \rangle$ versus r_g for different aspect ratio gels to determine the isotropicity, ϵ. The solid lines are power-law fits $\langle r_\perp^2 \rangle = c_3 r_g^{2\epsilon}$ and the dashed lines indicate the case ϵ =1.00. Values of the pre-factor c_3 are included in the inset. (d) Aspect ratio dependence of the elasticity exponent β and (inset) bond dimension, d_B, isotropicity ϵ. Lines in (d) are drawn to guide the eye. The backbone dimension and isotropicity analysis were conducted by Dr. M. Ganesan.

4.3.6 Interparticle bond and spring constant

The interparticle bond strength, κ_0 is calculated from particle pair-potentials using the equipartition theorem, $\kappa_0 = k_B T/(\langle s^2 \rangle - \langle s \rangle^2)$ [158,180]. Here, s is the surface-to-surface separation between particle pairs and $\langle \cdot \rangle$ represents a Boltzmann weighted average[158]. Discoid pair potentials are calculated using the expressions of Schiller et al[181].

As indicated in the preceding section, for spheres, the attraction is centro-symmetric; for discoids however, the shape anisotropy results in noncentral forces[182]. To highlight the interaction anisotropy accorded by particle shape, four limiting configurations of discoid pairs,

namely face-to-face (F-F), edge-to-edge (E-E), edge-to-face (E-F) and edge-on-edge (ExE) and their respective pair-potentials (calculated for $r = 0.20$) are shown in Figure 4.6(a)-(b). The interaction strength varies with relative orientation. F-F alignment results in the strongest bond significantly higher than that between two spheres – while E-E and E-F result in relatively weaker pair forces (Figure 4.6(b)). The stronger potential energy for F-F alignment was also observed in discoids interacting through depletion forces[182]. As a first approximation, we assume a uniform contribution of these configuration to the spring constant $\langle \kappa_0 \rangle$. This level of approximation is consistent with the use of $V_p^{1/3}$ as the characteristic length in equation (4-1). Figure 4.6(c) shows the degree to which the bond strength increases with shape anisotropy. For the lowest aspect ratio discoid, the bond strength increases by a factor of 6 relative to interacting spheres. The increase in $\langle \kappa_0 \rangle$ with monomer anisotropy indicates that, on average and in the range of discoidal shapes studied here, discoidal bonds are stronger than spheres.

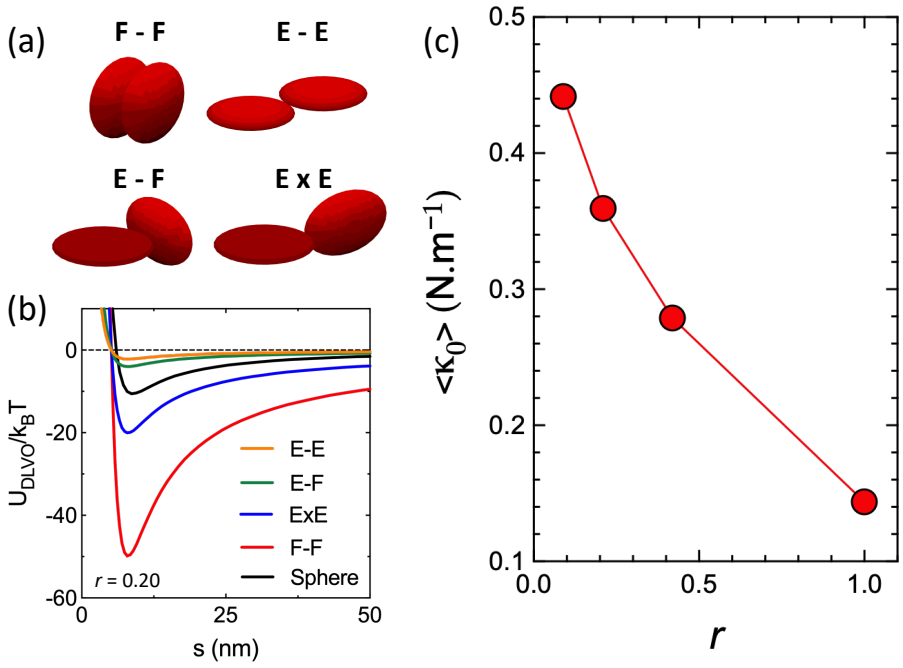

Figure 4.6 (a) Limiting cases of the pairwise orientation distribution function of discoids: face-to-face (F-F), edge-to-edge (E-E), edge-to-face (E-F) and edge-on-edge (ExE). Discoids are not drawn to represent any specific aspect ratio used in this study. (b) DLVO pair-potential, U_{DLVO} normalized by k_BT for sphere pairs and discoid pairs corresponding to relative orientations shown in (a). Discoid pair-potentials are for the case r = 0.20. (c) Aspect ratio dependence of the orientationally averaged bond spring constant $\langle\kappa_0\rangle$. Lines are drawn to guide the eye. The interparticle bond and spring constant analysis were conducted by Dr. M. Ganesan.

4.4 Discussion

Based on equation (4-1) and the analyses from Figure 4.4–4.6, within the experimental uncertainties, the predicted power law exponent, $\Pi_{\text{predict}} = (1+\beta)/(3-d_f)$ = 3.51 ± 0.13, 3.01 ± 0. 23, 2.90 ± 0.31 and 2.70 ± 0.45 for r = 1.00, 0.40, 0.20 and 0.09 is statistically similar with the values from Figure 4.3 ($p > 0.05$). Setting the corresponding modulus proportionality constant to f = 1.20 ± 0.14, 2.91 ± 0.60, 8.60 ± 1.10 and 18.42 ± 2.60 yields elastic modulus curves that are in good agreement with the measured values. Therefore, the efficient generation of elasticity in discoid gels and shifts in their power-law rheology are well predicted by the theory of Shih et al through shape induced changes to gel microstructure.

Intriguingly, f increases with discoid anisotropy. In the context of gel design, the r dependence of f and its magnitude points to an undetermined variable for controlling gel elasticity. While these f numbers are within the range reported in literature (see description of equation (4-1)), factors that mediate them have not been explored. Postulates include effect of polydispersity in particle size[161], contribution from pre-factor in cluster size scaling[124,183] and anisotropy in pair interactions[182] on bond strength and effective particle size. Future work exploring these postulated could reveal hidden variables for controlling gel elasticity.

In summary, this study demonstrates the potential of shape anisotropic particles for expanded elasticity control made possible by microstructural engineering that deviates from the universal descriptors of spinodal gelation.

4.5 Methods

4.5.1 Colloidal particles

Particles used in this study are polystyrene (PS) colloids. Fluorescently labeled carboxylate modified microspheres with diameter 0.98 ± 0.02 μm (F8821 FluoSpheres, Thermo Fisher Scientific) were used for confocal microscopy experiments. Rheology experiments were performed using non-fluorescent, sulfate modified latex particles with diameter 1.00 ± 0.02 μm (S37498, Invitrogen). The particle diameters were computed from scanning electron microscopy (SEM) images (TESCAN RISE, Michigan Center for Materials Characterization).

4.5.2 Thermomechanical squeezing of PS spheres

Colloidal discoids are generated by uniaxial compression of precursor PS spheres. Both the fluorescent and non-fluorescent precursor spheres are subjected to the same treatment. The method is adapted from Ahn et al[184] and Hsiao et al[182]. The stock PS particles are thrice washed

in de-ionized water and gently mixed with 10 wt% polyvinyl alcohol (PVA, molecular weight = 30 – 70 kDa, Sigma Aldrich) solution prepared in DI water. The choice of PVA and its concentration is based on our prior work[24,55]. The mixture is then poured onto 35 mm petri dishes (Thermo Scientific) and allowed to dry for 24 hours at 25°C on a precision leveling platform (TrippNT). After the edges are trimmed, the dried PVA films with embedded spheres are sandwiched between silicone rubber sheets (50A durometer, 0.5mm thick, McMaster Carr) and placed in between two 6" x 6" stainless steel panels (1 mm thick, McMaster Carr). See Figure S1 for the stack arrangement. The composite is then placed between heated platens of a bench-top press (Carver, Inc.) at 120°C (above the glass transition temperature of polystyrene, 90°C). The residence time is set to be 20 minutes for the films to reach the setpoint temperature (determined using a thermocouple thermometer, Fisher Scientific). A uniaxial compression is then applied to deform the film in which the spheres are embedded (Figure S1). The force is held for 20 min, following which the heat is turned off. The pressed films are allowed to cool under pressure to room temperature. The forces applied in this study are 750, 2800, 4200 kPa.

4.5.3 Retrieving colloidal discoids

Discoids are retrieved from the pressed PVA films following the procedure of Madivala et al[185]. The same procedure is followed for discoids prepared for both microscopy and rheology experiments. The PS-PVA films are dissolved in a 7:3 mixture of deionized water – isopropanol at 35°C for twelve hours with vigorous stirring[186]. The solution is then heated to 60°C for 30 min to dissolve the PVA completely. The solution is centrifuged, and the recovered particles are thrice washed in the same solvent. The particles are then dispersed in deionized water and heated to 60°C for 30 min with vigorous stirring to dissolve any final traces of PVA. Finally, the particles are thrice washed in DI water. The concentration of particles is measured using a

hemocytometer (NanoEnTek Inc.). The zeta potential measurements for the discoids average to -45.3 ± 3 mV, indicating a stable suspension, similar to the seed spheres, whose zeta potential is -48.5 ± 1.8 mV (Zetasizer Nano ZSP, Malvern Instruments). Aspect ratio, *r*, and discoid major axis *2A* are measured from images acquired by SEM of dilute samples in which discoids lie flat on the substrate. The minor axis *2B* is then obtained from conservation of volume of the seed sphere as per Hsiao et al[182].

4.5.4 Gelation of colloidal particles for microscopy and rheology

For gelation studies, the particles are redispersed in a buoyancy-matching mixture of deuterium oxide (151882, Sigma-Aldrich) and deionized water (resistance 18.2 MΩ, using Thermo Scientific DI Purifier) to prevent sedimentation effects [144,158]. Colloidal gels are assembled by the addition of $MgCl_2$ (68475, Sigma-Aldrich), which initiates aggregation. We follow the 50-50 mixing rule where equal parts of particles in H_2O-D_2O are mixed with equal parts of $MgCl_2$ solution to yield a final solution of desired particle volume fraction and [$MgCl_2$] = 10mM.

4.5.5 Confocal microscopy of colloidal gels

An inverted confocal laser scanning microscope (CLSM) (Nikon A1Rsi, equipped with NA = 1.4, 100x objective, oil-immersion type) is used to image the 3D microstructures of the gels self-assembled from fluorescently labeled particles. After the addition of $MgCl_2$ solution, the suspension is briefly and gently mixed for homogeneity and loaded into a 16-well chambered coverglass (Grace Bio-Labs, CultureWell, ChamberSLIP 16) mounted on the microscope stage above the objective. The chamber was closed to prevent evaporation. The gels form quiescently for 60 minutes before imaging. For visualization and microstructure characterization, 3D image volumes of size 512 x 512 pixels with pixel size 0.083 μm were acquired beginning at the

coverslip. The image stacks comprised of ~ 200 slices spaced at 0.083μm (acquired using Nikon AI Piezo z-drive). While acquiring image volumes, the intensity gain was gradually increased in the z-direction in steps of 1 unit for every 0.5μm to compensate for the loss of image intensity at depths greater than 8 μm due to the refractive index mismatch between polystyrene particles and H_2O-D_2O solution. CLSM visualization of the purified discoids are observed to be free of self-aggregation prior to the start of gelation.

4.5.6 Box-counting image analysis to compute fractal dimension

The fractal dimension, d_f, of gel networks are computed from confocal micrographs using the box counting method implemented as a custom MATLAB program[162,163]. Raw CLSM images are subjected to a thresholding filter of value S to distinguish foreground and background pixels. Segmented image volumes are then divided into cubes of dimension L x L x L (pixel^3) (c.f. Figure 4.4(a))[165]. The value of L is systemically varied from L = 2 pixels to L = 64 pixels. At each step, the number of cubes ($N(L)$) needed to cover all the foreground pixels corresponding to the gel is counted. Gel d_f is then obtained from the power-law fit $N(L) = c_1(I/L)^{d_f}$. Here, I is the image size (in pixels).

To address the S dependence inherent to this method, we apply the criteria of Thill and co-workers[163]. First, we vary S from 0 – 255 and plot d_f versus S as shown in Figure 4.9. The optimal threshold – where d_f does not change significantly – is identified by fitting the data to a third order polynomial and identifying the point where the concavity of the curve is zero. The optimal threshold was then used to compute the d_f values reported in Figure 4.4. This analysis accounts for any differences in instrument settings for image acquisition used due to batch-to-batch variation in particle fluorescence intensities.

To test the fidelity of this method, a complementary approach to identify the optimal threshold was followed. First, the d_f of sphere gels was determined from their radial distribution function, g(r_0) [158,187]. Here, g(r_0) is computed from particle centroids using tools available in TRACKPY[188] and FREUD[189] Python libraries. g(r_0) describes the average number of particles at a distance r_0 from a basis particle, relative to that of an ideal gas. For fractal structures, $g(r_0) \sim r_0^{d_f-3}$ for $r_0/2A > 3$ [180]. Following this equation, the fractal dimension is obtained from the slope of the log-log plot of g(r_0) data. This method yields $d_f = 1.89 \pm 0.04$ for sphere gels. Second, this value is matched with Figure 4.9 to find the threshold at which the d_f values for sphere gels match. A value of S = 137.5 is identified. The d_f for all the discoid gels were then computed at this threshold value.

4.5.7 Rheological characterization of colloidal gels

Rheological measurements are performed with a stress-controlled DHR-3 rheometer (TA Instruments) using a 40 mm stainless steel parallel plate geometry and a Peltier temperature-controlled plate (TA Instruments). Roughness 600 grit sandpaper (Part # 47185A51, McMaster Carr) was attached to both the top and bottom geometry surface to prevent wall slip[190,191]. The sample gap was set to be 500 μm. The temperature for all the rheology measurements is set to 20°C. Suspensions were loaded onto the Peltier plate, the top geometry was lowered and particles were allowed to quiescently assemble at the measurement gap for a gelation time of 45 minutes. An insulated solvent trap cover (TA Instruments) was used to prevent evaporation. Gel rheology was then measured by performing oscillatory strain amplitude sweeps ranging from $\gamma = 10^{-4}$ to 10^{-1} at a constant frequency of 1 rad/s.

We checked that the above choice of sandpaper and gap addressed any potential wall slip and confinement effects by performing measurements for sphere gels using different roughness

sandpapers and geometry gaps. Instrument sensitivity limits on the strains sweep plots (Figure 4.2) were determined by performing experiments with PEO (molecular weight ~ 1 x 10^6 g/mol, Sigma Aldrich) solutions at 2.0, 2.5, 3.0 and 4.0 wt% to determine the lower stress limits of the rheometer.

4.6 Supplementary Information

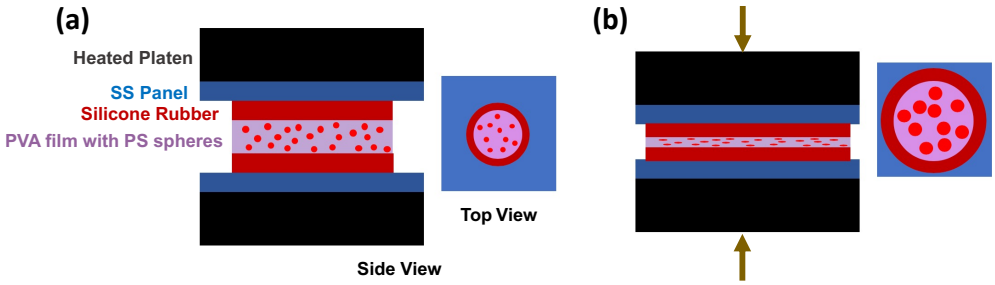

Figure 4.7 Thermo-mechanical squeezing of colloidal spheres for fabricating colloidal discoids (a) before applying uniaxial forces (b) after applying uniaxial forces.

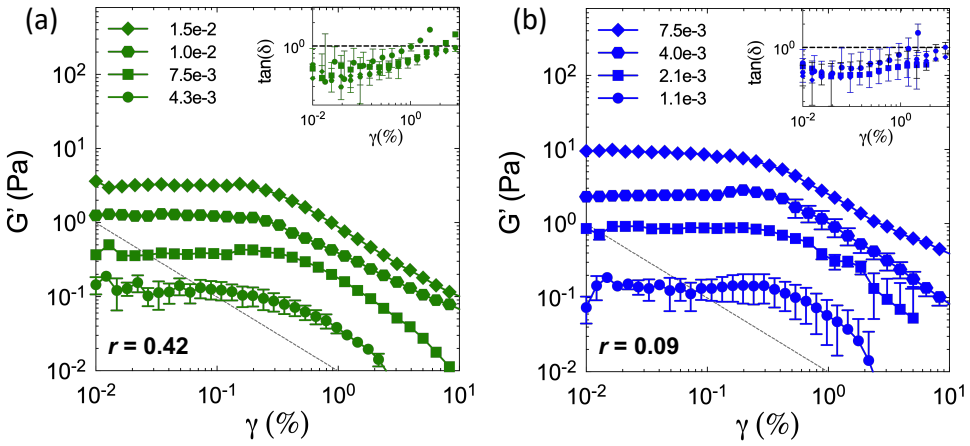

Figure 4.8 Storage modulus (G') and (inset) tan(δ) as a function of strain amplitude, γ at ω = 1 rad/s of colloidal gels made from (a) discoids (r = 0.42) and (b) discoids (r = 0.09). Dotted line indicates the instrument sensitivity limits (c.f. Methods).

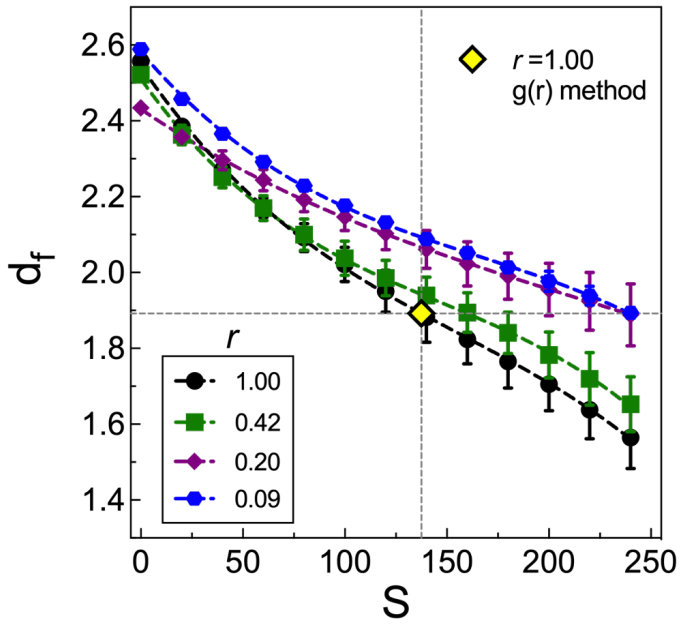

Figure 4.9 The effect of CLSM image thresholds, S, on the calculated fractal dimension values.

Chapter 5 Conclusions and Future Work

In this dissertation, we explored the connection between the microscopic structures and macroscopic optical properties for colloidal crystals and rheological properties for colloidal gels.

In Chapter 2, we investigated how to overcome one important engineering challenge in self-assembly: to control conditions to rapidly produce high quality crystal structures. We examined, with single-particle resolution, how could annealing strategies that popular for metals, polymers and protein crystal treatment might be extended to systems of colloidal particles. The extension yields both new fundamental understandings of how annealing is correlated with melting dynamics as well as the identification of useful heuristics that can be easily applied to improve the crystal quality of colloidal self-assembly, thereby yielding better control of the functional properties of colloidal systems.

There is a dearth of simple and efficient strategies for optimization and acceleration of the annealing process, especially ones that do not require detailed mapping of the system's energy landscape[48]. We produced such a simple annealing strategy and optimized its effectiveness by applying a cyclic external electric waveform of variable duty cycle to colloidal polystyrene monolayer films. This cyclic field is characterized by its amplitude, on-duration (t_{on}) for crystallization, and off-duration (t_{off}) for melting. We found a fundamental relationship between the local defects rearrangements timescale during melting and the optimal cyclic external field condition which best accelerates the crystal annealing. We used confocal microscopy, small-angle light scattering and molecular dynamics simulation to characterize

crystal ordering at both short-range and long-range, multigrain distances. We found that the optimal annealing duty cycle results in over 200% improvement of light-scattering peak intensity in as little as 15 cycles times with approximately two minutes per cycle.

We studied how local defect rearrangements promote the merging and reorientation of crystal grains into one long-range defect-free crystal. We found that the relationship between the melting timescale and the optimal t_{off} is insensitive to the details of particle interaction, suggesting the existence of a general principle for the annealing of colloidal monolayers.

Our findings contribute to the mechanistic understanding of how local defect rearrangements occur in external-field-driven colloidal crystal annealing. We demonstrate a novel annealing strategy that could be easily extended to other types of systems at different length and time scales. Functional materials comprised of colloidal particles that are required for applications such as sensing, structural color display and bioinspired camouflage materials can now be assembled into high quality crystals and rapidly reconfigured in time and space. In the future, this project can be extended to study the annealing of colloidal crystals assembled by anisotropic building blocks. For example, one could design a rotating external electric field to foster the annealing of anisotropic shape colloids due to particles rotational degree of freedom. One could study the motion of defects and defects recombination with anisotropic building blocks. In addition, future work could also examine the strategies to eliminate those dominant electric-field-direction-aligned defects in a coplanar device setup.

In Chapter 3, we compared the reconfigurable colloidal assembly between spheres and ellipsoids. Reconfigurable colloidal assembly concerns switchable transitions between phases, lattice spacings, and assembled configurations. Previous studies addressed the different tools available to achieve colloidal assembly reconfiguration and function[3]. Much work has addressed

the kinetics of colloidal assembly; however, less work has studied the effects of shape anisotropy on reconfiguration kinetics.

By SALS, we observed that particle shape has a strong effect on the melting kinetics of the ordered phases; ellipsoids with aspect ratio 2.0 melt into disordered structures 5.7 times faster than spherical colloids. Molecular dynamics simulation results further established that the enhanced melting is linked to the dynamical availability of rotational degrees of freedom for the ellipsoids. This work contributes to the understanding of reconfigurable kinetics and optical properties of colloidal crystals produced from anisotropic colloids. Understanding of the dynamics of colloidal ordering can be usefully applied in areas such as reconfigurable structural color. Future work could examine the crystallization and melting kinetics of ellipsoids with different aspect ratio. In addition, one could discuss the hydrodynamics effects in the system and how would that impact particles with different aspect ratio.

In Chapter 4, we explored new opportunities available to design sustainable gels formulation based on anisotropic colloids. We developed robust synthesis methods (thermomechanical squeezing and solvent retrieving) for manufacturing shape anisotropic colloidal discoids starting from spherical seed particles. We first demonstrated that elasticity of colloidal gels generated from colloidal discoids exhibit different power law dependency on particle loading where the exponent depends on building block aspect ratio. We then showed that gels formulated from discoids exhibit expanded elasticity states that are shifted relative to the universal behavior of sphere gels by a factor of as much as 15.

We applied the well-known predictive model[123] of colloidal gelation and explain this efficient generation of elasticity as a series of multiplicative factors dependent on the network fractal dimension d_f, the backbone topology d_B, and the existence of non-central pair forces. We

collected independent gels structural parameters by confocal microscopy and image analysis. The shifts in their power-law rheology are well predicted by the theory through shape induced changes to gel microstructure. In the future, this work could be extended to focus on the relationship between microstructures and the efficient generation of elasticity in discoid gels. Specifically, in the Shih et al theory, gel elasticity is controlled by the cluster size, R which is given by the equation $N_p = k_f\left(R/V_p^{1/3}\right)^{d_f}$. N_p is the number of particles in the cluster. Here, the pre-factor, k_f describing the absolute value of R is taken to be on the order of unity and not included further. However, studies on non-spherical soot aggregates[131] report k_f values that deviate from ideal spheres. Therefore, any *r* induced changes to k_f and consequential impacts on R are unaccounted for in equation (4-1). To remediate this, it is important to design a colloidal system with image analysis algorithms that capable of identifying number of anisotropic particles in each cluster of the system. In addition, one could study the particles with ellipsoidal shape and study how the microstructures related to their rheology responses, as a complement to the current study, which is limited to the discoidal particle shape. Economic analysis for the manufacturing process could be helpful to understand the practical sustainability application.

In this dissertation, our research results show that the macroscopic functional properties of colloidal crystals and gels can be tuned by engineering their microstructures. We demonstrate through cyclic toggling of external fields and modulation of particle shape anisotropy the realization of defect free high quality colloidal crystals and ultra-efficient colloidal gels with expanded elasticity states. These are made possible by coupling the applied field and assembly conditions to fundamental time scales and pair potentials of the constituent particles. Our studies reveal new directions for designing colloidal structures with tailored features that are useful in applications ranging from displays and coatings to consumer and pharmaceutical products.

Appendices

Here in the appendices are computational codes for image analysis used in this dissertation.

A. Psi 6 analysis of spheres assembly (Python)

```
[window 1]
import freud
import pandas
import numpy as np
import matplotlib.pyplot as plt
% matplotlib inline

import matplotlib.colors as colors
import matplotlib.cm as cmx

[window 2]
c_1 = pandas.read_excel('/Users/pkkao/I_second_1.xlsx')
c_1_np = np.array(c_1)

c_19 = pandas.read_excel('cycle_19.xlsx')
c_19_np = np.array(c_19)

[window 3]
for data, name in zip([c_1_np, c_19_np],['cycle_1', 'cycle_19']):
    Lx = 1.1*(np.amax(data[:,0]) - np.amin(data[:,0]))
    Ly = 1.1*(np.amax(data[:,1]) - np.amin(data[:,1]))
    Lz = 100

    B0 = data.mean(axis=0)

    positions = np.copy(data)
    positions = positions - B0
    positions[:,2] = 0

    edge_buffer = 5*data[:,2].mean()

    cond = ((positions[:,0]-np.amax(positions[:,0])+edge_buffer<0)*
           (positions[:,0]+np.amax(positions[:,0])-edge_buffer>0)*
           (positions[:,1]-np.amax(positions[:,1])+edge_buffer<0)*
           (positions[:,1]+np.amax(positions[:,1])-edge_buffer>0))

    fbox = freud.box.Box(Lx=Lx,Ly=Ly,Lz=Lz)
    psi = freud.order.HexOrderParameter(rmax=edge_buffer, k=6, n=6)
    psi.compute(fbox, positions)

    psi_6 = np.real(np.copy(psi.psi)*np.conj(np.copy(psi.psi)))

    del(psi)

    psi = freud.order.HexOrderParameter(rmax=edge_buffer, k=2, n=2)
```

```
    psi.compute(fbox, positions)

    psi_2 = np.real(np.copy(psi.psi)*np.conj(np.copy(psi.psi)))

    cm = plt.get_cmap('viridis')
    cNorm  = colors.Normalize(vmin=0, vmax=1)
    scalarMap = cmx.ScalarMappable(norm=cNorm, cmap=cm)

    fig = plt.figure(figsize=(8,8))
    ax = fig.add_subplot(221)
    ax.scatter(positions[:,0], positions[:,1], s=0.5, c='b')
    ax.scatter(positions[cond,0], positions[cond,1], s=20,
c=scalarMap.to_rgba(psi_6[cond]))

ax.set_title(r'$\langle\psi_6\rangle={p:.2f}\pm{pp:.2f}$'.format(p=psi_6[c
ond].mean(),

pp=psi_6[cond].std()), fontsize=20)
    ax.axis('off')


    ax = fig.add_subplot(222)
    ax.scatter(positions[:,0], positions[:,1], s=0.5, c='b')
    ax.scatter(positions[cond,0], positions[cond,1], s=20,
c=scalarMap.to_rgba(psi_2[cond]))

ax.set_title(r'$\langle\psi_2\rangle={p:.2f}\pm{pp:.2f}$'.format(p=psi_2[c
ond].mean(),

pp=psi_2[cond].std()), fontsize=20)
    ax.axis('off')

    ax = fig.add_subplot(223)
    hist, bins = np.histogram(psi_6[cond], bins=100)
    ax.set_ylabel(r'$N$', fontsize=16)
    ax.set_xlabel(r'$\psi_6$', fontsize=16)
    ax.xaxis.set_tick_params(labelsize=14)
    ax.yaxis.set_tick_params(labelsize=14)
    ax.plot(bins[0:-1]+(bins[1]-bins[0])/2, hist)

    ax = fig.add_subplot(224)
    hist, bins = np.histogram(psi_2[cond], bins=100)
    ax.set_ylabel(r'$N$', fontsize=16)
    ax.set_xlabel(r'$\psi_2$', fontsize=16)
    ax.xaxis.set_tick_params(labelsize=14)
    ax.yaxis.set_tick_params(labelsize=14)
    ax.plot(bins[0:-1]+(bins[1]-bins[0])/2, hist)


    plt.tight_layout()
    fig.savefig('{n}.png'.format(n=name), dpi=300)
```

B. Nearest neighbors and nearest neighboring angles distribution: ellipsoids (Matlab)

```
clc
clear all;
close all;
```

```
 XRemovePixela=140;              %%%%%%%%%%%%%%%%%%%%RightLimitX
 YRemovePixela=25;               %%%%%%%%%%%%%%%%%%%%UpperLimitY
 XRemovePixelb=20;               %%%%%%%%%%%%%%%%%%%%LeftLimitX
 YRemovePixelb=80;              %%%%%%%%%%%%%%%%%%%%LowerLimitY



I = imread('cp_2.png'); %reads the image and stores it as a 3-D uint8
variable
imshow(I);
Enh=adapthisteq(I(:,:,1),'Cliplimit',0.9);
%%%%%%%%%%%%%%%%%%%%%%%%%%%%%%%%%%%%%%%%%%%%%%%%%%%%
% enhance the contrast of the greyscale image I
% contrast enhancement limit, specified as a real scalar in the range
[0,1]
% Higher limits result in more contrast
imshow(Enh)

BW=imbinarize(Enh,0.5);
%%%%%%%%%%%%%%%%%%%%%%%%%%%%%%%%%%%%%%%%%%
imshow(BW)
imshow(I);hold on

stats =
regionprops(BW,'Orientation','Centroid','MajorAxisLength','MinorAxisLen
gth','Eccentricity');

%Parametric equation of bounding ellipse
phi = linspace(0,2*pi,100);
cosphi = cos(phi);
sinphi = sin(phi);

kk=0;
for k = 1:length(stats);
    if  stats(k).MajorAxisLength > 7 && stats(k).MajorAxisLength < 50
%%%%%%%%%%%%%%%%%%%%%%%%%%%%%%%%%%%%%%%%%%%%%%%%%%%%

        kk=kk+1;

        %MajorAxisLength arbitrarily set to 14.
        %Play around with this number to identify more particles
        xbar = stats(k).Centroid(1);
        ybar = stats(k).Centroid(2);
        a = stats(k).MajorAxisLength/2;
        b = stats(k).MinorAxisLength/2;
        theta = pi*stats(k).Orientation/180;

        R = [ cos(theta)   sin(theta)
        -sin(theta)   cos(theta)];
        xy = [a*cosphi; b*sinphi];
        xy = R*xy;
        x(:,1) = xy(1,:) + xbar;
        y(:,1) = xy(2,:) + ybar;

        %Major Axis
        xmaj2=xbar-a*cos(pi-theta);
        ymaj2=ybar-a*sin(pi-theta);
```

```
        xmaj1=xbar+a*cos(pi-theta);
        ymaj1=ybar+a*sin(pi-theta);

        %Minor Axis
        xmin2=xbar-b*sin(pi-theta);
        ymin2=ybar+b*cos(pi-theta);
        xmin1=xbar+b*sin(pi-theta);
        ymin1=ybar-b*cos(pi-theta);


        %Line for Major Axis
            for i=1:length(x)
                ymajorline(i,1)=(x(i,1)-xmaj1)/(xmaj2-xmaj1)*(ymaj2-
ymaj1)+ymaj1;
            end

        %Line for Minor Axis
            for i=1:length(x)
                yminorline(i,1)=(x(i,1)-xmin1)/(xmin2-xmin1)*(ymin2-
ymin1)+ymin1;
            end

        %Storing the data
        data(:,1,kk)=x(:,1); %x-coordinate for ellipse kk
        data(:,2,kk)=y(:,1); %y-coordinate for ellipse kk
        data(:,3,kk)=ymajorline(:,1); %y-coordinate for major axis of
ellipse kk
        data(:,4,kk)=atand(ymajorline(length(ymajorline),1)-
ybar)/(x(length(x),1)-xbar); %slope of major axis of ellipse kk
        data(:,5,kk)=stats(k).Orientation; %Orientation of the ellipse
        data(:,6,kk)=xbar;   % store the x centroids
        data(:,7,kk)=ybar;   % store the y centroids


        %Plotting of ellipse boundary and major axis
        plot(x,y,'w','LineWidth',3);hold on;
        plot(xbar,ybar,'o','MarkerFaceColor','b');hold on;
       %
plot(xmaj2,ymaj2,'o','MarkerFaceColor','g','MarkerSize',4);hold on;
       %
plot(xmaj1,ymaj1,'o','MarkerFaceColor','g','MarkerSize',4);hold on;
       %
plot(xmin2,ymin2,'o','MarkerFaceColor','g','MarkerSize',4);hold on;
       %
plot(xmin1,ymin1,'o','MarkerFaceColor','g','MarkerSize',4);hold on;

    end
end

%create a giant matrix
             grow=kk;  % row is total number of particles
             gcolu=12; % column in a big number
%%%%% check if Nearest number is larger than this number
             Angl=zeros(grow,gcolu);

 %for each particle, start to draw a big cut_off ellipse
 %effectively, we have 'kk' particles in the image
     for m=1:kk
```

```
     xcent(m)=data(1,6,m);
     ycent(m)=data(1,7,m);
      m=m+1;
     end

     % each particle centroids in xbarnew and ybarnew
     % cut_off ratio
     Cr=3.5;
%%%%%%%%%%%%%%%

     for j=1:kk
     xbarnew(j)=data(1,6,j);
     ybarnew(j)=data(1,7,j);
        for i=1:100
            %each slope=ES
            %distance=d
            ES(i,j)=(data(i,2,j)-ybarnew(j))./(data(i,1,j)-xbarnew(j));
            d(i,j)=sqrt((data(i,1,j)-xbarnew(j)).^2+(data(i,2,j)-
ybarnew(j)).^2);
            %vectors
            vx(i,j)=data(i,1,j)-xbarnew(j);
            vy(i,j)=data(i,2,j)-ybarnew(j);
            ux(i,j)=vx(i,j)./d(i,j);
            uy(i,j)=vy(i,j)./d(i,j);
            xcut(i,j)=xbarnew(j)+Cr.*d(i,j).*ux(i,j);
            ycut(i,j)=ybarnew(j)+Cr.*d(i,j).*uy(i,j);

            i=i+1;

        end

            %in =   inpolygon(xq,yq,xv,yv) returns in indicating if the
query points
            %       specified by xq and yq are inside or on the edge of
the polygon area
            %       defined by xv and yv.
            in=inpolygon(xcent,ycent,xcut(:,j),ycut(:,j));
            N_withCent(j)=numel(xcent(in),ycent(in));
            N(j)=N_withCent(j)-1;

   %%%%%%%%%%        find the center of each cut region

            Xz=xcent(in);Yz=ycent(in);
            zz=size(Xz);
            czz=zz(1,2);
            MXz=mean(Xz); MYz=mean(Yz);
            ComDis=[];

            for lol=1:czz
                 ComDis(1,lol)= sqrt((MXz(1)-Xz(lol)).^2+(MYz(1)-
Yz(lol)).^2);
                 lol=lol+1;

            end


            minI=find(ComDis==min(ComDis));
```

```
            if size(minI)==2   % if only two points in the cut_off
region
                N(j)=1;
                %xccut=mean(Xz(minI));
                %yccut=mean(Yz(minI));
            else

                xccut=Xz(minI); % position of the center among the cut
off region (x)
                yccut=Yz(minI); % position of the center among the cut
off region (y)
            end
             %%%%%%%forming vectors%%%%%%%%

             ru=[];
             for cr=1:czz
                 ru(cr,1)=Xz(cr)-xccut(1);
                 ru(cr,2)=Yz(cr)-yccut(1);
             end
             %ru
             new_ru=ru;
             for cr1=1:czz
                    if ru(cr1,:)==0
                    new_ru(cr1,:)=[];
                    end
             end


             cLine=czz-1;  % how many points around the center
             cCount=cLine-1;
             cll=2;


             %new_ru: vectors around the center
             %plot vector in each center point%

%             for itt=1:cLine
%             x1=xccut+new_ru(itt,1);
%             y1=yccut+new_ru(itt,2);
%             itt=itt+1;
%             plot([xccut,x1],[yccut,y1],'w','LineWidth',1.5 );hold on;
%
%              end

% ref vector(1,0) find the angles around the center

             if cLine==0
              Angl(j,1)=0;
             else
                 refv=[1,0];
                 Deg=[];
                 for s=1:cLine
                   MagS(s)=sqrt(new_ru(s,1).^2+new_ru(s,2).^2);
                   Deg(s)=acosd(dot(refv,new_ru(s,:))./(1.*MagS(s)));
                    if new_ru(s,2)<0
                       Deg(s) =360-Deg(s);
                    end
```

```
                  s=s+1;
                end
                BB=sort(Deg);

                for ss=1:cCount
                    Angl(j,ss)=BB(ss+1)-BB(ss);
                    ss=ss+1;
                end
                for ss=cLine
                    Angl(j,ss)=360-BB(cLine)+BB(1);
                end

             end


            j=j+1;
     end

       % plot the cut_off ellipse  %

%plot(xcut(:,100),ycut(:,100),'o','MarkerFaceColor','g','MarkerSize',4)
;hold on;

     % Remove edge particels
     Summ=sum(N);
     CC=numel(N);
     NoutSum=0;
     NoutCount=0;
     Posi=[xcent;ycent ;N]';
       for jj=1:kk
           %%% if (the peripheral region)
           if Posi(jj,1)>XRemovePixela || Posi(jj,2)<YRemovePixela ||
Posi(jj,1)<XRemovePixelb || Posi(jj,2)>YRemovePixelb
               NoutSum=NoutSum+Posi(jj,3);
               NoutCount=NoutCount+1;

           end

           jj=jj+1;
       end

       %%%%%remove edge particles for degree calculation%%%%%%%%%

      PosiAn=[xcent;ycent]';
      Ang=cat(2,PosiAn,Angl);
      for aa=1:kk
          %%% if (the peripheral region)
           if Ang(aa,1)>XRemovePixela || Ang(aa,2)<YRemovePixela ||
Ang(aa,1)<XRemovePixelb || Ang(aa,2)>YRemovePixelb
              Ang(aa,:)=0;

           end

           aa=aa+1;

      end

      Ang( ~any(Ang,2), : ) = [];  %removes all rows with all zero
```

```
        Ang2=Ang;
        Ang2(:,[1,2])=[];
        tot=size(Ang,1)*12;
           Ang3=reshape(Ang2,[tot,1]);
           Angd=Ang3(Ang3~=0);


         %%%%%
         % Plot Nearest Angles
         %%%%%
         Angd=sort(Angd);
         ad=figure;
         histogram(Angd,25)
%%%%%%%%%%%% how many bins are you going to divide
        title('Angles Distribution within Nearest
Neighbors','fontsize',22);
        h.FontSize=16;
        xlabel('Angles(degree)','fontsize',16);
        ylabel('Count','fontsize',16);
         ylim([0 30])
         xlim([0 180])
         set(gca, 'XTick');
         set(gca, 'FontSize', 16)
        set(ad, 'Position', [0 0 650 428]);  % set the display window
size
        %%%%

       NInnerSum=Summ-NoutSum;
       Ncount=CC-NoutCount
       Navg=NInnerSum./Ncount
```

C. SALS analysis: spheres (Matlab)

SpheresIdentify.m

```
close all;
clear;
clc;
imshow('x1_-1.png')
[aa,yy]=getpts;
XY=[aa,yy];
```

CircleFitByPratt.m

```
function Par = CircleFitByPratt(XY)
n = size(XY,1);      % number of data points
centroid = mean(XY);   % the centroid of the data set

% computing moments (note: all moments will be normed, i.e. divided by n)

Mxx=0; Myy=0; Mxy=0; Mxz=0; Myz=0; Mzz=0;

for i=1:n
    Xi = XY(i,1) - centroid(1);  %  centering data
    Yi = XY(i,2) - centroid(2);  %  centering data
    Zi = Xi*Xi + Yi*Yi;
```

```
    Mxy = Mxy + Xi*Yi;
    Mxx = Mxx + Xi*Xi;
    Myy = Myy + Yi*Yi;
    Mxz = Mxz + Xi*Zi;
    Myz = Myz + Yi*Zi;
    Mzz = Mzz + Zi*Zi;
end

Mxx = Mxx/n;
Myy = Myy/n;
Mxy = Mxy/n;
Mxz = Mxz/n;
Myz = Myz/n;
Mzz = Mzz/n;

%    computing the coefficients of the characteristic polynomial

Mz = Mxx + Myy;
Cov_xy = Mxx*Myy - Mxy*Mxy;
Mxz2 = Mxz*Mxz;
Myz2 = Myz*Myz;

A2 = 4*Cov_xy - 3*Mz*Mz - Mzz;
A1 = Mzz*Mz + 4*Cov_xy*Mz - Mxz2 - Myz2 - Mz*Mz*Mz;
A0 = Mxz2*Myy + Myz2*Mxx - Mzz*Cov_xy - 2*Mxz*Myz*Mxy + Mz*Mz*Cov_xy;
A22 = A2 + A2;

epsilon=1e-12;
ynew=1e+20;
IterMax=20;
xnew = 0;

%    Newton's method starting at x=0

for iter=1:IterMax
    yold = ynew;
    ynew = A0 + xnew*(A1 + xnew*(A2 + 4.*xnew*xnew));
    if (abs(ynew)>abs(yold))
        disp('Newton-Pratt goes wrong direction: |ynew| > |yold|');
        xnew = 0;
        break;
    end
    Dy = A1 + xnew*(A22 + 16*xnew*xnew);
    xold = xnew;
    xnew = xold - ynew/Dy;
    if (abs((xnew-xold)/xnew) < epsilon), break, end
    if (iter >= IterMax)
        disp('Newton-Pratt will not converge');
        xnew = 0;
    end
    if (xnew<0.)
        fprintf(1,'Newton-Pratt negative root:  x=%f\n',xnew);
        xnew = 0;
    end
end

%    computing the circle parameters
```

```
DET = xnew*xnew - xnew*Mz + Cov_xy;
Center = [Mxz*(Myy-xnew)-Myz*Mxy , Myz*(Mxx-xnew)-Mxz*Mxy]/DET/2;

Par = [Center+centroid , sqrt(Center*Center'+Mz+2*xnew)];

end    %    CircleFitByPratt
```

PlotCircle.m

```
clear all
close all;

I0empty=zeros(2192,2728);
srcFiles = dir('/Users/pkkao/UM/UM_LAB/Annealing
SALS/Codes_spheres/x3_1_*.png') %%%%%%%%%%%%%%%

jk=length(srcFiles)

for i = 1 : jk

    filename = strcat('/Users/pkkao/UM/UM_LAB/Annealing
SALS/Codes_spheres/',srcFiles(i).name);
    Iss= imread(filename);
    J=imrotate(Iss,0,'crop');

      Id=double(J);
      I0empty=Id;
end

GP=I0empty./1; %%%%%     how many images are for the average

I = imread('x3_1_1.png'); %reads the image
imshow(I); hold on;

x=1.35e+03;    %%%%
y=1.08e+03;    %%%%
rp=0.29e+03;      %%%%
rm=rp;              %%%%

kk=1200; %how many points along 0-2pi
kkm=kk;
j=1;
k=1;
km=1;

pp=10; % how many pixels you want to look at (band)
pp2=2*pp;

th = 0:pi/600:2*pi;

%outer circle
for j=1:pp
    rp=rp+j/2;
    for k=1:kk
        xunit(j,k) = rp* cos(th(k)) + x;
```

```
        yunit(j,k) = rp* sin(th(k)) + y;
        k=k+1;
    end
 j=j+1;
end

%inner circle
for z=1:pp
    rm=rm-z/2;
    for km=1:kkm
        xunitm(z,km) = rm* cos(th(km)) + x;
        yunitm(z,km) = rm* sin(th(km)) + y;
        km=km+1;
    end
 z=z+1;
end

plot(xunit, yunit,'w','LineWidth',2);hold on;
plot(xunitm,yunitm,'y','LineWidth',2);hold on;
Xunit=[xunit;xunitm];
Yunit=[yunit;yunitm];
XPos=Xunit';
YPos=Yunit';
XPosR=round(XPos);
YPosR=round(YPos);

% get the intensity
for jj=1:pp2
  for rr=1:kk             %%%% how many pointws are devided %%%
 IntensPos(rr,jj)=GP(YPosR(rr,jj),XPosR(rr,jj));  %%%    GP(y,x)
 rr=rr+1;
  end
 jj=jj+1;

end
Rth=th';
Iavg=mean(IntensPos,2);
Isum=sum(IntensPos,2);

Rth( ~any(Rth,2), : ) = [];    %%%%% Remove the first 0 element in the
matrix
IntScat=figure;
plot(Rth,Isum,'o','MarkerFaceColor','b','MarkerSize',4);hold on;

GPts=getpts;
PCenter=(GPts(1)/pi*180+(GPts(2)/pi*180-60)+(GPts(3)/pi*180-
60*2)+(GPts(4)/pi*180-60*3)+(GPts(5)/pi*180-60*4)+(GPts(6)/pi*180-
60*5))./6;
ShiftPeak=30-PCenter   %%% unit: degree
```

GFitting_S.m

```
cenS=ShiftPeak/(60/(kk/6));
movC=round(cenS);              %%%% how many pixels should move (max: kk/6
= 200 pixels)
```

```
GFit=figure;

N=round(size(Rth,1)./6);
for i=1:N
I1245(i)=(Isum(i)+Isum(i+N)+Isum(i+3.*N)+Isum(i+4.*N))./pp2./4;
I36(i)=(Isum(i+2.*N)+Isum(i+5.*N))./pp2./2;
end

c=N-movC;

for ii=1:c

        Inew(ii+movC)=I1245(ii);
        Inew2(ii+movC)=I36(ii);

        ii=ii+1;
end

for ii=(c+1):N
    Inew(201-ii)=I1245(ii);
    Inew2(201-ii)=I36(ii);

    ii=ii+1;
end
for d=1:N
Deg(d)= (60/N).*d;
end

plot(Deg,Inew,'o','MarkerFaceColor','b','MarkerSize',4);hold on;
plot(Deg,Inew2,'o','MarkerFaceColor','r','MarkerSize',4);hold on;

smyy3 = smooth(Deg,Inew,10,'moving'); % 4 peaks
smyy4 = smooth(Deg,Inew2,10,'moving'); % 2 peaks

plot(Deg,Inew,'b.',Deg,smyy3,'b-','LineWidth',1.5)
plot(Deg,Inew2,'b.',Deg,smyy4,'r-','LineWidth',1.5)
```

function [ycorr,yfit] = bf(y,varargin)

```
def_method  = 'spline';
def_avgpts  = 3;

method = [];
avgpts = [];
pts    = [];
confirm = false;
for n = 2:nargin,
    f = varargin{n-1};
    if ischar(f),
        if strcmpi(f,'confirm'),
            confirm = true;
        else
            method = f;
        end
    elseif isnumeric(f) && numel(f) == 1,
        avgpts = f;
    elseif isnumeric(f) && numel(f) > 1,
```

```
        pts = f;
    elseif isempty(f),
        continue
    else
        error ('  Invalid input argument!')
    end
end
if isempty(method),     method = def_method;        end
if isempty(avgpts),     avgpts = def_avgpts;        end
dimy = size(y);
lst = dimy(1);
newdimy = [dimy(1),prod(dimy(2:end))];
y = reshape(y,newdimy);
x = 1:lst;
if isempty(pts),
    interactive = true;
else
    interactive = false;
end
if interactive || confirm,
    bffig = figure;
else
    bffig = 0;
end
ok = false;
while ~ok,
    if interactive,
        plot(x,real(y(:,1)))
        set(bffig,'Name','Baseline Fit - Select points')
        fprintf(['\n Now select baseline points to fit by positioning
cursor,',...
            '\n   and selecting points with mouse button or key
press.',...
            '\n Press Enter key when done.\n'])
        [a,b] = ginput;                                 %#ok
        pts = round(a.');
    end
    pts = sort(pts);
    pts(diff(pts)==0) = [];         % delete duplicate points
    if pts(1)~=1,       pts = [1,pts];          end     %#ok
    if pts(end)~=lst,   pts = [pts,lst];        end     %#ok
    npts = numel(pts);
    pss = zeros(npts,2);
    pss(:,1) = pts - floor(avgpts/2);
    pss(:,2) = pss(:,1) + avgpts;
    pss(pss < 1) = 1;
    pss(pss > lst) = lst;
    yavg = zeros([npts,newdimy(2)]);
    for n = 1:npts,
        yavg(n,:) = mean(y(pss(n,1):pss(n,2),:),1);
    end
    yfit = interp1(pts,yavg,x,method);
    if size(yfit,1) ==1,
        yfit = shiftdim(yfit,1);    % make yfit a column if it is a row
vector
    end
    if confirm,
        interactive = true;
```

```
        figure(bffig)

plot(x,real(y(:,1)),'b',x,real(yfit(:,1)),'r',pts,real(yavg(:,1)),'ob')
        set(bffig,'Name','Baseline Fit - Verify baseline')
        answer = input('  Do you to redo fit and reselect baseline
points?[N] ','s');
        if isempty(answer),     answer = 'n';   end
        if strcmpi(answer,'y'),
            ok = false;
        else
            ok = true;
        end
    else
        ok = true;
    end
end
if any(findobj('Type','figure')==bffig),
    close(bffig),                % close figure if it exists
end
ycorr = y - yfit;
ycorr = reshape(ycorr,dimy);
yfit = reshape(yfit,dimy);
```

Sint.m

```
%    InewM=mean(I1(81:110))


    DX1=1;         %%% change the range of DX1-DX2 to better fit the peak
    DX2=199;
    SD=Deg'; ID=I2;sV=-5;
    SD(1:DX1)=sV; SD(DX2:end)=sV;
    ID(1:DX1)=sV;ID(DX2:end)=sV;
    SD=SD(find(SD~=sV));
    ID=ID(find(ID~=sV));

%    ID=ID+3

    fD = fit(SD,ID,'gauss1')

   figure
   GFittingplot=plot(fD,SD,ID)
%%%%%%%%%%%%%%%%%%%%%%%%%%%%%%%%%%%%%%%%%%%%%%%%%%%%%%%%%%%%%%%%%%%%%%%%%%%


    set(GFittingplot,'LineWidth',2)

title('SALS Scattering Peaks Fitting ','fontsize',20);
       xlabel('Theta(degree)','fontsize',16);
       ylabel('Intensity(a.u.)','fontsize',16);
       set(gca,'XTick',(0:10:60));
       ylim([-10 250]);
       set(gca,'YTick',(0:50:120));
```

D. SALS analysis: ellipsoids (Matlab)

EllipsIntensity.m

```
clear;
clc;
close all;
X= imread('10__1.jpg');
J = imrotate(X,57.5,'crop');
imshow(J)
[aa,yy]=getpts;
A=[aa,yy];
z=-yy;
```

function ellipse_t = fit_ellipse(x,y,axis_handle)

```
% initialize
orientation_tolerance = 1e-3;

% empty warning stack
warning( '' );

% prepare vectors, must be column vectors
x = x(:);
y = y(:);

% remove bias of the ellipse - to make matrix inversion more accurate.
(will be added later on).
mean_x = mean(x);
mean_y = mean(y);
x = x-mean_x;
y = y-mean_y;

% the estimation for the conic equation of the ellipse
X = [x.^2, x.*y, y.^2, x, y ];
a = sum(X)/(X'*X);

% check for warnings
if ~isempty( lastwarn )
       disp( 'stopped because of a warning regarding matrix inversion' );
       ellipse_t = [];
       return
   end

   % extract parameters from the conic equation
   [a,b,c,d,e] = deal( a(1),a(2),a(3),a(4),a(5) );

   % remove the orientation from the ellipse
   if ( min(abs(b/a),abs(b/c)) > orientation_tolerance )

       orientation_rad = 1/2 * atan( b/(c-a) );
       cos_phi = cos( orientation_rad );
       sin_phi = sin( orientation_rad );
       [a,b,c,d,e] = deal(...
           a*cos_phi^2 - b*cos_phi*sin_phi + c*sin_phi^2,...
           0,...
           a*sin_phi^2 + b*cos_phi*sin_phi + c*cos_phi^2,...
           d*cos_phi - e*sin_phi,...
           d*sin_phi + e*cos_phi );
       [mean_x,mean_y] = deal( ...
```

```
        cos_phi*mean_x - sin_phi*mean_y,...
        sin_phi*mean_x + cos_phi*mean_y );
else
    orientation_rad = 0;
    cos_phi = cos( orientation_rad );
    sin_phi = sin( orientation_rad );
end

% check if conic equation represents an ellipse
test = a*c;
switch (1)
case (test>0),  status = '';
case (test==0), status = 'Parabola found';  warning( 'fit_ellipse: Did
not locate an ellipse' );
case (test<0),  status = 'Hyperbola found'; warning( 'fit_ellipse: Did
not locate an ellipse' );
end

% if we found an ellipse return it's data
if (test>0)

    % make sure coefficients are positive as required
    if (a<0), [a,c,d,e] = deal( -a,-c,-d,-e ); end

    % final ellipse parameters
    X0          = mean_x - d/2/a;
    Y0          = mean_y - e/2/c;
    F           = 1 + (d^2)/(4*a) + (e^2)/(4*c);
    [a,b]       = deal( sqrt( F/a ),sqrt( F/c ) );
    long_axis   = 2*max(a,b);
    short_axis  = 2*min(a,b);

    % rotate the axes backwards to find the center point of the
original TILTED ellipse
    R           = [ cos_phi sin_phi; -sin_phi cos_phi ];
    P_in        = R * [X0;Y0];
    X0_in       = P_in(1);
    Y0_in       = P_in(2);

    % pack ellipse into a structure
    ellipse_t = struct( ...
        'a',a,...
        'b',b,...
        'phi',orientation_rad,...
        'X0',X0,...
        'Y0',Y0,...
        'X0_in',X0_in,...
        'Y0_in',Y0_in,...
        'long_axis',long_axis,...
        'short_axis',short_axis,...
        'status','' );
else
    % report an empty structure
    ellipse_t = struct( ...
        'a',[],...
        'b',[],...
        'phi',[],...
```

```
        'X0',[],...
        'Y0',[],...
        'X0_in',[],...
        'Y0_in',[],...
        'long_axis',[],...
        'short_axis',[],...
        'status',status );
end

% check if we need to plot an ellipse with it's axes.
if (nargin>2) & ~isempty( axis_handle ) & (test>0)

    % rotation matrix to rotate the axes with respect to an angle phi
    R = [ cos_phi sin_phi; -sin_phi cos_phi ];

    % the axes
    ver_line        = [ [X0 X0]; Y0+b*[-1 1] ];
    horz_line       = [ X0+a*[-1 1]; [Y0 Y0] ];
    new_ver_line    = R*ver_line;
    new_horz_line   = R*horz_line;

    % the ellipse
    theta_r         = linspace(0,2*pi);
    ellipse_x_r     = X0 + a*cos( theta_r );
    ellipse_y_r     = Y0 + b*sin( theta_r );
    rotated_ellipse = R * [ellipse_x_r;ellipse_y_r];

    % draw
    hold_state = get( axis_handle,'NextPlot' );
    set( axis_handle,'NextPlot','add' );
    plot( new_ver_line(1,:),new_ver_line(2,:),'r' );
    plot( new_horz_line(1,:),new_horz_line(2,:),'r' );
    plot( rotated_ellipse(1,:),rotated_ellipse(2,:),'r' );
    set( axis_handle,'NextPlot',hold_state );
end
```

NewTrackEllipse.m

```
%close all;

I0empty=zeros(2192,2728);
srcFiles = dir('/Users/pkkao/UM/UM LAB/Annealing
SALS/Codes_ellipsoids/annealing_g_17-*.png');
for ilol = 1 : length(srcFiles)

    filename = strcat('/Users/pkkao/UM/UM LAB/Annealing
SALS/Codes_ellipsoids/',srcFiles(ilol).name);
    Iss= imread(filename);
    J=imrotate(Iss,61.5,'crop');

    Id=double(J);
    I0empty=Id+I0empty;
end

GP=I0empty./3;    %%%%%%%%%% how many frames

x0=1.3523e+03;                      %input, fitting ellipse parameters
```

```
y0=-1.1178e+03;
orien=0.50*pi;
a =584.4439/2;
b =486.4212/2;
n=200;                                  %input n points
vc1=n;
t = linspace(0,2*pi,n);
ju=15;                    %%%%%%%%%%
du=15;

 %middle ellipse
 x1=x0+a*cos(orien);
 x2=x0-a*cos(orien);
 y1=y0-a*sin(orien);
 y2=y0+a*sin(orien);
 X = a*cos(t);
 Y = b*sin(t);
 w = atan2(y2-y1,x2-x1);
 xmi = (x1+x2)/2 + X*cos(w) - Y*sin(w);
 ymi = (y1+y2)/2 + X*sin(w) + Y*cos(w);

 % calculating the degree of each point
 %%%%%% forming vectors, each point on the ellipse to the centroids
 %%%% the largest magnitude of the vector are the ends points
 v=[xmi-x0;ymi-y0];

 for vc=1:vc1
      vm(1,vc)=sqrt(v(1,vc).^2+v(2,vc).^2);
      vc=vc+1;                                    %%%%check v(3,:) if the
first one is the end point
 end


 for vd=1:vc1

vdeg(1,vd)=acosd(((v(1,vd).*v(1,1))+(v(2,vd).*v(2,1))./(vm(1,1).*vm(1,
vd)));
     vd=vd+1;
 end



 for vn=1:vc1
 if v(1,vn)>0
     vdeg(1,vn)=360-vdeg(1,vn);
 end
 if v(1,vc1)==0
     vdeg(1,vc1)=360;
 end
 vn=vn+1;
 end

%increasing ring
    for j=1:ju
%%%%%%%%%%%%%%%%%%%%%%%%%%%%%%%%%%%%%%%%%%%%%%%%%%%%%%%%%%%%%%%%%%%%%%%
        ai(j)=a+j;
```

```
        bi(j)=b+j;
        xi(j)=x0+ai(j).*cos(orien);
        xii(j)=x0-ai(j).*cos(orien);
        yi(j)=y0-ai(j).*sin(orien);
        yii(j)=y0+ai(j).*sin(orien);
        wI(j) = atan2(yii(j)-yi(j),xii(j)-xi(j));

        for tn=1:n
            XI(j,tn) = ai(j).*cos(t(tn));
            YI(j,tn) = bi(j).*sin(t(tn));
            x(j,tn) = (xi(j)+xii(j))./2 + XI(j,tn).*cos(wI(j)) -
YI(j,tn).*sin(wI(j));
            y(j,tn)= (yi(j)+yii(j))./2 + XI(j,tn).*sin(wI(j)) +
YI(j,tn).*cos(wI(j));
            tn=tn+1;
        end
            j=j+1;
    end

    % decreasing ring

    for d=1:du
%%%%%%%%%%%%%%%%%%%%%%%%%%%%%%%%%%%%%%%%%%%%%%%%%%%%%%%%%%%%%%%%%%%%%%%%%%%
        c(d)=a-d;
        o(d)=b-d;
        xm(d)=x0+c(d).*cos(orien);
        xn(d)=x0-c(d).*cos(orien);
        yn(d)=y0-c(d).*sin(orien);
        yii(d)=y0+c(d).*sin(orien);
        wI(d) = atan2(yii(d)-yn(d),xn(d)-xm(d));

        for tn=1:n
            XId(d,tn) = c(d).*cos(t(tn));
            YId(d,tn) = o(d).*sin(t(tn));
            xd(d,tn) = (xm(d)+xn(d))./2 + XId(d,tn).*cos(wI(d)) -
YId(d,tn).*sin(wI(d));
            yd(d,tn)= (yn(d)+yii(d))./2 + XId(d,tn).*sin(wI(d)) +
YId(d,tn).*cos(wI(d));
            tn=tn+1;
        end
            d=d+1;
    end



   % subplot(1,2,1)

    plot(x,y,xd,yd,xmi,ymi,'b',aa,z,'g*',x0,y0,'r*',xmi(1),ymi(1),'r*')
%plot1 information
    ylabel('Row Pixel')
    xlabel('Column Pixel')
    pause


    %%%read intensity from the figure %%%
```

```
Nymi=-1.*ymi;
xRound=round(xmi);
yRound=round(Nymi);

%increasing ring
NyL=-1.*y;
xRoundL=round(x);
yRoundL=round(NyL);
%decreasing ring
Nysm=-1.*yd;
xRoundsm=round(xd);
yRoundsm=round(Nysm);



I=zeros(1,n);
%Large
IL=zeros(ju,n);
%small
Ism=zeros(du,n);

% central ring
 for i=1:n
   I(i)=GP(yRound(i),xRound(i));
   i=i+1;
 end

%increasing ring
 for j2=1:ju
      for i=1:n
        IL(j2,i)=GP(yRoundL(j2,i),xRoundL(j2,i));
        i=i+1;
      end
 end

 %decreasing ring
 for d2=1:du
      for i=1:n
          Ism(d2,i)=GP(yRoundsm(d2,i),xRoundsm(d2,i));
        i=i+1;
      end
 end

    ISum1=[Ism;I;IL];
    tot=du+ju+1;
    Isumav=sum(ISum1)./tot;

%subplot(1,2,2)
plot(vdeg,Isumav,'b:','LineWidth',1.25)
ylabel('Intensity')
xlabel('Angle(degree)')
set(gca,'XTick',(0:60:360));
%%%%%%%%%%%%%%%%%%%%%%%%%%%%%%%%%%%%%%%%%%%%%%%%%%%%%%%%%%%
%%%simulation degree locations%%%
s=41.29;% small deg
la=69.355;% large deg
```

```
line([s/2 s/2], [0 255],'Color','red','LineStyle','--
','LineWidth',1.5);
line([s/2+la s/2+la], [0 255],'Color','red','LineStyle','--
','LineWidth',1.5);
line([s/2+2*la s/2+2*la], [0 255],'Color','red','LineStyle','--
','LineWidth',1.5);
line([1.5*s+2*la 1.5*s+2*la], [0 255],'Color','red','LineStyle','--
','LineWidth',1.5);
line([1.5*s+3*la 1.5*s+3*la], [0 255],'Color','red','LineStyle','--
','LineWidth',1.5);
line([1.5*s+4*la 1.5*s+4*la], [0 255],'Color','red','LineStyle','--
','LineWidth',1.5)
xlim([0,362])
ylim([0,260])
```

smoothingIntCurv.m

```
smyy1 = smooth(vdeg,Isumav,0.07,'loess');
smyy2 = smooth(vdeg,Isumav,0.07,'rloess');
smyy3 = smooth(vdeg,Isumav,5,'moving');
smyy4 = smooth(vdeg,Isumav,17,'sgolay');
smyy5 = smooth(vdeg,Isumav,0.11,'lowess');
smyy6 = smooth(vdeg,Isumav,0.11,'rlowess');

subplot(3,2,1)
s=41.29;% small deg
la=69.355;% large deg

plot(vdeg,Isumav,'b.',vdeg,smyy1,'r-','LineWidth',1.5)
set(gca,'YLim',[0 256])

line([s/2 s/2], [0 255],'Color','red','LineStyle','--
','LineWidth',1.5);
line([s/2+la s/2+la], [0 255],'Color','red','LineStyle','--
','LineWidth',1.5);
line([s/2+2*la s/2+2*la], [0 255],'Color','red','LineStyle','--
','LineWidth',1.5);
line([1.5*s+2*la 1.5*s+2*la], [0 255],'Color','red','LineStyle','--
','LineWidth',1.5);
line([1.5*s+3*la 1.5*s+3*la], [0 255],'Color','red','LineStyle','--
','LineWidth',1.5);
line([1.5*s+4*la 1.5*s+4*la], [0 255],'Color','red','LineStyle','--
','LineWidth',1.5);
legend('Original data','Smoothed data using ''loess''',...
    'Location','NW');
xlim([0,362])
ylim([0,260])



subplot(3,2,2)
  %%%simulation degree locations%%%
s=41.29;% small deg
la=69.355;% large deg


plot(vdeg,Isumav,'b.',vdeg,smyy2,'r-','LineWidth',1.5)
```

```
set(gca,'YLim',[0 256])

   line([s/2 s/2], [0 255],'Color','red','LineStyle','--
','LineWidth',1.5);
line([s/2+la s/2+la], [0 255],'Color','red','LineStyle','--
','LineWidth',1.5);
line([s/2+2*la s/2+2*la], [0 255],'Color','red','LineStyle','--
','LineWidth',1.5);
line([1.5*s+2*la 1.5*s+2*la], [0 255],'Color','red','LineStyle','--
','LineWidth',1.5);
line([1.5*s+3*la 1.5*s+3*la], [0 255],'Color','red','LineStyle','--
','LineWidth',1.5);
line([1.5*s+4*la 1.5*s+4*la], [0 255],'Color','red','LineStyle','--
','LineWidth',1.5);
legend('Original data','Smoothed data using ''rloess''',...
       'Location','NW')
xlim([0,362])
ylim([0,260])

subplot(3,2,3)
plot(vdeg,Isumav,'b.',vdeg,smyy3,'r-','LineWidth',1.5)
set(gca,'YLim',[0 256])

line([s/2 s/2], [0 255],'Color','red','LineStyle','--
','LineWidth',1.5);
line([s/2+la s/2+la], [0 255],'Color','red','LineStyle','--
','LineWidth',1.5);
line([s/2+2*la s/2+2*la], [0 255],'Color','red','LineStyle','--
','LineWidth',1.5);
line([1.5*s+2*la 1.5*s+2*la], [0 255],'Color','red','LineStyle','--
','LineWidth',1.5);
line([1.5*s+3*la 1.5*s+3*la], [0 255],'Color','red','LineStyle','--
','LineWidth',1.5);
line([1.5*s+4*la 1.5*s+4*la], [0 255],'Color','red','LineStyle','--
','LineWidth',1.5);
legend('Original data','Smoothed data using ''moving''',...
    'Location','NW');
xlim([0,362])
ylim([0,260])



subplot(3,2,4)
plot(vdeg,Isumav,'b.',vdeg,smyy4,'r-','LineWidth',1.5)
set(gca,'YLim',[0 256])

line([s/2 s/2], [0 255],'Color','red','LineStyle','--
','LineWidth',1.5);
line([s/2+la s/2+la], [0 255],'Color','red','LineStyle','--
','LineWidth',1.5);
line([s/2+2*la s/2+2*la], [0 255],'Color','red','LineStyle','--
','LineWidth',1.5);
line([1.5*s+2*la 1.5*s+2*la], [0 255],'Color','red','LineStyle','--
','LineWidth',1.5);
line([1.5*s+3*la 1.5*s+3*la], [0 255],'Color','red','LineStyle','--
','LineWidth',1.5);
```

```
line([1.5*s+4*la 1.5*s+4*la], [0 255],'Color','red','LineStyle','--
','LineWidth',1.5);
legend('Original data','Smoothed data using ''sgolay''',...
       'Location','NW')
xlim([0,362])
ylim([0,260])

subplot(3,2,5)
plot(vdeg,Isumav,'b.',vdeg,smyy5,'r-','LineWidth',1.5)
set(gca,'YLim',[0 256])

line([s/2 s/2], [0 255],'Color','red','LineStyle','--
','LineWidth',1.5);
line([s/2+la s/2+la], [0 255],'Color','red','LineStyle','--
','LineWidth',1.5);
line([s/2+2*la s/2+2*la], [0 255],'Color','red','LineStyle','--
','LineWidth',1.5);
line([1.5*s+2*la 1.5*s+2*la], [0 255],'Color','red','LineStyle','--
','LineWidth',1.5);
line([1.5*s+3*la 1.5*s+3*la], [0 255],'Color','red','LineStyle','--
','LineWidth',1.5);
line([1.5*s+4*la 1.5*s+4*la], [0 255],'Color','red','LineStyle','--
','LineWidth',1.5);
legend('Original data','Smoothed data using ''lowess''',...
    'Location','NW');
xlim([0,362])
ylim([0,260])


subplot(3,2,6)
plot(vdeg,Isumav,'b.',vdeg,smyy6,'r-','LineWidth',1.5)
set(gca,'YLim',[0 256])

line([s/2 s/2], [0 255],'Color','red','LineStyle','--
','LineWidth',1.5);
line([s/2+la s/2+la], [0 255],'Color','red','LineStyle','--
','LineWidth',1.5);
line([s/2+2*la s/2+2*la], [0 255],'Color','red','LineStyle','--
','LineWidth',1.5);
line([1.5*s+2*la 1.5*s+2*la], [0 255],'Color','red','LineStyle','--
','LineWidth',1.5);
line([1.5*s+3*la 1.5*s+3*la], [0 255],'Color','red','LineStyle','--
','LineWidth',1.5);
line([1.5*s+4*la 1.5*s+4*la], [0 255],'Color','red','LineStyle','--
','LineWidth',1.5);
legend('Original data','Smoothed data using ''rlowess''',...
    'Location','NW');
xlim([0,362])
ylim([0,260])
```

bf.m

IntensityOfGaussian.m

```
Isec1b(Isec1b<0)=0;Isec2b(Isec2b<0)=0;
Isec3b(Isec3b<0)=0;Isec4b(Isec4b<0)=0;
Isec5b(Isec5b<0)=0;Isec6b(Isec6b<0)=0;
```

```
%
I146=Isec1b+Isec3b+Isec6b+Isec4b;
I146=I146./4;
% %
% I146=Isec4b+Isec3b+Isec1b;
% I146=I146./3;

% I146=Isec3b+Isec1b;
% I146=I146./2;

% I25=Isec2b+Isec5b;
% I25=I25./2;

plot(vsec1',I146,'r',vsec1',Isec1b,'b',vsec1',Isec4b,'k',vsec1',Isec6b,
'y',vsec1',Isec3b,'p')
%plot(vsec2,I25,'r',vsec2,Isec2b,'b',vsec2,Isec5b,'k')

    DX1=1;                %%% %%% %%% %%% change the range of DX1-DX2
to better fit the peak
    DX2=30;              %%% %%% %%%
%     DX3=39;

    SD=vsec1'; ID=I146; sV=-5;
    SD(1:DX1)=sV; SD(DX2:end)=sV;
    ID(1:DX1)=sV;ID(DX2:end)=sV;
    SD=SD(find(SD~=sV));
    ID=ID(find(ID~=sV));
    fD1 = fit(SD,ID,'gauss1')

%     SD2=vsec2'; ID2=I25; sV=-5;
%     SD2(1:DX1)=sV; SD2(DX2:end)=sV;
%     ID2(1:DX1)=sV;ID2(DX2:end)=sV;
%     SD2=SD2(find(SD2~=sV));
%     ID2=ID2(find(ID2~=sV));
%     fD2 = fit(SD2,ID2,'gauss1')

   figure
   GFittingplot=plot(fD1,SD,ID)
%    GFittingplot=plot(fD2,SD2,ID2)
```

E. Voronoi analysis: spherical colloidal crystals crystallinity (Python)

```
[window 1]
import freud
import pandas
import numpy as np
import matplotlib.pyplot as plt
%matplotlib inline

import matplotlib.patches as Patches
from matplotlib.collections import PatchCollection
import matplotlib.lines as mlines
import matplotlib.patches as mpatch
from matplotlib.collections import PatchCollection

from matplotlib.patches import Polygon
```

```
import matplotlib.colors as colors
import matplotlib.cm as cmx

from scipy.spatial import Voronoi

import copy

[window 2]
c_i = pandas.read_excel('r_27_new.xlsx')
c_i_np = np.array(c_i)

c_f = pandas.read_excel('aa2_6_2_3.nd2 - aa2_6_2_3.nd2 (series 2).xlsx')
c_f_np = np.array(c_f)

[window 3]
core_cm = plt.get_cmap('PiYG')
# core_cm = plt.get_cmap('RdBu_r')
core_cNorm  = colors.Normalize(vmin=4, vmax=8)
core_map = cmx.ScalarMappable(norm=core_cNorm, cmap=core_cm)

def CMYK_to_RGB(cmyk):
    return np.array([(1-cmyk[0])*(1-cmyk[3]),
                     (1-cmyk[1])*(1-cmyk[3]),
                     (1-cmyk[2])*(1-cmyk[3])])

cmyk_colors = [[0,0.66,0.71,0.05],
               [0,0.3,1,0],
               [0,0,0,0.02],
               [0.45,0.17,0,0.02],
               [0.71,0.53,0,0.12]]

vert_color_dict = {}
for i,cmyk in zip(range(4,9),cmyk_colors):
    vert_color_dict[i] = CMYK_to_RGB(cmyk)

haspect = 1.15/6 # aspect ratio of the histogram plots

vert8 = np.append(np.cos(np.linspace(0,2*np.pi,num=8,endpoint=False)-
np.pi/2).reshape(-1,1),
    haspect*np.sin(np.linspace(0,2*np.pi,num=8,endpoint=False)-
np.pi/2).reshape(-1,1), axis=1)
vert7 = np.append(np.cos(np.linspace(0,2*np.pi,num=7,endpoint=False)-
np.pi/2).reshape(-1,1),
    haspect*np.sin(np.linspace(0,2*np.pi,num=7,endpoint=False)-
np.pi/2).reshape(-1,1), axis=1)
vert6 = np.append(np.cos(np.linspace(0,2*np.pi,num=6,endpoint=False)-
np.pi/6).reshape(-1,1),
    haspect*np.sin(np.linspace(0,2*np.pi,num=6,endpoint=False)-
np.pi/6).reshape(-1,1), axis=1)
vert5 = np.append(np.cos(np.linspace(0,2*np.pi,num=5,endpoint=False)-
np.pi/2).reshape(-1,1),
    haspect*np.sin(np.linspace(0,2*np.pi,num=5,endpoint=False)-
np.pi/2).reshape(-1,1), axis=1)
vert4 = np.append(np.cos(np.linspace(0,2*np.pi,num=4,endpoint=False)-
np.pi/2).reshape(-1,1),
    haspect*np.sin(np.linspace(0,2*np.pi,num=4,endpoint=False)-
np.pi/2).reshape(-1,1), axis=1)
```

```
fig = plt.figure(figsize=(8,8))
names = ['0tau_50 last cycle', '10tau_50 last cycle']


for data, d in zip([c_i_np, c_f_np],range(2)):
    Lx = 1.1*(np.amax(data[:,0]) - np.amin(data[:,0]))
    Ly = 1.1*(np.amax(data[:,1]) - np.amin(data[:,1]))
    Lz = 10000

    B0 = data[:,0:3].mean(axis=0)

    positions = np.copy(data[:,0:3])
    positions = positions - B0
    positions[:,2] = 0

    edge_buffer = 3*data[:,2].mean()

    cond = ((positions[:,0]-np.amax(positions[:,0])+edge_buffer<0)*
           (positions[:,0]+np.amax(positions[:,0])-edge_buffer>0)*
           (positions[:,1]-np.amax(positions[:,1])+edge_buffer<0)*
           (positions[:,1]+np.amax(positions[:,1])-edge_buffer>0))


    vor = Voronoi(positions[:,0:2])
    vert_num = []
    verts = []

    cidx = np.arange(len(positions))[cond]

    for idx in cidx:
        if any(np.array(vor.regions[vor.point_region[idx]])<0):
            vert_num.append(-1)
            verts.append([])
        else:
            vert_num.append(len(vor.regions[vor.point_region[idx]]))
            verts.append(vor.vertices[vor.regions[vor.point_region[idx]]])

    vert_num = np.array(vert_num)

    counts = np.array([(vert_num==4).sum(),
                       (vert_num==5).sum(),
                       (vert_num==6).sum(),
                       (vert_num==7).sum(),
                       (vert_num==8).sum()])

    ax = fig.add_subplot(221+d)
    ax.set_title(names[d], fontsize=20)

    ax.scatter(positions[:,0], positions[:,1], s=0.5, c='k')

    patches = []
    facecolors = []
    edgecolors = []
    for i in range(len(vert_num)):
        if vert_num[i] > 0 and vert_num[i] != 6:
            polygon = Polygon(xy=verts[i], closed=True)
```

```
#                           edgecolors.append([0.3,0.3,0.3]
            edgecolors.append(0.8*np.array(vert_color_dict[vert_num[i]]))
            facecolors.append(vert_color_dict[vert_num[i]])
            patches.append(polygon)
        elif vert_num[i] == 6:
            polygon = Polygon(xy=verts[i], closed=True)
#                           edgecolors.append([0.8,0.8,0.8])
            edgecolors.append(0.8*np.array([0.8,0.8,0.8]))
            facecolors.append([0.8,0.8,0.8])
            patches.append(polygon)

    p = PatchCollection(patches, alpha=1, facecolors=facecolors,
edgecolors=edgecolors)
    ax.add_collection(p)

    ax.set_yticklabels([])
    ax.set_xticklabels([])
    ax.xaxis.set_ticks_position('none')
    ax.yaxis.set_ticks_position('none')
    ax.axis('off')

    ax = fig.add_subplot(223+d)
    ax.axhline(1, lw=0.5, ls='--', c=[0.5,0.5,0.5])
    ax.bar(np.arange(4,9), counts/counts.sum(), width=0.9, color='w',
edgecolor='k')

    ax.set_ylim([0,haspect*(len(counts)+1)])
    ax.set_ylabel(r'$N_{defect}/N_{total}$', fontsize=14)
    ax.set_xlabel(r'$n_{sides}$', fontsize=14)

    print(names[d], counts)
    for pidx, verts in zip(range(5),[vert4,vert5,vert6,vert7,vert8]):
        pos = np.array([[pidx+4, counts[pidx]/counts.sum()+0.4*haspect]])

        patch = Polygon(xy=0.35*verts+pos,
                        closed=True, lw=1,
facecolor=vert_color_dict[pidx+4],
                        zorder=20, #transform=fig.transFigure, figure=fig,
                        ec=0.8*np.array(vert_color_dict[pidx+4]))
        ax.add_patch(patch)

fig.tight_layout()

fig.savefig('voronoi_example.png', dpi=300)

[window 4]
vert8 = np.append(np.cos(np.linspace(0,2*np.pi,num=8,endpoint=False)-
np.pi/2).reshape(-1,1),
    np.sin(np.linspace(0,2*np.pi,num=8,endpoint=False)-np.pi/2).reshape(-
1,1), axis=1)
vert7 = np.append(np.cos(np.linspace(0,2*np.pi,num=7,endpoint=False)-
np.pi/2).reshape(-1,1),
    np.sin(np.linspace(0,2*np.pi,num=7,endpoint=False)-np.pi/2).reshape(-
1,1), axis=1)
vert6 = np.append(np.cos(np.linspace(0,2*np.pi,num=6,endpoint=False)-
np.pi/6).reshape(-1,1),
    np.sin(np.linspace(0,2*np.pi,num=6,endpoint=False)-np.pi/6).reshape(-
1,1), axis=1)
```

```
vert5 = np.append(np.cos(np.linspace(0,2*np.pi,num=5,endpoint=False)-
np.pi/2).reshape(-1,1),
    np.sin(np.linspace(0,2*np.pi,num=5,endpoint=False)-np.pi/2).reshape(-
1,1), axis=1)
vert4 = np.append(np.cos(np.linspace(0,2*np.pi,num=4,endpoint=False)-
np.pi/2).reshape(-1,1),
    np.sin(np.linspace(0,2*np.pi,num=4,endpoint=False)-np.pi/2).reshape(-
1,1), axis=1)

for pidx, verts in zip(range(4,9),[vert4,vert5,vert6,vert7,vert8]):
    fig = plt.figure(figsize=(2,2))
    ax = fig.add_subplot(111)
    patch = Polygon(xy=verts,
                    closed=True, lw=1, facecolor=vert_color_dict[pidx],
                    ec=0.8*np.array(vert_color_dict[pidx]))
    ax.add_patch(patch)
    ax.set_ylim([-1,1])
    ax.set_xlim([-1,1])
    ax.set_yticklabels([])
    ax.set_xticklabels([])
    ax.xaxis.set_ticks_position('none')
    ax.yaxis.set_ticks_position('none')
    ax.axis('off')
    plt.subplots_adjust(0,0,1,1,0,0)
    fig.savefig('polygon_{s}.png'.format(s=pidx), dpi=200,
transparent=True)
```

F. Box counting (Matlab)

b_ThreeD_BoxC.m

```
%%cube
%  A = ones(512,512,512);

% %%sphere
% imageSizeX = 512;imageSizeY = 512;imageSizeZ =512;
% [X,Y,Z] = ndgrid(1:imageSizeX, 1:imageSizeY, 1:imageSizeZ);
% centerX = 256;centerY = 256; centerZ = 256;
% radius = 256;
% circlePixels = (Z-centerZ).^2 + (Y-centerY).^2 + (X-centerX).^2 <=
radius.^2;
% A=circlePixels;
% %isosurface(A)

%%Menger Sponge
% M = 0;
% n=4;
%
% for k=1:n
%    A = zeros([3^k, 3^k, 3^k]);
%    A(:,:,1:3^(k-1)) = [M,      M,        M;
%                        M, ones(size(M)), M;
%                        M,      M,        M];
%    A(:,:,3^(k-1)+1:2*3^(k-1)) = ...
%        [M,             ones(size(M)), M;
```

```
%         ones(size(M)), ones(size(M)), ones(size(M));
%         M,             ones(size(M)), M];
%    A(:,:,2*3^(k-1)+1:3^k) = [M,        M,      M;
%                              M, ones(size(M)), M;
%                              M,        M,      M];
%    M=A;
% end
%
% A=M;

srcFiles = dir('/Users/solomonlab/Desktop/passive-2z/passive-2z0_*.png');

jk=length(srcFiles);

for i = 1 : jk

    filename = strcat('/Users/solomonlab/Desktop/passive-
2z/',srcFiles(i).name);
    Id= imread(filename);
    A(:,:,i) = Id;
    i=i+1;
end

width_max = max(size(A));originheighs=size(A,3);
p = log(width_max)/log(2);
%%remap the array if the sizes are not all equal,
 p=ceil(p);width = 2^p;
 mz = zeros(width, width, width,'like', A);
 mz(1:size(A,1),1:size(A,2),1:size(A,3)) = A;
 A=mz;

t=150;  %threshold value
A=A-t;

%image dimension
[rows columns] = size(A(:,:,1));
heighs=size(A,3);

% size 1
    % n1=nnz (A);

% size 2 [2^1]
blockSizeR = 2; % Rows in block.
blockSizeC = 2; % Columns in block.
blockSizeZ = 2; % height in block.
threshold =blockSizeR^3; % threshold of counting
n2=0;

wholeBlockRows = floor(rows / blockSizeR);
blockVectorR = [blockSizeR * ones(1, wholeBlockRows)];
wholeBlockCols = floor(columns / blockSizeC);
blockVectorC = [blockSizeC * ones(1, wholeBlockCols)];
wholeBlockHeig = floor(heighs / blockSizeZ);
blockVectorZ = [blockSizeZ * ones(1, wholeBlockHeig)];
```

```
ca  = mat2cell(A, blockVectorR, blockVectorC,blockVectorZ);

for j=1:(columns/blockSizeC)^3
        S(j)=sum(sum(sum(cell2mat(ca(j)'))));
        if S(j)>threshold
            n2=n2+1;
        else
            n2=n2;
    end
        j=j+1;
end

% size 4 [2^2]
blockSizeR_4= 4; % Rows in block.
blockSizeC_4= 4; % Columns in block.
blockSizeZ_4= 4; % height in block.
threshold_4 = blockSizeR_4^3; % threshold of counting
n4=0;

wholeBlockRows_4 = floor(rows / blockSizeR_4);
blockVectorR_4 = [blockSizeR_4 * ones(1, wholeBlockRows_4)];
wholeBlockCols_4 = floor(columns / blockSizeC_4);
blockVectorC_4 = [blockSizeC_4 * ones(1, wholeBlockCols_4)];
wholeBlockHeig_4 = floor(heighs / blockSizeZ_4);
blockVectorZ_4 = [blockSizeZ_4 * ones(1, wholeBlockHeig_4)];


ca_4  = mat2cell(A, blockVectorR_4, blockVectorC_4,blockVectorZ_4);


for j_4=1:(columns/blockSizeC_4)^3
        S_4(j_4)=sum(sum(sum(cell2mat(ca_4(j_4)'))));
        if S_4(j_4)>threshold_4
            n4=n4+1;
        else
            n4=n4;
    end
        j_4=j_4+1;
end

% size 8 [2^3]
blockSizeR_8= 8; % Rows in block.
blockSizeC_8= 8; % Columns in block.
blockSizeZ_8= 8; % height in block.
threshold_8 = blockSizeR_8^3; % threshold of counting
n8=0;

wholeBlockRows_8 = floor(rows / blockSizeR_8);
blockVectorR_8 = [blockSizeR_8 * ones(1, wholeBlockRows_8)];
wholeBlockCols_8 = floor(columns / blockSizeC_8);
blockVectorC_8 = [blockSizeC_8 * ones(1, wholeBlockCols_8)];
wholeBlockHeig_8 = floor(heighs / blockSizeZ_8);
blockVectorZ_8 = [blockSizeZ_8 * ones(1, wholeBlockHeig_8)];

ca_8  = mat2cell(A, blockVectorR_8, blockVectorC_8,blockVectorZ_8);
```

```
for j_8=1:(columns/blockSizeC_8)^3
        S_8(j_8)=sum(sum(sum(cell2mat(ca_8(j_8)'))));
        if S_8(j_8)>threshold_8
            n8=n8+1;
        else
            n8=n8;
    end
        j_8=j_8+1;
end

% size 16 [2^4]
blockSizeR_16= 16; % Rows in block.
blockSizeC_16= 16; % Columns in block.
blockSizeZ_16= 16; % height in block.
threshold_16 = blockSizeR_16^3; % threshold of counting
n16=0;

wholeBlockRows_16 = floor(rows / blockSizeR_16);
blockVectorR_16 = [blockSizeR_16 * ones(1, wholeBlockRows_16)];
wholeBlockCols_16 = floor(columns / blockSizeC_16);
blockVectorC_16 = [blockSizeC_16 * ones(1, wholeBlockCols_16)];
wholeBlockHeig_16 = floor(heighs / blockSizeZ_16);
blockVectorZ_16 = [blockSizeZ_16 * ones(1, wholeBlockHeig_16)];

ca_16  = mat2cell(A, blockVectorR_16, blockVectorC_16,blockVectorZ_16);

for j_16=1:(columns/blockSizeC_16)^3
        S_16(j_16)=sum(sum(sum(cell2mat(ca_16(j_16)'))));
        if S_16(j_16)>threshold_16
            n16=n16+1;
        else
            n16=n16;
    end
        j_16=j_16+1;
end

% size 32 [2^5]
blockSizeR_32= 32; % Rows in block.
blockSizeC_32= 32; % Columns in block.
blockSizeZ_32= 32; % height in block.
threshold_32 = blockSizeR_32^3; % threshold of counting
n32=0;

wholeBlockRows_32 = floor(rows / blockSizeR_32);blockVectorR_32 =
[blockSizeR_32 * ones(1, wholeBlockRows_32)];
wholeBlockCols_32 = floor(columns / blockSizeC_32);blockVectorC_32 =
[blockSizeC_32 * ones(1, wholeBlockCols_32)];
wholeBlockHeig_32 = floor(heighs / blockSizeZ_32);blockVectorZ_32 =
[blockSizeZ_32 * ones(1, wholeBlockHeig_32)];

ca_32  = mat2cell(A, blockVectorR_32, blockVectorC_32,blockVectorZ_32);

for j_32=1:(columns/blockSizeC_32)^3
        S_32(j_32)=sum(sum(sum(cell2mat(ca_32(j_32)'))));
        if S_32(j_32)>threshold_32
            n32=n32+1;
        else
```

```
            n32=n32;
    end
        j_32=j_32+1;
end

% size 64 [2^6]
blockSizeR_64= 64; % Rows in block.
blockSizeC_64= 64; % Columns in block.
blockSizeZ_64= 64; % height in block.
threshold_64 = blockSizeR_64^3; % threshold of counting
n64=0;

wholeBlockRows_64 = floor(rows / blockSizeR_64);blockVectorR_64 =
[blockSizeR_64 * ones(1, wholeBlockRows_64)];
wholeBlockCols_64 = floor(columns / blockSizeC_64);blockVectorC_64 =
[blockSizeC_64 * ones(1, wholeBlockCols_64)];
wholeBlockHeig_64 = floor(heighs / blockSizeZ_64);blockVectorZ_64 =
[blockSizeZ_64 * ones(1, wholeBlockHeig_64)];


ca_64  = mat2cell(A, blockVectorR_64, blockVectorC_64,blockVectorZ_64);

for j_64=1:(columns/blockSizeC_64)^3
        S_64(j_64)=sum(sum(sum(cell2mat(ca_64(j_64)'))));
        if S_64(j_64)>threshold_64
            n64=n64+1;
        else
            n64=n64;
    end
        j_64=j_64+1;
end

% size 128 [2^7]
blockSizeR_128= 128; % Rows in block.
blockSizeC_128= 128; % Columns in block.
blockSizeZ_128= 128; % height in block.
threshold_128 = blockSizeR_128^3; % threshold of counting
n128=0;

wholeBlockRows_128 = floor(rows / blockSizeR_128);blockVectorR_128 =
[blockSizeR_128 * ones(1, wholeBlockRows_128)];
wholeBlockCols_128 = floor(columns / blockSizeC_128);blockVectorC_128 =
[blockSizeC_128 * ones(1, wholeBlockCols_128)];
wholeBlockHeig_128 = floor(heighs / blockSizeZ_128);blockVectorZ_128 =
[blockSizeZ_128 * ones(1, wholeBlockHeig_128)];


ca_128  = mat2cell(A, blockVectorR_128,
blockVectorC_128,blockVectorZ_128);

for j_128=1:(columns/blockSizeC_128)^3
        S_128(j_128)=sum(sum(sum(cell2mat(ca_128(j_128)'))));
        if S_128(j_128)>threshold_128
            n128=n128+1;
        else
            n128=n128;
```

```
    end
        j_128=j_128+1;
end

n=[n2;n4;n8;n16;n32;n64;n128];
```

Bibliography

1 B. Li, D. Zhou and Y. Han, *Nat Rev Mater*, 2016, **1**, 15011.
2 P. J. Lu (陸述義) and D. A. Weitz, *Annu. Rev. Condens. Matter Phys.*, 2013, **4**, 217–233.
3 M. J. Solomon, *Langmuir*, 2018, **34**, 11205–11219.
4 P. N. Pusey and W. van Megen, *Nature*, 1986, **320**, 340–342.
5 Y. Kim, A. A. Shah and M. J. Solomon, *Nat. Commun.*, 2014, **5**, 3676.
6 R. J. Macfarlane, B. Lee, H. D. Hill, A. J. Senesi, S. Seifert and C. A. Mirkin, *Proc. Natl. Acad. Sci. U. S. A.*, 2009, **106**, 10493–10498.
7 J. W. Swan, J. L. Bauer, Y. Liu and E. M. Furst, *Soft Matter*, 2014, **10**, 1102–1109.
8 S. O. Lumsdon, E. W. Kaler and O. D. Velev, *Langmuir*, 2004, **20**, 2108–2116.
9 T. D. Edwards and M. A. Bevan, *Langmuir*, 2014, **30**, 10793–10803.
10 M. Mittal, P. P. Lele, E. W. Kaler and E. M. Furst, *J. Chem. Phys.*, 2008, **129**, 064513.
11 B. Van Der Meer, L. Filion and M. Dijkstra, *Soft Matter*, 2016, **12**, 3406–3411.
12 T. Liu, B. Vansaders, S. C. Glotzer and M. J. Solomon, *ACS Appl. Mater. Interfaces*, 2020, **12**, 9842–9850.
13 R. E. Rodríguez, S. P. Agarwal, S. An, E. Kazyak, D. Das, W. Shang, R. Skye, T. Deng and N. P. Dasgupta, *ACS Appl. Mater. Interfaces*, 2018, **10**, 4614–4621.
14 A. Surmacki, L. Siefferman and H. W. Yuan, *Condor*, 2011, **113**, 590–596.
15 J. Sun, B. Bhushan and J. Tong, *RSC Adv.*, 2013, **3**, 14862–14889.
16 J. Teyssier, S. V. Saenko, D. van der Marel and M. C. Milinkovitch, *Nat. Commun.*, 2015, 1–7.
17 G. Isapour and M. Lattuada, *Adv. Mater.*, 2018, **30**, 1–36.
18 A. A. Shah, M. Ganesan, J. Jocz and M. J. Solomon, *ACS Nano*, 2014, **8**, 8095–8103.
19 H. Hu, Q. W. Chen, K. Cheng and J. Tang, *J. Mater. Chem.*, 2012, **22**, 1021–1027.
20 S. C. Glotzer and M. J. Solomon, *Nat. Mater.*, 2007, **6**, 557–562.
21 J. A. Ferrar, L. Pavlovsky, E. Viges, Y. Liu and M. J. Solomon, *AIChE J.*, 2018, **64**, 697–707.
22 A. Donev, F. H. Stillinger, P. M. Chaikin and S. Torquato, *Phys. Rev. Lett.*, 2004, **92**, 255506.
23 A. A. Shah, H. Kang, K. L. Kohlstedt, K. H. Ahn, S. C. Glotzer, C. W. Monroe and M. J. Solomon, *Small*, 2012, **8**, 1551–1562.
24 M. Ganesan and M. J. Solomon, *Soft Matter*, 2017, **13**, 3768–3776.
25 T. Ding, K. Song, K. Clays and C. H. Tung, *Adv. Mater.*, 2009, **21**, 1936–1940.
26 M. Kohri, Y. Tamai, A. Kawamura, K. Jido and M. Yamamoto, *Langmuir*, 2019, **35**, 5574–5580.
27 E. Zaccarelli, *J. Phys. Condens. Matter*, , DOI:10.1088/0953-8984/19/32/323101.
28 W. Y. Shih, W.-H. Shih and I. A. Aksay, *J. Am. Ceram. Soc.*, 2004, **82**, 616–624.
29 Y. Zhang, W. Gao, Y. Chen, T. Escajadillo, J. Ungerleider, R. H. Fang, K. Christman, V. Nizet and L. Zhang, *ACS Nano*, 2017, **11**, 11923–11930.

30 M. H. Lee and E. M. Furst, *Phys. Rev. E - Stat. Nonlinear, Soft Matter Phys.*, 2008, **77**, 1–9.
31 J. R. Rothenbuhler, J. R. Huang, B. A. Didonna, A. J. Levine and T. G. Mason, *Soft Matter*, 2009, **5**, 3639–3645.
32 M. J. Solomon and P. T. Spicer, *Soft Matter*, 2010, **6**, 1391–1400.
33 A. Mohraz and M. J. Solomon, *J. Colloid Interface Sci.*, 2006, **300**, 155–162.
34 V. J. Anderson and H. N. W. Lekkerkerker, *Nature*, 2002, **416**, 811–815.
35 A. Yethiraj, J. H. J. Thijssen, A. Wouterse and A. Van Bladderen, *Adv. Mater.*, 2004, **16**, 596–600.
36 T. Vissers, A. Van Blaaderen and A. Imhof, *Phys. Rev. Lett.*, 2011, **106**, 106–109.
37 J. J. Juárez, S. E. Feicht and M. A. Bevan, *Soft Matter*, 2012, **8**, 94–103.
38 J. Gong and N. Wu, *Langmuir*, 2017, **33**, 5769–5776.
39 Z. M. Sherman and J. W. Swan, *ACS Nano*, , DOI:10.1021/acsnano.8b08076.
40 S. J. Boehm, L. Kang, D. H. Werner and C. D. Keating, *Adv. Funct. Mater.*, 2017, **27**, 1–8.
41 A. A. Shah, B. Schultz, W. Zhang, S. C. Glotzer and M. J. Solomon, *Nat. Mater.*, 2015, **14**, 117–124.
42 J. M. Harp, D. E. Timm and G. J. Bunick, *Acta Crystallogr. Sect. D Biol. Crystallogr.*, 1998, **54**, 622–628.
43 S. Kriminski, C. L. Caylor, M. C. Nonato, K. D. Finkelstein and R. E. Thorne, *Acta Crystallogr. Sect. D Biol. Crystallogr.*, 2002, **58**, 459–471.
44 P. T. Korda and D. G. Grier, *J. Chem. Phys.*, 2001, **114**, 7570–7573.
45 B. Vansaders and S. C. Glotzer, *Soft Matter*, 2019, **15**, 6086–6096.
46 M. E. Cates, J. P. Wittmer, J. P. Bouchaud and P. Claudin, *Phys. Rev. Lett.*, 1998, **81**, 1841–1844.
47 X. Tang, B. Rupp, Y. Yang, T. D. Edwards, M. A. Grover and M. A. Bevan, *ACS Nano*, 2016, **10**, 6791–6798.
48 X. Tang, J. Zhang, M. A. Bevan and M. A. Grover, *J. Process Control*, 2017, **60**, 141–151.
49 J. Zhang, J. Yang, Y. Zhang and M. A. Bevan, *Sci. Adv.*, 2020, **6**, 1–11.
50 S. Ramananarivo, E. Ducrot and J. Palacci, *Nat. Commun.*, , DOI:10.1038/s41467-019-11362-y.
51 D. P. Singh, U. Choudhury, P. Fischer and A. G. Mark, *Adv. Mater.*, 2017, **29**, 1–7.
52 A. Altemose, A. J. Harris and A. Sen, *ChemSystemsChem*, , DOI:10.1002/syst.201900021.
53 T. V. Rajan, C. P. Sharma and A. Sharma, *Heat Treatment: Principles And Techniques*, Prentice-Hall of India, 1992.
54 Z. M. Sherman and J. W. Swan, *ACS Nano*, 2016, **10**, 5260–5271.
55 P.-K. Kao, B. J. Vansaders, M. D. Durkin, S. C. Glotzer and M. J. Solomon, *Soft Matter*, , DOI:10.1039/c9sm00887j.
56 P. Bahukudumbi and M. A. Bevan, *J. Chem. Phys.*, , DOI:10.1063/1.2739548.
57 D. B. Allan, T. Caswell, N. C. Keim and C. M. van der Wel, trackpy: Trackpy v0.4.1.
58 R. Metzler, J. H. Jeon, A. G. Cherstvy and E. Barkai, *Phys. Chem. Chem. Phys.*, 2014, **16**, 24128–24164.
59 K. A. Rose, M. Molaei, M. J. Boyle, D. Lee, J. C. Crocker and R. J. Composto, *J. Appl. Phys.*, 2020, **127**, 191101.
60 L. C. Hsiao, H. Kang, K. H. Ahn and M. J. Solomon, *Soft Matter*, 2014, **10**, 9254–9259.

61 S. C. Kim, L. Yu, A. Pertsinidis and X. S. Ling, *Proc. Natl. Acad. Sci. U. S. A.*, 2020, **117**, 13220–13226.
62 C. B. Barber, D. P. Dobkin and H. Huhdanpaa, *ACM Trans. Math. Softw.*, 1996, **22**, 469–483.
63 O. V. Yazyev and Y. P. Chen, *Nat. Nanotechnol.*, 2014, **9**, 755–767.
64 J. J. Juaźrez, B. G. Liu, J. Q. Cui and M. A. Bevan, *Langmuir*, 2011, **27**, 9219–9226.
65 A. Yethiraj, *Soft Matter*, 2007, **3**, 1099–1115.
66 S. Henderson, S. Mitchell and P. Bartlett, *Phys. Rev. E - Stat. Physics, Plasmas, Fluids, Relat. Interdiscip. Top.*, 2001, **64**, 8.
67 V. Sivadasan, E. Lorenz, A. G. Hoekstra and D. Bonn, *Phys. Fluids*, , DOI:10.1063/1.5121536.
68 L. C. Hsiao, S. Jamali, E. Glynos, P. F. Green, R. G. Larson and M. J. Solomon, *Phys. Rev. Lett.*, 2017, **119**, 1–6.
69 M. Kim, S. M. Anthony, S. C. Bae and S. Granick, *J. Chem. Phys.*, , DOI:10.1063/1.3623489.
70 A. L. Thorneywork, R. E. Rozas, R. P. A. Dullens and J. Horbach, *Phys. Rev. Lett.*, 2015, **115**, 1–5.
71 E. Falck, J. M. Lahtinen, I. Vattulainen and T. Ala-Nissila, *Eur. Phys. J. E*, 2004, **13**, 267–275.
72 W. Loose and B. J. Ackerson, *J. Chem. Phys.*, 1994, **101**, 7211–7220.
73 P. J. Steinhardt, D. R. Nelson and M. Ronchetti, *Phys. Rev. B*, 1983, **28**, 784–805.
74 V. Ramasubramani, B. D. Dice, E. S. Harper, M. P. Spellings, J. A. Anderson and S. C. Glotzer, *Comput. Phys. Commun.*, 2020, **254**, 107275.
75 M. Ester, H.-P. Kriegel, J. Sander and X. Xu, *Proc. 2nd Int. Conf. Knowl. Discov. Data Mining, Portland, Or*.
76 A. T. Gray, E. Mould, C. P. Royall and I. Williams, *J. Phys. Condens. Matter*, , DOI:10.1088/0953-8984/27/19/194108.
77 J. A. Anderson, C. D. Lorenz and A. Travesset, *J. Comput. Phys.*, 2008, **227**, 5342–5359.
78 J. Glaser, T. D. Nguyen, J. A. Anderson, P. Lui, F. Spiga, J. A. Millan, D. C. Morse and S. C. Glotzer, *Comput. Phys. Commun.*, 2015, **192**, 97–107.
79 J. A. Anderson, J. Glaser and S. C. Glotzer, *Comput. Mater. Sci.*, 2020, **173**, 109363.
80 J. E. Jones, *Proc. R. Soc. A*, 1924, **106**, 463.
81 B. Vansaders, J. Dshemuchadse and S. C. Glotzer, *Phys. Rev. Mater.*, 2018, **2**, 1–7.
82 J. J. Crassous, A. M. Mihut, E. Wernersson, P. Pfleiderer, J. Vermant, P. Linse and P. Schurtenberger, *Nat. Commun.*, 2014, **5**, 5516.
83 T. D. Nguyen, C. L. Phillips, J. A. Anderson and S. C. Glotzer, *Comput. Phys. Commun.*, 2011, **182**, 2307–2313.
84 J. A. Ferrar and M. J. Solomon, *Soft Matter*, 2015, **11**, 3599–3611.
85 B. Liu, T. H. Besseling, M. Hermes, A. F. Demirörs, A. Imhof and A. Van Blaaderen, *Nat. Commun.*, 2014, **5**, 1–8.
86 A. C. Stelson, S. J. Penterman and C. M. Liddell Watson, *J. Mater. Chem. C*, 2018, **6**, 11118–11127.
87 A. C. Stelson, S. J. Penterman and C. M. Liddell Watson, *Small*, 2017, **13**, 1603509.
88 S. J. Boehm, L. Lin, K. Guzmán Betancourt, R. Emery, J. S. Mayer, T. S. Mayer and C. D. Keating, *Langmuir*, 2015, **31**, 5779–5786.
89 S. J. Boehm, L. Lin, N. Brljak, N. R. Famularo, T. S. Mayer and C. D. Keating, *Langmuir*,

2017, **33**, 10898–10906.
90 M. Caleap and B. W. Drinkwater, *Proc. Natl. Acad. Sci.*, 2014, **111**, 6226–6230.
91 K. A. Willets and R. P. Van Duyne, *Annu. Rev. Phys. Chem.*, 2007, **58**, 267–297.
92 L. M. Mäthger, E. J. Denton, N. J. Marshall and R. T. Hanlon, *J. R. Soc. Interface*, 2009, **6**, S149–S163.
93 A. D. Pris, Y. Utturkar, C. Surman, W. G. Morris, A. Vert, S. Zalyubovskiy, T. Deng, H. T. Ghiradella and R. A. Potyrailo, *Nat. Photonics*, 2012, **6**, 195–200.
94 J. M. Weissman, H. B. Sunkara, A. S. Tse and S. A. Asher, *Science (80-.).*, 1996, **274**, 959–963.
95 S. H. Kim, J. G. Park, T. M. Choi, V. N. Manoharan and D. A. Weitz, *Nat. Commun.*, 2014, **5**, 1–8.
96 T. S. Shim, S. H. Kim, J. Y. Sim, J. M. Lim and S. M. Yang, *Adv. Mater.*, 2010, **22**, 4494–4498.
97 H. Hwang, D. A. Weitz and F. Spaepen, *Proc. Natl. Acad. Sci.*, 2019, **116**, 1180–1184.
98 Y. L. Wu, D. Derks, A. van Blaaderen and A. Imhof, *Proc. Natl. Acad. Sci.*, 2009, **106**, 10564–10569.
99 T. Palberg, *J. Phys. Condens. Matter*, 2014, **26**, 333101.
100 F. Ferri, *Rev. Sci. Instrum.*, 1997, **68**, 2265–2274.
101 J. K. G. Dhont, C. Smits and H. N. W. Lekkerkerker, *J. Colloid Interface Sci.*, 1992, **152**, 386–401.
102 S. V. Savenko and M. Dijkstra, *Phys. Rev. E*, 2004, **70**, 051401.
103 A. Mohraz and M. J. Solomon, *Langmuir*, 2005, **21**, 5298–5306.
104 D. Andrienko, *J. Mol. Liq.*, 2018, **267**, 520–541.
105 D. K. Cinader and W. R. Burghardt, *Macromolecules*, 1998, **31**, 9099–9102.
106 A. Somwangthanaroj, E. C. Lee and M. J. Solomon, *Macromolecules*, 2003, **36**, 2333–2342.
107 W. S. Cleveland, *J. Am. Stat. Assoc.*, 1979, **74**, 829–836.
108 J. P. Singh, P. P. Lele, F. Nettesheim, N. J. Wagner and E. M. Furst, *Phys. Rev. E*, 2009, **79**, 050401.
109 G. Yatsenko and K. S. Schweizer, *Langmuir*, 2008, **24**, 7474–7484.
110 D. Mukhija and M. J. Solomon, *Soft Matter*, 2011, **7**, 540–545.
111 P. Mazeron and S. Muller, *Appl. Opt.*, 1996, **35**, 3726–3735.
112 A. Ramos, H. Morgan, N. G. Green and A. Castellanos, *J. Colloid Interface Sci.*, 1999, **217**, 420–422.
113 A. Azari, J. J. Crassous, A. M. Mihut, E. Bialik, P. Schurtenberger, J. Stenhammar and P. Linse, *Langmuir*, 2017, **33**, 13834–13840.
114 V. Trappe, V. Prasad, L. Cipelletti, P. N. Segre and D. A. Weitz, *Nature*, 2001, **411**, 772–775.
115 J. G. Gay and B. J. Berne, *J. Chem. Phys.*, 1981, **74**, 3316–3319.
116 J. D. Weeks, D. Chandler and H. C. Andersen, *J. Chem. Phys.*, 1971, **54**, 5237–5247.
117 T. F. Tadros, *Encyclopedia of Colloid and Interface Science*, Springer Berlin, Heidelberg, 2013.
118 T. F. Tadros, *Colloid Stability and Application in Pharmacy. vol. 3*, Wiely-VCH Verlag GmbH & Co. KGaA, 2007.
119 T. F. Tadros, *Colloids in Paints.*, Wiley-VCH Verlag GmbH & Co. KGaA, 2010.
120 P. J. Lu, E. Zaccarelli, F. Ciulla, A. B. Schofield, F. Sciortino and D. A. Weitz, *Nature*,

DOI:10.1038/nature06931.
121 M. Y. Lin, H. M. Lindsayt, D. A. Weitz, R. C. Ballt, R. Klein and P. Meakinll, *Nature*, 1989, **339**, 360–362.
122 M. Y. Lin, H. M. Lindsay, D. A. Weitz, R. Klein, R. C. Ball and P. Meakin, *J. Phys. Condens. Matter*, 1990, **2**, 3093–3113.
123 A. H. Krall and D. A. Weitz, *Phys. Rev. Lett.*, 1998, **80**, 778–781.
124 S. Romer, H. Bissig, P. Schurtenberger and F. Scheffold, *EPL*, , DOI:10.1209/0295-5075/108/48006.
125 A. Mohraz, D. B. Moler, R. M. Ziff and M. J. Solomon, *Phys. Rev. Lett.*, 2004, **92**, 155503–1.
126 L. M. Flores-Tandy, A. V. García-Monjaraz, E. A. van Nierop, E. A. Vázquez-Martínez, J. Ruiz-Garcia and S. Mejía-Rosales, *Colloids Surfaces A Physicochem. Eng. Asp.*, DOI:10.1016/j.colsurfa.2020.124477.
127 B. Madivala, J. Fransaer and J. Vermant, *Langmuir*, 2009, **25**, 2718–2728.
128 A. Wierenga, A. P. Philipse and H. N. W. Lekkerkerker, *Langmuir*, 1998, **14**, 55–65.
129 N. Krishna Reddy, Z. Zhang, M. Paul Lettinga, J. K. G. Dhont and J. Vermant, *J. Rheol.*, 2012, **56**, 1153–1174.
130 A. P. Philipse and A. M. Wierenga, *Langmuir*, 1998, **14**, 49–54.
131 M. Lapuerta, F. J. Martos and G. Martín-González, *J. Colloid Interface Sci.*, 2010, **346**, 23–31.
132 S. J. Ahn, K. H. Ahn and S. J. Lee, *Colloid Polym. Sci.*, 2016, **294**, 859–867.
133 M. Voggenreiter, J. Roller, J. Geiger, L. Ebner, A. Zumbusch and J. M. Meijer, *Langmuir*, 2020, **36**, 13087–13095.
134 B. Ruzicka and E. Zaccarelli, *Soft Matter*, 2011, **7**, 1268–1286.
135 M. Diez-Silva, M. Dao, J. Han, C. T. Lim and S. Suresh, *MRS Bull.*, 2010, **35**, 382–388.
136 W. Shih, Y. Shih, S. Kim, J. Liu and I. A. Aksay, *Phys. Rev. A*, 1990, **42**, 4772.
137 R. de Rooij, D. van den Ende, M. H. G. Duits and J. Mellema, *Phys. Rev. E*, 1994, **49**, 3038–3049.
138 T. Gisler, R. C. Ball and D. A. Weitz, *Phys. Rev. Lett.*, 1999, **82**, 1064–1067.
139 A. D. Dinsmore and D. A. Weitz, *J. Phys. Condens. Matter*, 2002, **14**, 7581–7597.
140 L. C. Hsiao, B. A. Schultz, J. Glaser, M. Engel, M. E. Szakasits, S. C. Glotzer and M. J. Solomon, *Nat. Commun.*, DOI:10.1038/ncomms9507.
141 L. C. Hsiao, R. S. Newman, S. C. Glotzer and M. J. Solomon, *Proc. Natl. Acad. Sci. U. S. A.*, 2012, **109**, 16029–16034.
142 R. Buscall, *Colloids and Surfaces*, 1982, **5**, 269–283.
143 R. de Rooij, D. van den Ende, M. H. G. Duits and J. Mellema, *Phys. Rev. E*, 1994, **49**, 3038–3049.
144 A. H. Krall and D. A. Weitz, *Phys. Rev. Lett.*, 1998, **80**, 778–781.
145 P. B. Laxton and J. C. Berg, *Colloids Surfaces A Physicochem. Eng. Asp.*, 2007, **301**, 137–140.
146 W.-H. Shih, W. Y. Shih, S.-I. Kim, J. Liu and I. A. Aksay, *Phys. Rev. A*, 1990, **42**, 4772–4779.
147 T. Liberto, M. Le Merrer, C. Barentin, M. Bellotto and J. Colombani, *Soft Matter*, 2017, **13**, 2014–2023.
148 E. K. Hobbie, *Rheol. Acta*, 2010, **49**, 323–334.
149 A. Mohraz and M. J. Solomon, *J. Rheol.*, 2005, **49**, 657–681.

150 M. A. Rao, *Rheology of foods, semisolid, and solid foods. Principles and Aplications*, Springer New York, New York, NY, Third., 2014.
151 T. Hagiwara, H. Kumagai and K. Nakamura, *Food Hydrocoll.*, 1998, **12**, 29–36.
152 M. M. Ould Eleya, S. Ko and S. Gunasekaran, *Food Hydrocoll.*, 2004, **18**, 315–323.
153 M. Mellema, J. H. J. van Opheusden and T. van Vliet, *J. Rheol.*, 2002, **46**, 11–29.
154 Y. Cao and R. Mezzenga, *Nat. Food*, 2020, **1**, 106–118.
155 A. Rafe and S. M. A. Razavi, *Food Hydrocoll.*, 2017, **62**, 58–65.
156 W. Xiong, C. Ren, X. Xu, J. Li, L. Wang and B. Li, *Food Hydrocoll.*, 2019, **91**, 214–223.
157 S. S. Narine and A. G. Marangoni, *Phys. Rev. E - Stat. Physics, Plasmas, Fluids, Relat. Interdiscip. Top.*, 1999, **60**, 6991–7000.
158 M. E. Szakasits, K. T. Saud, X. Mao and M. J. Solomon, *Soft Matter*, 2019, **15**, 8012–8021.
159 A. D. Dinsmore and D. A. Weitz, *J. Phys. Condens. Matter*, 2002, **14**, 303.
160 A. H. L. West, J. R. Melrose and R. C. Ball, *Phys. Rev. E*, 1994, **49**, 4237–4249.
161 P. B. Laxton and J. C. Berg, *J. Colloid Interface Sci.*, 2006, **296**, 749–755.
162 G. C. Bushell, Y. D. Yan, D. Woodfield, J. Raper and R. Amal, *Adv. Colloid Interface Sci.*, 2002, **95**, 1–50.
163 A. Thill, S. Veerapaneni, B. Simon, M. Wiesner, J. Y. Bottero and D. Snidaro, *J. Colloid Interface Sci.*, 1998, **204**, 357–362.
164 A. Boromand, S. Jamali and J. M. Maia, *Soft Matter*, 2017, **13**, 458–473.
165 C. J. Dibble, M. Kogan and M. J. Solomon, *Phys. Rev. E*, 2006, **74**, 1–11.
166 H. Kumagai, T. Hagiwara, O. Miyawaki and K. Nakamura, *Hydrocolloids*, 2000, 417–422.
167 E. Dàvila and D. Parés, *Food Hydrocoll.*, 2007, **21**, 147–153.
168 M. Altenhoff, S. Aßmann, C. Teige, F. J. T. Huber and S. Will, *J. Aerosol Sci.*, , DOI:10.1016/j.jaerosci.2019.105470.
169 M. Carpineti and M. Giglio, *Phys. Rev. Lett.*, 1992, **68**, 3327–3330.
170 J. N. Immink, J. J. E. Maris, P. Schurtenberger and J. Stenhammar, *Langmuir*, 2020, **36**, 419–425.
171 B. A. Legg, M. Zhu, L. R. Comolli, B. Gilbert and J. F. Banfield, *Langmuir*, 2014, **30**, 9931–9940.
172 P. Kollmannsberger, M. Kerschnitzki, F. Repp, W. Wagermaier, R. Weinkamer and P. Fratzl, *arXiv*, 2017, 0–13.
173 P. Meakin, I. Majid, S. Havlin and H. Eugene Stanley, *J. Phys. A Gen. Phys.*, , DOI:10.1088/0305-4470/17/18/008.
174 I. Teraoka, *Polymer solutions*, John Wiley & Sons, Inc, New York, NY, 1st edn., 2002.
175 A. A. Potanin, *J. Colloid Interface Sci.*, 1991, **145**, 140–157.
176 A. CHHABRA, H. J. HERRMANN and D. P. LANDAU, *Fractal Dimensionalities of Backbones and Clusters in a Kinetic Gelation Model*, Elsevier B.V., 1986.
177 Z. Rácz and M. Plischke, *Phys. Rev. A*, 1985, **31**, 985–994.
178 J. N. Immink, J. J. E. Maris, P. Schurtenberger and J. Stenhammar, *Langmuir*, 2020, **36**, 419–425.
179 H. T. Nguyen, A. L. Graham, P. H. Koenig and L. D. Gelb, *Soft Matter*, 2019, **16**, 256–269.
180 A. D. Dinsmore, V. Prasad, I. Y. Wong and D. A. Weitz, *Phys. Rev. Lett.*, 2006, **96**, 1–4.
181 P. Schiller, S. Krüger, M. Wahab and H. J. Mögel, *Langmuir*, 2011, **27**, 10429–10437.

182 L. C. Hsiao, B. A. Schultz, J. Glaser, M. Engel, M. E. Szakasits, S. C. Glotzer and M. J. Solomon, *Nat. Commun.*, 2015, **6**, 1–8.
183 A. H. Krall, Z. Huang and D. A. Weitz, *Phys. A Stat. Mech. its Appl.*, 1997, **235**, 19–33.
184 S. J. Ahn, K. H. Ahn and S. J. Lee, *Colloid Polym. Sci.*, 2016, **294**, 859–867.
185 B. Madivala, J. Fransaer and J. Vermant, *Langmuir*, 2009, **25**, 2718–2728.
186 J. A. Champion, Y. K. Katare and S. Mitragotri, *Proc. Natl. Acad. Sci. U. S. A.*, 2007, **104**, 11901–11904.
187 K. T. Saud, M. Ganesan and M. J. Solomon, *J. Rheol.*, 2021, **65**, 225–239.
188 D. Allan, T. Caswell, N. Keim and C. Van Der Wel, *soft-matter/trackpy: Trackpy v0.4.2 (Version v0.4.2). Zenodo. http://doi.org/10.5281/zenodo.3492186*.
189 V. Ramasubramani, B. D. Dice, E. S. Harper, M. P. Spellings, J. A. Anderson and S. C. Glotzer, *Comput. Phys. Commun.*, 2020, **254**, 107275.
190 R. H. Ewoldt, M. T. Johnston and L. M. Caretta, in *Complex Fluids in Biological Systems: Experiment, Theory, and Computation*, ed. S. E. Spagnolie, Springer New York, New York, NY, 2015, pp. 207–241.
191 R. Buscall, *J. Rheol.*, 2010, **54**, 1177–1183.